

**DEFECTS BY DESIGN  
ENHANCING SYNTHESIS AND CHARACTERIZATION OF  
QUANTUM MATERIALS**

by  
Lucas Allan Pressley

A dissertation submitted to The Johns Hopkins University in conformity  
with the requirements for the degree of Doctor of Philosophy

Baltimore, Maryland  
August, 2022

© 2022 Lucas Pressley  
All rights reserved

# Abstract

Materials design has been driven by the desire to improve upon our current technology. An indispensable contribution from chemistry to this process is the use of controlled doping to tune properties. The focus of chapter 1 is to further define defects and their tunability in electronic and quantum materials design.

Chapter 2 will delve into characterization tools including x-ray diffraction, heat capacity, and magnetism as useful indirect probes in understanding defect formation. Synthetic methods, with a specific focus on crystal growth using flux and floating zone method, are detailed. A specific example of the Kondo insulator YbB<sub>12</sub> is detailed to put into context the materials design cycle in creating “low defect” samples.

Chapter 3 will focus on the discovery and crystal growth of defect pyrochlores. This family of materials, with the chemical formula M<sub>2</sub>Ln<sub>3</sub>Ta<sub>3</sub>O<sub>14</sub> (M=Mg, Zn, Co, Mn; Ln=La, Pr, Nd, Sm, Eu, Gd), is synthesized. Magnetism of all samples shows no sign of ordering down to T=2 K, with heat capacity showing disorder in the form of a localized optical phonon mode modeled using an Einstein oscillator. Single crystals of Mg<sub>2</sub>Nd<sub>3</sub>Ta<sub>3</sub>O<sub>14</sub> are grown using the laser diode floating zone technique, demonstrating oxygen vacancies tunable upon annealing.

Chapter 4 shows the expansion of crystal growth of disordered systems to the high entropy oxide SmCo<sub>1/4</sub>Cr<sub>1/4</sub>Fe<sub>1/4</sub>Mn<sub>1/4</sub>O<sub>3</sub>. This material, exhibiting a large configurational entropy and high chemical disorder, is characterized for its magnetic properties in comparison to SmMO<sub>3</sub> (M=Co, Cr, Fe, Mn).

Chapter 5 showcases X-ray  $\mu$ -Computed Tomography as a nondestructive 3D technique to analyze bulk inclusions and imhogeneities. Examples are given in the field of electronic and quantum materials.

Chapter 6 takes theses process and returns to the well-studied ferroelectric PbTiO<sub>3</sub> to show advances in crystal growth. We grow low defect crystals of PbTiO<sub>3</sub> using laser diode floating zone and compare its properties to those grown using PbO flux. Our floating zone crystals demonstrate lower oxygen vacancies and less impurities to due to the control of the technique.

## Thesis Readers

Dr. Tyrel M. McQueen (Primary Advisor)  
Professor  
Department of Chemistry  
Johns Hopkins University

Dr. Howard Fairbrother  
Professor  
Department of Chemistry  
Johns Hopkins University

Dr. Rigoberto Hernandez  
Professor  
Department of Chemistry  
Johns Hopkins University

*To my creator:*

*"How great is our Lord! His power is absolute! His understanding is beyond  
comprehension!"*

*Psalm 147:5.*

# Acknowledgements

Although these people listed (and those not) are deserving of countless more than a simple acknowledgement, this will have to suffice for now. I would like to thank members of the McQueen lab past and present for helping me on my journey here. While my time with them was short, Dr. Zachary Kelly, Dr. Jessica Panella and Dr. Lennox Morey all helped set up the lab for success in my time here. Dr. Mekhola Sinha, Dr. Veronica Stewart and Dr. Chris Pasco were excellent senior graduate students and helped guide me through the world of solid state chemistry. Nicholas Ng, Shannon Bernier, Evan Crites, Benjamin Redemann, Austin Ferrenti, Gregory Bassen, Thomas Whoriskey, Izze Hedrick, and Jason Zhang have all been tremendous help and wonderful labmates. Tanya Berry has been not only a wonderful office mate but a truly individual mind with great insights into our field. Our postdocs Dr. Thao Tran, Dr. Michal Winiarski, Dr. Lisa Pogue and Dr. Brandon Wilfong are geniuses in their own right and have been encouraging as well as motivating me toward excellence. Members of the Institute for Quantum Matter and PARADIM, specifically Chris Lygouras, Alireza Ghasemi, Yi Luo, Dr. Seyed Koohpayeh, Professor Collin Broholm and David Elbert among others, are equally deserving of praise for being excellent sources of wisdom and expertise. For my thesis committee, Professors Howard Fairbrother and Rigoberto Hernandez have been superb teachers and I thank them for taking the time to mold and grow me into a model scientist. The three associate directors of PARADIM, Dr. Adam Phelan, Dr. Mojammel Khan, and Dr. Satya Kushwaha have helped my time as a trainee flourish and each individually impacted

me as secondary advisors in my projects. I have had the pleasure of serving Angela Torrejon, Julia Trowbridge, Luc Capaldi, and Noah Edmiston as a mentor and have been ever appreciative of all that I've learned from them. My undergraduate advisor Dr. Latha Gearheart first sparked the joy of research in me and I have been blessed to have him for advice over the years.

Outside of the world of quantum materials, I've had help along the way. Jim, Aron, Brian, Emily, Jake, and Caldwell have all kept me entertained during long days in lab. Friends at Hopkins, Danielle Bautista, Eric Peterson, Alexa Wallace helped me feel at home and survive the past 5 years of graduate school. Hector Vivanco and Dr. Juan Chamorro helped me transition into the McQueen lab and have assisted me more than they know in hard times. My friends outside of Hopkins, are too numerous to fully list out, but my church communities at Grace City and Sowebo Community Church, the HamFam, John Love, Tyler Hayes, Joel Herd, Adam White, Evan Haney, and Dr. John Sloop have truly been pillars to lean on when things were falling apart. Truly, friends like these make life worthwhile and I wouldn't be who I am without them.

My family has always been my biggest supporters and I am so grateful for them. My mom and dad, two of the hardest workers I know for teaching me the importance of preservance and integrity. Instilling the importance of kindness, patience and pursuing God in all that I do. My sister Sarah and niece Avery for being fonts of joy and love, always making sure I have a good time when I see them. I'm so lucky to have the family that is given to me be so wonderful and hope to honor them throughout my life.

Having a good advisor in graduate school is not a given. Having Professor Tyrel McQueen as your advisor is a one of a kind privilige. I have never met someone so enthusiastic about the world of chemistry and physics, whose excitement is contagious. He has a scarily never ending well of knowledge to pull from and always knows the right knob to turn to make my experiments succeed. More than that he has served as

an ambassador for myself and I feel so supported in all I pursue. He is a kind person and who cares for the well being of all he mentors. I am ever thankful for him taking me on as a student.

Finally I'd like to dote on my loving beautiful wife Erin. I could write a whole thesis on you (and it would be a much better read). You spark a desire for adventure in me and make me a better man each passing day. Thanks for helping me on the hard times, the sleepless nights, and the breakdowns. I'm so lucky to harmonize with you in this life.

# Contents

<b>Abstract</b> . . . . .	ii
<b>Dedication</b> . . . . .	iv
<b>Acknowledgements</b> . . . . .	v
<b>Contents</b> . . . . .	viii
<b>List of Tables</b> . . . . .	xii
<b>List of Figures</b> . . . . .	xiv
<b>Chapter 1 Introduction</b> . . . . .	1
Defects in the Role of Materials Discovery . . . . .	1
Background . . . . .	1
Classification of Defects . . . . .	2
Impact on Quantum Materials . . . . .	3
<b>References</b> . . . . .	7
<b>Chapter 2 Experimental Methods</b> . . . . .	10
Characterization Tools . . . . .	10
Introduction . . . . .	10
X-ray Diffraction . . . . .	11
Heat Capacity . . . . .	14

Magnetization . . . . .	17
Synthesis Methods . . . . .	19
Solid State Synthesis . . . . .	19
Flux Crystal Growth . . . . .	20
Floating Zone Crystal Growth . . . . .	21
Crystal Growth of Kondo Insulator YbB <sub>12</sub> . . . . .	23
Background . . . . .	23
Experimental Methods and Results . . . . .	23
<b>References . . . . .</b>	<b>25</b>
<b>Chapter 3 Discovery and Single Crystal Growth of High Entropy Pyrochlores . . . . .</b>	<b>27</b>
Introduction . . . . .	27
Experimental Procedure . . . . .	29
Powder Synthesis of $A_2\text{Ta}_3Ln_3\text{O}_{14}$ ( $A=\text{Mg, Co, Mn, Zn}; Ln=\text{La, Pr, Nd, Sm, Eu, Gd}$ ) . . . . .	29
Powder Synthesis of Ni <sub>2</sub> Yb <sub>3</sub> Sb <sub>3</sub> O <sub>14</sub> . . . . .	29
Single Crystal Growth of Mg <sub>2</sub> Ta <sub>3</sub> Nd <sub>3</sub> O <sub>14</sub> . . . . .	30
Characterization . . . . .	30
Results and Discussion . . . . .	32
Conclusion . . . . .	42
Associated Content . . . . .	43
Acknowledgements . . . . .	43
<b>References . . . . .</b>	<b>45</b>
<b>Chapter 4 Transition Metal (Dis)order in Single Crystal Multicomponent Rare Earth Perovskites . . . . .</b>	<b>48</b>

Introduction . . . . .	48
Methods . . . . .	49
Synthesis . . . . .	49
Characterization . . . . .	50
Results and Discussion . . . . .	51
Conclusion . . . . .	60
Acknowledgements . . . . .	61
<b>References . . . . .</b>	<b>62</b>
<b>Chapter 5 Informing Quantum Materials Discovery and Synthesis using X-ray Micro-Computed Tomography . . . . .</b>	<b>65</b>
Introduction . . . . .	65
Experimental Methods . . . . .	66
Synthesis . . . . .	66
Characterization . . . . .	67
Results and Discussion . . . . .	67
Volumetric Measurements . . . . .	67
Flux Crystal Growth . . . . .	70
Anisotropic Measurements/Visualization . . . . .	71
Floating Zone Crystal Growth . . . . .	73
Diffraction Computed Tomography and Other Future Directions . . . . .	74
Conclusion . . . . .	76
Acknowledgements . . . . .	77
<b>References . . . . .</b>	<b>84</b>
<b>Chapter 6 Optimization of PbTiO<sub>3</sub> single crystals with flux and laser floating zone method . . . . .</b>	<b>88</b>

Introduction . . . . .	88
Methods . . . . .	89
Synthesis . . . . .	89
Characterization . . . . .	91
Results . . . . .	92
Crystal Growth . . . . .	92
Structure . . . . .	95
Physical Properties . . . . .	100
Conclusion . . . . .	108
Acknowledgements . . . . .	108
<b>References . . . . .</b>	<b>109</b>
<b>Curriculum vitae . . . . .</b>	<b>113</b>

# List of Tables

3-I	Crystallographic parameters of the SXRD for $Mg_2Ta_3Nd_3O_{14}$ . . . . .	32
3-II	Curie-Weiss fits done on magnetization measurements of the $Mg_2Ta_3Ln_3O_{14}$ series as powders. . . . .	37
3-III	A list of comparable Nd compounds and their corresponding Weiss temperatures and effective magnetic moments over the listed temperature range. . . . .	38
3-IV	The constants obtained from CW fits of $A_2Ta_3Nd_3O_{14}$ ( $A=Mg, Co, Mn$ ) can be used to create a normalized plot for comparison. . . . .	38
3-V	The fitting parameters to the $C_p/T^3$ data for both $Ln=La$ and $Ln=Nd$ . .	42
4-I	Crystallographic parameters of the SXRD for floating zone grown $SmCo_{1/4}Cr_{1/4}Fe_{1/4}Mn_{1/4}O_3$ . . . . .	53
4-II	Elemental ratios for single crystal $SmCo_{1/4}Cr_{1/4}Fe_{1/4}Mn_{1/4}O_3$ as determined by EDS . . . . .	54
4-III	Summary of magnetic behavior of parent compounds of HEO SmMO <sub>3</sub> , where $T_N$ , $T_{SR2}$ , $T_{SR1}$ , $T_{SSW}$ , and $T_{Comp}$ are the Neel temperature, spin reorientation temperatures 1 and 2, spin switching transition, and compensation temperature respectively. . . . .	58
5-I	The point-spread function radius for each CT dataset is shown to give an estimation of length of distinguishable features. . . . .	68

5-II A list of some common inhomogeneities that can impact a material's properties, adapted from Peter Rudolph. . . . .	69
6-I Crystallographic parameters of the SXRD for floating zone grown PbTiO <sub>3</sub>	96
6-II Crystallographic parameters of the SXRD for flux grown PbTiO <sub>3</sub> . . .	97
6-III Fitting parameters to the $C_p/T^3$ data for flux and floating zone crystal and starting powder . . . . .	102
6-IV Trace elemental analysis performed for both a floating zone and flux grown PbTiO <sub>3</sub> using GDMS. . . . .	107

# List of Figures

<b>Figure 1-1</b> The formation energy for defects as a function of the number of defects. . . . .	2
<b>Figure 1-2</b> An example 2D crystal lattice demonstrating Schottky and Frenkel defects. . . . .	3
<b>Figure 1-3</b> An example of magnetic frustration/ordering in a) 2D triangular lattice, b) 2D kagome lattice, c) 3D tetrahedra showing spin ice configuration. . . . .	4
<b>Figure 1-4</b> An example of the concentrations and length scales at which different defects occur for a variety of quantum and electronic materials. [7, 16, 36–42] . . . . .	6
<b>Figure 2-1</b> A flow chart for different characterization tools for analyzing and quantifying crystalline defects . . . . .	11
<b>Figure 2-2</b> A case scenario for the complimentary utilization of different forms of X-ray diffraction in materials design . . . . .	15
<b>Figure 2-3</b> The heat capacity of $\text{Bi}_2\text{Ti}_2\text{O}_7$ , $\text{Pb}_2\text{Ru}_2\text{O}_{6.5}$ , and $\text{Mg}_2\text{Ta}_3\text{Nd}_3\text{O}_{14}$ showing a low lying optical phonon. . . . .	17
<b>Figure 2-4</b> Examples of different specific kinds of crystalline defects and the corresponding synthesis tools to avoid or limit their concentration. . . . .	19

<b>Figure 2-5</b> A cartoon rendering of a floating zone set up showing the formation of a solid liquid interface using laser diodes as the heating source. . . . .	22
<b>Figure 2-6</b> The low temperature heat capacity divided by temperature as a function of temperature for different samples of YbB <sub>12</sub> . The sample that was from a zone refined floating zone growth shows significantly less upturn at low temperature, similar in magnitude to that reported by Sato et al. [21] . . . . .	24
<b>Figure 3-1</b> PXRD data of initial synthetic attempts for Mg <sub>2</sub> Ta <sub>3</sub> Ln <sub>3</sub> O <sub>14</sub> compounds, scaled according to the largest peak, with tick marks showing the allowed ( <i>hkl</i> ) reflections. The impurities that arise when targeting Mg <sub>2</sub> TaLnO <sub>6</sub> are denoted with an asterisk symbol and disappear when the appropriate stoichiometry is targeted. . . . .	31
<b>Figure 3-2</b> The crystal structure of the defect pyrochlore, with the corner-sharing tetrahedra being shown between the Nd atoms. . . . .	33
<b>Figure 3-3</b> (a) Laue image of the Mg <sub>2</sub> Ta <sub>3</sub> Nd <sub>3</sub> O <sub>14</sub> crystal aligned along the (111) plane with the various ( <i>hkl</i> ) indices labeled appropriately. This image shows well defined spots and no evidence of twinning. (b) Mg <sub>2</sub> Ta <sub>3</sub> Nd <sub>3</sub> O <sub>14</sub> crystal as grown in Ar <sub>(g)</sub> . (c) Another crystal of Mg <sub>2</sub> Ta <sub>3</sub> Nd <sub>3</sub> O <sub>14</sub> as grown in O <sub>2(g)</sub> . . . . .	35
<b>Figure 3-4</b> Annealing of oxygen deficient Mg <sub>2</sub> Ta <sub>3</sub> Nd <sub>3</sub> O <sub>14</sub> as measured using thermogravimetric analysis shows significant uptake in mass as the sample regains lost oxygen. . . . .	36
<b>Figure 3-5</b> The DC magnetic susceptibility of a crystal of Mg <sub>2</sub> Ta <sub>3</sub> Nd <sub>3</sub> O <sub>14</sub> with $\chi$ estimated as M/H. The inset shows the Curie-Weiss fit to the data. No magnetic order is apparent in this data. . . . .	39

<b>Figure 3-6</b> A dimensionless, normalized plot of $A_2\text{Ta}_3\text{Nd}_3\text{O}_{14}$ ( $A=\text{Mg, Co, Mn}$ ). All analogs display CW behavior with antiferromagnetic deviations occurring at low temperatures. The dashed black line serves as a paramagnetic CW guide to the eye. . . . .	40
<b>Figure 3-7</b> The low temperature heat capacity is fit to 3.1 with the Schottky and Debye contributions highlighted. . . . .	41
<b>Figure 3-8</b> The phonon contribution to the heat capacity of (a) $\text{Mg}_2\text{Ta}_3\text{Nd}_3\text{O}_{14}$ and (b) $\text{Mg}_2\text{Ta}_3\text{La}_3\text{O}_{14}$ is fit to a combination of three Debye modes and one Einstein mode. The fit extends up to $T=300$ K and shows no excess contribution to heat capacity as seen beyond the upturn at low temperatures that can be modeled using a two-level Schottky anomaly. A plot of the phonon density of states (c) shows the phonon modes for $Ln=\text{Nd}$ shift to higher energy, even at lower phonon energies, indicating a stiffening of the lattice for $Ln=\text{Nd}$ relative to $Ln=\text{La}$ . . . . .	43
<b>Figure 4-1</b> a) Crystal structure of $\text{SmCo}_{1/4}\text{Cr}_{1/4}\text{Fe}_{1/4}\text{Mn}_{1/4}\text{O}_3$ with Glazer notation $a^+b^-b^-$ for the tilted transition metal octahedra. Atomic displacement parameters are visualized at 80% probability b) Floating zone grown crystal of $\text{SmCo}_{1/4}\text{Cr}_{1/4}\text{Fe}_{1/4}\text{Mn}_{1/4}\text{O}_3$ c) Digitally reconstructed precession photograph from SCXRD data along the (0kl) plane . . . . .	52
<b>Figure 4-2</b> SEM image of $\text{SmCo}_{1/4}\text{Cr}_{1/4}\text{Fe}_{1/4}\text{Mn}_{1/4}\text{O}_3$ powder with EDS mapping of the transition metal elements colored. . . . .	54

**Figure 4-3** Field cooled (FZ) and zero field cooled (ZFC) magnetization as a function of temperature for a)  $\text{SmCo}_{1/4}\text{Cr}_{1/4}\text{Fe}_{1/4}\text{Mn}_{1/4}\text{O}_3$  powder, b)  $\text{SmCo}_{1/4}\text{Cr}_{1/4}\text{Fe}_{1/4}\text{Mn}_{1/4}\text{O}_3$  powder under multiple fields, c)  $\text{SmCo}_{1/4}\text{Cr}_{1/4}\text{Fe}_{1/4}\text{Mn}_{1/4}\text{O}_3$  parallel to crystal length, and d)  $\text{SmCo}_{1/4}\text{Cr}_{1/4}\text{Fe}_{1/4}\text{Mn}_{1/4}\text{O}_3$  perpendicular to crystal length . . . . . 55

**Figure 4-4** Curie Weiss fit to the paramagnetic region of zero field cooled (ZFC)  $\text{LaCo}_{1/4}\text{Cr}_{1/4}\text{Fe}_{1/4}\text{Mn}_{1/4}\text{O}_3$  powder. Inset shows the field cooled (FC) and zero field cooled (ZFC) magnetization as a function of temperature . . . . . 57

**Figure 4-5** a) Magnetization as a function of field for  $\text{SmCo}_{1/4}\text{Cr}_{1/4}\text{Fe}_{1/4}\text{Mn}_{1/4}\text{O}_3$  powder over multiple temperatures. b) A plot of the exchange bias ( $H_{EB} = [H_1 + H_2]/2$ ) for  $\text{SmCo}_{1/4}\text{Cr}_{1/4}\text{Fe}_{1/4}\text{Mn}_{1/4}\text{O}_3$  powder over multiple temperatures. . . . . 58

**Figure 4-6** Heat capacity as a function of temperature for single crystal  $\text{SmCo}_{1/4}\text{Cr}_{1/4}\text{Fe}_{1/4}\text{Mn}_{1/4}\text{O}_3$  and  $\text{LaCo}_{1/4}\text{Cr}_{1/4}\text{Fe}_{1/4}\text{Mn}_{1/4}\text{O}_3$  powder. . . . . 59

**Figure 4-7** The magnetic entropy for  $\text{SmCo}_{1/4}\text{Cr}_{1/4}\text{Fe}_{1/4}\text{Mn}_{1/4}\text{O}_3$  obtained by integrated  $C_{mag}/T$  data after subtracting the scaled La analog. b) The computed single ion crystal field for  $\text{Sm}^{3+}$  in the perovskite structure. Doublet states are indicated by  $d$ . . . . . 60

**Figure 5-1** a) A representation of the key components in a  $\mu\text{CT}$  instrument. The x-ray source shown generates x-rays in a cone-beam geometry as they transmit through the sample and hit the scintillation detector, all while the sample rotates on a stage. b) A comparison of the various time and length scales defects can form in electronic and quantum materials. . . . . 78

**Figure 5-2** a) A 3D rendering of a portion of cold pressed Cu powder with voids in the sample colored to distinguish and emphasize their dispersal throughout the sample. b) A histogram distribution of volume for the various voids present. . . . . . . . . . . . . . . . .

79

**Figure 5-3** a) A comparison of the attenuation coefficients of Al and SmB<sub>6</sub> as a function of x-ray energy in the operating range of the instrument, demonstrating the feasibility of contrasting the two components using  $\mu$ CT. The K-edge for SmB<sub>6</sub> lies between 40-60 keV, resulting in the dip of attenuation. b) Visualizations of the crystal structure of SmB<sub>6</sub> and Al, demonstrating that given the similar lattice parameter, both systems mutually support the growth of one another c) A 3D rendering of a crystal of SmB<sub>6</sub> showing the presence of Al inclusions (colored yellow) that are epitaxially oriented. d) A rendering of a different crystal of SmB<sub>6</sub> with Al inclusions showing up as epitaxially oriented layered sheets. e) A 3D rose diagram generated from the star volume distribution (SVD) of the inclusions of (c). The data is oriented along the length of the crystal, showing a preferred growth direction following the crystal habit. The image is colored according to distance from origin f) A 3D rose diagram generated from the SVD of the inclusions of (d), showing the impact the opposing layers have on the overall anisotropy. The image is colored according to distance from origin . . . . . . . . . . . . . . . . . .

80

**Figure 5-4** A single crystal of rutile- $\text{GeO}_2$  grown using a flux with a cooling rate of  $3^\circ \text{ C/hr}$ . b) Laue diffraction image of the crystal along the [011] direction. c) A representation of a crystal from the same batch as (a) generated from  $\mu\text{CT}$  data with voids present (highlighted blue). d) A 3D rose diagram of the star volume distribution of the voids. The data was aligned such that the void shows a preferential orientation parallel to the [011] direction of the crystal axis. The image is colored according to distance from origin. e) A different crystal of rutile- $\text{GeO}_2$  grown using a flux with a cooling rate of  $0.5^\circ \text{ C/hr}$ . f) A rendering of a crystal from the same batch as (e) showing no detectable voids. . . . .

81

**Figure 5-5** a) The crystal structure of  $\text{YbMgGaO}_4$  showing its trigonal nature b) A rendering of the melt from a high-pressure floating zone growth of  $\text{YbMgGaO}_4$  characterized by  $\mu\text{CT}$  to highlight the presence of internal voids, colored to be visually distinct from one another. c) An optical microscope image of the melt from the growth, showing the presence of external voids detectable by the eye. d) A contour map of the melt's void volume as a function of their relative orientation. Weak anisotropy is present as the samples grow larger in volume. Distances between the largest size voids are emphasized to show the directionality obeying the trigonal structure. . . . .

82

**Figure 5-6** Floating zone-grown rutile- $\text{TiO}_2$  is visualized in both a) diffraction CT and b) absorption CT data. Multiple crystalline domains are present in the sample, as is expected for an early-stage portion of the growth. The absorption data shown has had a Sobel filter applied to highlight the edges. . . . .

83

<b>Figure 6-1</b> a) A series of Laue images taken along the length of the sanded crystal demonstrates multiples grains. Key orientations are symbolized to help one keep track of crystal reorientation, happening at pattern 3. b) The as-grown crystal of Er-doped PbTiO <sub>3</sub> with the region labeled according to the section examined by Laue diffraction c) Piece of floating zone grown PbTiO <sub>3</sub> (left) compared to a crystal grown using PbO flux (right). . . . .	93
<b>Figure 6-2</b> SEM backscattered image of the cross section of floating zone grown PbTiO <sub>3</sub> with EDS elemental maps showing the areas of Pb deficiencies. TiO <sub>2</sub> regions show up as inclusions with crystalline shapes. . . . .	95
<b>Figure 6-3</b> Visualizations of the solved crystal structure of PbTiO <sub>3</sub> for a) floating zone grown and b) flux grown crystals. The anisotropic displacement parameters are displayed at 80% probability. CCDC 2181876-2181877 contain the supplementary crystallographic data for this paper. These data can be obtained free of charge via <a href="#">here</a> . . . . .	98
<b>Figure 6-4</b> A comparison using TGA of the uptake in oxygen upon annealing for both samples of PbTiO <sub>3</sub> . Samples grown using PbO flux demonstrate a greater amount of oxygen vacancies. Inset shows the saturation in mass once held at T=800° C b) The tetragonal-cubic transition for crystals grown by flux and floating zone. . . . .	99
<b>Figure 6-5</b> Heat capacity as plotted as $C_p/T^3$ vs log(T) to show the presence of a broad peak at low temperatures. All data sets were fit with a series of two Debye and one Einstein mode. . . . .	101

**Figure 6-6** The low temperature region of heat capacity for both sets of crystals show a linear contribution, which can be fit to a simple linear model. The sample data can also be fit using the full Debye and Einstein terms derived from the  $C_p/T^3$  data, showing the energy of the Einstein term correlates to the “slope” of the seemingly linear data . . . . . 103

**Figure 6-7** The presence of weak hysteresis in magnetization as a function of field for flux grown (left) crystals of  $\text{PbTiO}_3$ . The saturation in moment is quickly dispersed upon application of higher fields and is not impacted post-annealing under oxygen. This is contrasted with floating zone crystals (right showing Er-doped and inset shows the pure material). . . . . 105

# Chapter 1

## Introduction

### Defects in the Role of Materials Discovery

#### Background

Throughout the history of human innovation, both the harnessing and exclusion of “defects” (intentional additions or impurities) has been essential to technological advances. Whether that is alloying metals to improve hardness or purifying and then doping semiconductors for the devices we use today, it has often been advantageous to generate control and utilization of these “defects”. [1, 2] The advent of quantum materials, systems that generate emergent behavior in response to strongly correlated electrons, shows the importance of controllable defects even clearer. [3] Before understanding how defects affect materials properties, we must first thoroughly define defects. Defects are inherently linked to thermodynamics and the entropy of systems. If we consider one of the defining equations in a chemist’s life:

$$\Delta G = \Delta H - T\Delta S \tag{1.1}$$

the thermodynamic stability ( $\Delta G$ ) is increased by an increase in entropy ( $\Delta S$ ). Intuitively this tells us that, in accordance with the third law of thermodynamics, that defects must exist. More firmly, we know that the concentration of defects,  $c_v$ ,

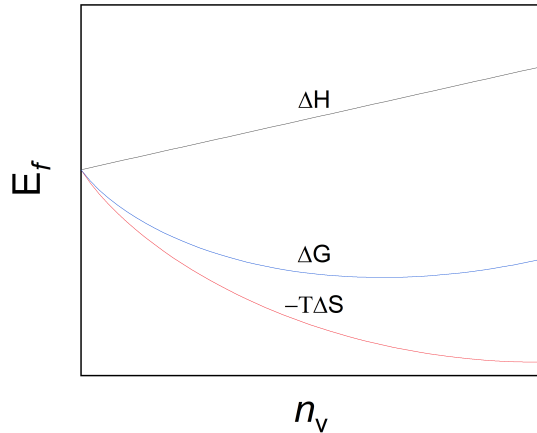


**Figure 1-1.** The formation energy for defects as a function of the number of defects.

relates to the formation energy,  $H_f$  by:

$$c_v = -e^{H_f/RT} \quad (1.2)$$

where  $T$  is temperature and  $R = 8.314\text{J/mol K}$ . The formation energy plotted as function of vacancy concentration in Figure 1 shows that as more vacancies are formed past a threshold, the favorability of formation goes down (ie the configurational entropy gain is now lowered). From this relationship we see that defects are unavoidable. The materials design cycle, a process which uses a combination of synthesis, characterization, and theory to enhance materials properties and progress the development of new compounds, must selectively control defects instead. As we will see later, this can be avoiding impurities but also doping to bring about desired or novel behavior.

## Classification of Defects

The focus of this dissertation will be on crystalline materials (solids whose atoms follow a periodic arrangement of bonding). Crystalline materials can then be further divided into polycrystalline, multiple crystallites better described as a powder than any individual grain with ideally no preferred orientation, and single crystals, composed of a single continuous crystalline domain sub mm in length or larger. For these crystalline materials, defects (regardless of intention) can be classified into point

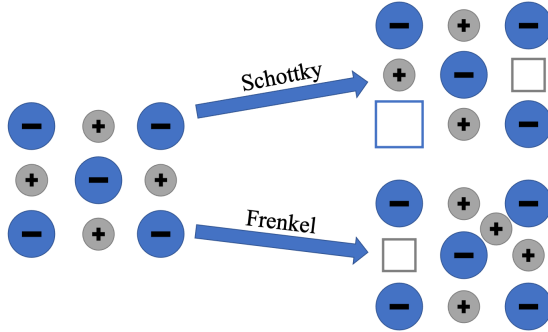


**Figure 1-2.** An example 2D crystal lattice demonstrating Schottky and Frenkel defects.

and extended defects. Point defects are related to changes on atomic sites and can be subcategorized into intrinsic (related to the material composition) and extrinsic (chemically different). Whether intrinsic or extrinsic, point defects can be vacancy pairs (Schottky) or interstitials (Frenkel). [4–6] An example of these in comparison for a simple cubic crystal structure is shown in Figure 1-2. Extended defects, as a catch all term for anything not a point defect, can be thought of more specifically as having dimensionality to it. A couple examples of this are grain boundaries, inclusions, and voids. These features, which are often overlooked due to their length scale ( $>\text{\AA}$ ), can be a serious inhibitor for the design and understanding of materials.

## Impact on Quantum Materials

With this primer, we can see how defects impact structure-property relationships by looking at examples in the realm of quantum and electronic materials. Superconductivity is the presence of zero resistance below a critical temperature ( $T_C$ ) along with the repelling of magnetic field. A pivotal discovery in the history of superconductivity was the cuprate superconductors, a family of  $\text{Cu}^{2+}$  compounds that upon (typically hole) doping display a  $T_C$  well above that which is predicted by Bardeen-Cooper-Schrieffer theory for conventional superconductivity. [7] An optimal doping (both n-type and p-type) for  $T_C$  can be found in the phase space alongside a wide variety of accessible states including charge density wave, spin stripe, and metallic. [8] We see that dopants

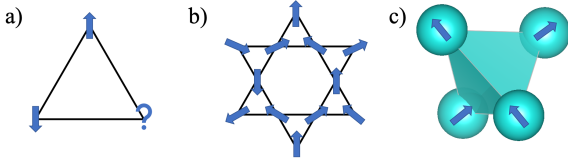


**Figure 1-3.** An example of magnetic frustration/ordering in a) 2D triangular lattice, b) 2D kagome lattice, c) 3D tetrahedra showing spin ice configuration.

are crucial to bring about the superconducting states, but other defects can equally be detrimental to the material. Non-stoichiometry, oxygen vacancies/interstitials, and low angle grain boundaries can all affect the structure-property relationships. [9–15] In this we see the care needed in not synthesizing but designing defect-controllable materials on both atomic and macro-scale to elicit out the underlying chemistry/physics at play.

Inherent to defects is also the impact they have on chemical disorder. The study of frustrated magnetism is built off this principle in efforts to achieve the quantum spin liquid (QSL) state in a material. [16] Such state is predicted not to magnetically order down to  $T=0$  K, instead adopting a resonating valence bond state. [17] A common design approach for the synthesis of QSL candidates is utilizing crystal structures that can introduce magnetic frustration based on the lattice type. [18] Examples, shown in Figure 1-3, are the 2D triangular and kagome lattices and the 3D tetrahedra. The triangle lattice is composed such that using the Ising model for antiferromagnetic ordering, where each spin wants to be antiparallel its nearest neighbors, a degeneracy is obtained in the ground state as such an arrangement is not possible. Hence the materials are geometrically frustrated. Different types of exotic magnetic ordering are possible, such as the ordering shown for the kagome lattice and the spin ice configuration for the tetrahedra ("2-in-2-out"). [19, 20] Given the desire to magnetically order, structural disorder (inherent with defects) will lift this degeneracy. [21, 22]

An example of a widely studied system where nonstoichiometric composition affects its magnetic order is the rare earth pyrochlore  $\text{Yb}_2\text{Ti}_2\text{O}_7$ . This system, now realized to

contain 2-in-2-out ferromagnetic order, was widely debated due to sample-dependent properties. [23] Differences in sample can be attributed to non-stoichiometry such as “stuffing” ( $\text{Ti}_{\text{Yb}}^+$  or  $\text{Yb}_{\text{Ti}}^-$ ). In this example we also see the usefulness of indirect probes (vida infra) such as lattice parameter and heat capacity measurements to understand and tune the disorder. [24] Of course, substitutions can also be useful in designing frustrated systems and QSL candidates. Examples of this can be seen in the partial substitution of pyrochlore systems to generate tripod kagome lattices. [25] A nonmagnetic ion (such as  $\text{Mg}/\text{Zn}^{2+}$ ) is substituted to break up the symmetry, separating out the rare earth ions to promote 2D intralayer interactions among a kagome lattice. Similar substitutions are used for the triangular lattice QSL candidate  $\text{YbMGaO}_4$  ( $\text{M}=\text{Mg}, \text{Zn}$ ). [26] This material is derived from the  $\text{YbFe}_2\text{O}_4$  type structure and hosts effective  $S = 1/2$  moment on the frustrated triangular lattice through substitution of Fe for M/Ga ( $\text{M}=\text{Mg}, \text{Zn}$ ). These doping also allow for the use of chemical pressure (changes in bond length due to differing ionic radii) to tune the magnetic ordering (or lack thereof). [27]

A third application involving the use of defects is the concept of high entropy-/multicomponent materials. These materials are often described as having a high configurational entropy according to:

$$S_{config} = R \ln(W) \quad (1.3)$$

where  $W$  is the available microstates per formula unit. Chemically speaking this looks like alloys such as  $\text{FeCrMnNiCo}$  (the famous Cantor alloy) or oxides such as  $\text{Mg}_{0.2}\text{Ni}_{0.2}\text{Cu}_{0.2}\text{Co}_{0.2}\text{Zn}_{0.2}\text{O}$ . [28, 29] The benefit this term provides is in the stabilization of a single-phase crystal structure that is reversible and demonstrates an endotherm when heating near the phase transition. Such ideas of entropy driven transformations is not necessarily new. [30] The unique development in this field however has been the impact such configurational entropy has on materials properties. If we extend this field from just entropy stabilized materials to materials exhibiting

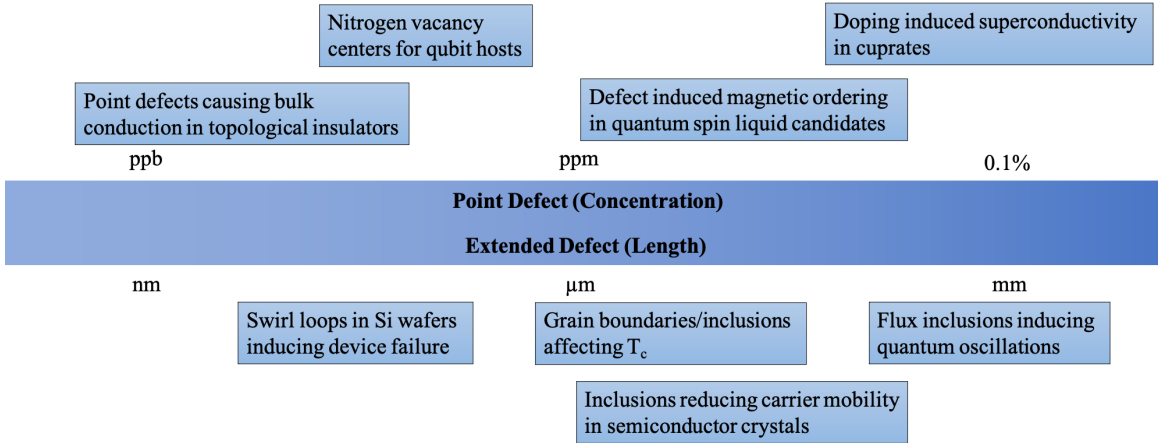


**Figure 1-4.** An example of the concentrations and length scales at which different defects occur for a variety of quantum and electronic materials. [7, 16, 36–42]

large chemical disorder, we gain access to an unprecedented phase space to dial in physical behavior. This configurational entropy/chemical disorder is utilized for a variety of applications, including but not limited to high temperature turbine blades, energy storage solutions, thermoelectrics, magnetocaloric refrigeration, and low thermal conductivity ceramics. [31–35]

To drive home the impact of defects, further phenomena are described in context of point/extended defects in Figure 1-4. We see that a range of quantum materials applications are affected by a variety of inhomogeneities, necessitating the need for synthetic control and utilization of the characterization tools we have available to us, as summarized in the next chapters. An example of how these fit into materials design is shown in Figure 1-4, where different types of defects can be characterized and synthetically controlled using the tools we have available as solid state chemists.

# References

1. Buchwald, V. *Iron and Steel in Ancient Times* (The Royal Danish Academy of Sciences and Letters, 2005).
2. Smith, R. A. *Semiconductors* (Cambridge University Press, 1979).
3. Broholm, C. *et al.* *Basic research needs workshop on quantum materials for energy relevant technology* 2016.
4. Wagner, C. & Schottky, W. Theory of controlled mixed phases. *Z. Phys. Chem. B* **11**, 163 (1930).
5. Frenkel, J. Heat Motion in Solids and Liquids. *Zeits. f. Physik* **35**, 652 (1926).
6. Seitz, F. The Nature of Lattice Defects in Silver Bromide Crystals. *Phys. Rev.* **54**, 1111–1112 (12 Dec. 1938).
7. Cava, R. J. Oxide Superconductors. *Journal of the American Ceramic Society* **83**, 5–28. eprint: <https://ceramics.onlinelibrary.wiley.com/doi/pdf/10.1111/j.1151-2916.2000.tb01142.x> (2000).
8. Keimer, B., Kivelson, S. A., Norman, M. R., Uchida, S. & Zaanen, J. From quantum matter to high-temperature superconductivity in copper oxides. *Nature* **518**, 179–186 (Feb. 2015).
9. Eisaki, H. *et al.* Effect of chemical inhomogeneity in bismuth-based copper oxide superconductors. *Phys. Rev. B* **69**, 064512 (6 Feb. 2004).
10. Baetzold, R. C. Atomistic simulation of ionic and electronic defects in  $\text{YBa}_2\text{Cu}_3\text{O}_7$ . *Phys. Rev. B* **38**, 11304–11312 (16 Dec. 1988).
11. Babcock, S. E., Cai, X. Y., Kaiser, D. L. & Larbalestier, D. C. Weak-link-free behaviour of high-angle  $\text{YBa}_2\text{Cu}_3\text{O}_{7-\delta}$  grain boundaries in high magnetic fields. *Nature* **347**, 167–169 (Sept. 1990).
12. Marshall, A. F. *et al.* Ordered-defect structure in epitaxial  $\text{YBa}_2\text{Cu}_3\text{O}_{7-x}$  thin films. *Phys. Rev. B* **37**, 9353–9358 (16 June 1988).
13. Axe, J. D. *et al.* Structural phase transformations and superconductivity in  $\text{La}_{2-x}\text{Ba}_x\text{CuO}_4$ . *Phys. Rev. Lett.* **62**, 2751–2754 (23 June 1989).
14. Tafto, J., Suenaga, M. & Sabatini, R. L. Characterization of planar crystal lattice defects in the high-temperature superconductor  $\text{YBa}_2\text{Cu}_3\text{O}_7$ . *Applied Physics Letters* **52**, 667–668. eprint: <https://doi.org/10.1063/1.99369> (1988).
15. Chen, C. H., Werder, D. J., Schneemeyer, L. F., Gallagher, P. K. & Waszczak, J. V. Observation of oxygen-vacancy-ordered domains in oxygen-deficient single-crystal  $\text{YBa}_2\text{Cu}_3\text{O}_{6.7}$ . *Phys. Rev. B* **38**, 2888–2891 (4 Aug. 1988).

16. Broholm, C. L. *et al.* Quantum Spin Liquids. *Science* **367** (2020).
17. Anderson, P. Resonating valence bonds: A new kind of insulator? *Materials Research Bulletin* **8**, 153–160 (1973).
18. Balents, L. Spin liquids in frustrated magnets. *Nature* **464**, 199–208 (Mar. 2010).
19. Paddison, J. A. M. *et al.* Emergent order in the kagome Ising magnet Dy<sub>3</sub>Mg<sub>2</sub>Sb<sub>3</sub>O<sub>14</sub>. *Nature Communications* **7**, 13842 (Dec. 2016).
20. Gingras, M. J. P. & McClarty, P. A. Quantum spin ice: a search for gapless quantum spin liquids in pyrochlore magnets. *Reports on Progress in Physics* **77**, 056501 (May 2014).
21. Reehuis, M. *et al.* Competing Jahn-Teller distortions and ferrimagnetic ordering in the geometrically frustrated system Ni<sub>1-x</sub>Cu<sub>x</sub>Cr<sub>2</sub>O<sub>4</sub>. *Phys. Rev. B* **91**, 024407 (2 Jan. 2015).
22. Chapon, L. C. *et al.* Structural Anomalies and Multiferroic Behavior in Magnetically Frustrated TbMn<sub>2</sub>O<sub>5</sub>. *Phys. Rev. Lett.* **93**, 177402 (17 Oct. 2004).
23. Scheie, A. *et al.* Multiphase magnetism in Yb<sub>2</sub>Ti<sub>2</sub>O<sub>7</sub>. *Proceedings of the National Academy of Sciences* **117**, 27245–27254. eprint: <https://www.pnas.org/doi/pdf/10.1073/pnas.2008791117> (2020).
24. Arpino, K. E., Trump, B. A., Scheie, A. O., McQueen, T. M. & Koohpayeh, S. M. Impact of Stoichiometry of Yb<sub>2</sub>Ti<sub>2</sub>O<sub>7</sub> on its Physical Properties. *Physical Review B* **95** (2017).
25. Sanders, M. B., Baroudi, K. M., Krizan, J. W., Mukadam, O. A. & Cava, R. J. Synthesis, Crystal Structure, and Magnetic Properties of Novel 2D Kagome Materials RE<sub>3</sub>Sb<sub>3</sub>Mg<sub>2</sub>O<sub>14</sub> (RE=La, Pr, Sm, Eu, Tb, Ho): Comparison to RE<sub>3</sub>Sb<sub>3</sub>Zn<sub>2</sub>O<sub>14</sub> Family. *Basic Solid State Physics* **253**, 2056–2065 (2016).
26. Li, Y. *et al.* Rare-earth triangular lattice spin liquid: A single-crystal study of YbMgGaO<sub>4</sub>. *Physical Review Letters* **115**, 167203 (2015).
27. Biesner, T. & Uykur, E. Pressure-Tuned Interactions in Frustrated Magnets: Pathway to Quantum Spin Liquids? *Crystals* **10** (2020).
28. Cantor, B., Chang, I. T. H., Knight, P. & Vincent, A. J. B. Microstructural development in equiatomic multicomponent alloys. *Materials Science and Engineering: A* **375-377**, 213–218 (2004).
29. Rost, C. M. *et al.* Entropy-Stabilized Oxides. *Nature Communications* **6** (2015).
30. Navrotsky, A. & Kleppa, O. J. Thermodynamics of Formation of Simple Spinels. *Journal of Inorganic Nuclear Chemistry* **30**, 479–498 (1968).
31. Gao, M. C., Yeh, J.-W., Liaw, P. K. & Yong, Z. *High-Entropy Alloys: Fundamentals and Applications* 1st (Cham: Springer International Publishing, 2016).
32. Sarkar, A., Kruk, R. & Hahn, H. Magnetic Properties of High Entropy Oxides. *Dalton Transactions* **50**, 1973–1982 (2021).
33. Lou, Z. *et al.* A novel high-entropy perovskite ceramics Sr<sub>0.9</sub>La<sub>0.1</sub>(Zr<sub>0.25</sub>Sn<sub>0.25</sub>Ti<sub>0.25</sub>Hf<sub>0.25</sub>)O<sub>3</sub> with low thermal conductivity and high Seebeck coefficient. *Journal of the European Ceramic Society* **42**, 3480–3488 (2022).

34. Yin, Y. *et al.* Spin-glass behavior and magnetocaloric properties of high-entropy perovskite oxide. *Applied Physics Letters* **120** (2022).
35. Banerjee, R. *et al.* High-Entropy Perovskites: An Emergent Class of Oxide Thermoelectrics with Ultralow Thermal Conductivity. *ACS Sustainable Chemistry & Engineering* **8**, 17022–17032. eprint: <https://doi.org/10.1021/acssuschemeng.0c03849> (2020).
36. Häberle, T., Schmid-Lorch, D., Karrai, K., Reinhard, F. & Wrachtrup, J. High-Dynamic-Range Imaging of Nanoscale Magnetic Fields Using Optimal Control of a Single Qubit. *Phys. Rev. Lett.* **111**, 170801 (17 Oct. 2013).
37. Föll, H. & Kolbesen, B. O. Formation and nature of swirl defects in silicon. *Applied Physics* **8**, 319–331 (1975).
38. Gurevich, A. & Pashitskii, E. A. Current transport through low-angle grain boundaries in high-temperature superconductors. *Physical Review B* **57**, 13878 (1998).
39. Durrell, J. H. & Rutter, N. A. Importance of low-angle grain boundaries in  $\text{YBa}_2\text{Cu}_3\text{O}_{7-\delta}$  coated conductors. *Superconductor Science and Technology* **22**, 013001 (2009).
40. Eo, Y. S. *et al.* Bulk Transport Paths Through Defects in Floating Zone and Al Flux Grown  $\text{SmB}_6$ . *Physical Review Materials* **5**, 055001 (2021).
41. Zhang, P. *et al.* Enhancing carrier transport properties of melt-grown  $\text{CsPbBr}_3$  single crystals by eliminating inclusions. *Crystal Growth and Design* **20**, 2424–2431 (2020).
42. Netsou, A.-M. *et al.* Identifying Native Point Defects in the Topological Insulator  $\text{Bi}_2\text{Te}_3$ . *ACS Nano* **14**. PMID: 33063986, 13172–13179. eprint: <https://doi.org/10.1021/acsnano.0c04861> (2020).

# Chapter 2

## Experimental Methods

### Characterization Tools

#### Introduction

As shown in the previous chapter, characterization tools are necessary to give us insight into the mechanisms of defect formation in materials. These techniques are also useful in giving feedback to our synthetic pathway to properly dope and tune such impurities. As the instruments available are wide-ranging, a useful classification is the distinction of direct/indirect probes. A method of approach in determining the appropriate instrument is shown in 2-1. Here direct probes are defined as instruments that directly visualize or measure concentration of defects. Imaging techniques such as transmission electron microscopy, scanning electron microscopy, and  $\mu$ -computed tomography are all different length scales that fall into the former while the techniques electron paramagnetic resonance spectroscopy and inductively coupled plasma mass spectrometry are examples of the latter. Indirect probes are measurements where the interpretation of the data can give us insight the defects/disorder present in materials. Methods like x-ray/neutron diffraction, heat capacity, and magnetization can all be utilized to indirectly measure the aforementioned properties. These probes will be discussed with examples focused relevant to the work done in chapters 3-6.

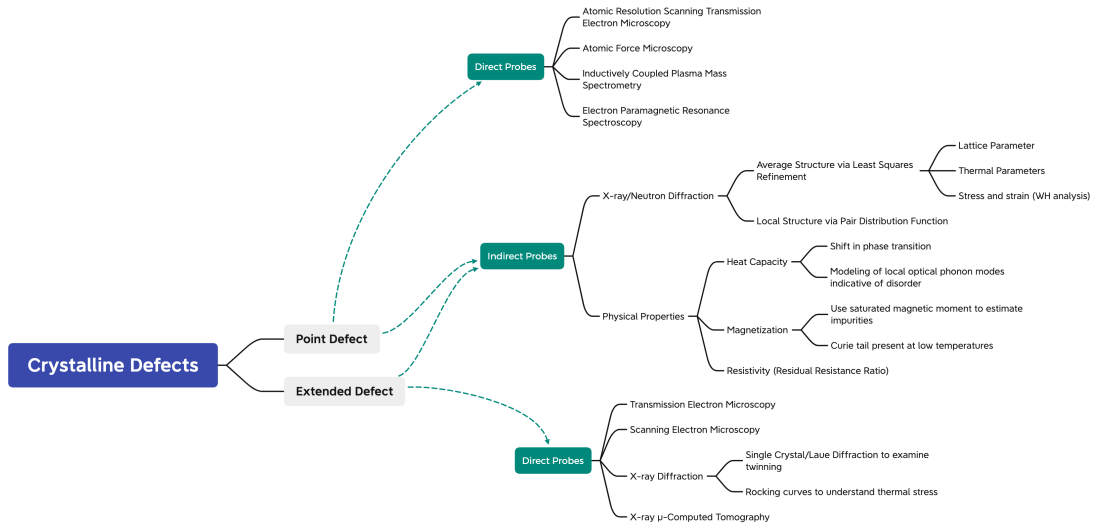


**Figure 2-1.** A flow chart for different characterization tools for analyzing and quantifying crystalline defects

## X-ray Diffraction

The use of x-rays to diffract, like light, through a material gives us information about the both the structure and composition, acting as the “fingerprint” of the material. When the X-rays incident on the material constructively interfere, this relationship is defined by Bragg’s law, thus defined:

$$n\lambda = 2d \sin(\theta) \quad (2.1)$$

Where  $\lambda$  is the wavelength of the x-ray (a common example being  $\text{Cu}K_{\alpha} = 1.56\text{\AA}$ ),  $\theta$  is the angle of diffraction,  $d$  is the spacing between lattices. A workhouse in most labs, powder x-ray diffraction (PXRD) utilizes the averaging of polycrystallites to get information about the crystal structure and phase composition. The 3D information is compressed into a 1D data set, presented as intensity as a function of angle of diffraction ( $2\theta$ ), and can be thought of in two main components.

The location of Bragg peaks gives structural information, as the spacing between peaks determines the unit cell dimensions while the absence of certain forbidden

reflections helps determine the space group. An example being for cubic systems where the spacing is related by:

$$\frac{1}{d} = \frac{1}{a}(h^2 + k^2 + l^2) \quad (2.2)$$

where  $a$  is the length of the unit cell, which is the smallest representation of the periodic arrangement of atoms that still includes necessary symmetry. The  $h, k, l$ , variables correspond to the Miller indices, the coordinate system in reciprocal space, where certain reflections can be forbidden based on unit cell type. The face centered unit cell type for example, allows only  $(hkl)$  where all is even, or all is odd.

While peak location tells us about the structure, relative intensities gives chemical information, wrapped up in what is called the structure factor:

$$I_{hkl} \propto |F_{hkl}|^2 = \left| \sum_n f_n e^{2\pi i(hx_n + ky_n + lz_n)} \right|^2 \quad (2.3)$$

where  $f_n$  is the form factor for atom  $n$ . As one can see this intensity lets us determine what atoms are located where in the structure. For x-rays this form factor scales accordingly with atomic number, thus heavier atoms are more intense. This can often make it difficult to determine the structure when lighter elements overwhelmed by the intensity of heavier elements.

The lesser discussed third component, peak width, can be attributed to a variety of factors, including crystallite size and strain. One such way to gleam information from this is using the Williamson-Hall equation:

$$\beta \cos(\theta) = \frac{k\lambda}{\tau} + \sin(\theta) \quad (2.4)$$

Where the slope and intercept give us the crystal strain and average crystallite size respectively. [1] While quantitative strain values require instrumental correction, this information can even be used comparatively to see the impact of doping or extended defects such as dislocations or stacking faults. Other subtle information can be gleamed from peak location, such as changes in lattice parameter telling us where the dopants

are coming from. Experiments with intentional doping can help us determine where the “stoichiometric” material lies. This is useful in deceptively incongruent melting materials, where the composition PXRD may show pure phase, but shifts in the lattice parameter of single crystals compared to the powder sample indicate the need for a flux to shift the composition in the phase diagram.[\[2\]](#) All above is summarized in Figure [2-2](#).

Single crystal x-ray diffraction (SCXRD) is another diffraction technique that is utilized to solve and refine the structure of new materials. In this technique, instead of using the powder average, the distinct reflections of a single crystal are collected, allowing for a larger range to be collected. The intensity and the phase (estimated using “Direct methods” typically) can then be used to generate an electron density map, allowing for structure solution of complex systems. Further refinement determines atomic locations, occupancy, and their thermal displacements. SCXRD can refine these displacement parameters anisotropically, allowing us to learn about the static and dynamic displacements present. These displacements give us information about the disorder present in the compound. [\[3\]](#) Precession images along the different  $hkl$  planes can show signs of crystal twinning, systematic absences, and local order, where further techniques like pair distribution function can be utilized to understand such behavior.

Unlike the previously mentioned use of a monochromatic X-ray source, Laue diffraction uses a polychromatic source for X-rays. By using multiple wavelengths simultaneously, the diffracted X-rays gives a map of reciprocal space. For single crystals this means distinct spots for each  $hkl$  direction. The diffracted spots demonstrate symmetry related to the crystal structure, allowing for orientation relative to distinct crystallographic planes. This technique is used for bulk materials to examine crystal quality such twinning evidenced by overlapping spots in the diffraction pattern. This technique is also used to orient the crystal in preparation for directional measurements

such as magnetization or resistivity.

An example of a typical utilization of the family of diffraction techniques in materials discovery could be the following. Use of PXRD initially helps determine the purity and structure, with such information fed back into the synthetic processes to improve preparation. Once pure phase materials are made and single crystals are needed, the appropriate technique (discussed later) can be performed. Laue diffraction will help us determine crystal quality and any changes needed to be made in the growth parameters. The Laue diffraction can then be used to orient the crystal and see any directional dependence on the previously measured physical properties. Single crystal diffraction can be included along this process to determine if the previous structure solution is correct, with further information gleaned from the displacement parameters. The final determined structure can be used by theorists for band structure calculations to help understand the materials experimental behavior. Of course, further variations can occur from this example, one such being using neutron (particles with no charge that interact with the electron spin of a material) diffraction to determine the magnetic structure, as well refine occupancies from elements with low x-ray scattering (such as hydrogen or oxygen). Thus, x-ray diffraction plays a key role in the materials discovery cycle to help inform all parts of the process.

## Heat Capacity

If x-ray diffraction is the most important compositional tool, heat capacity is the essential measurement to perform on all materials to understand its physical properties. Heat capacity, as defined as the amount of energy to raise the temperature, is often measured for solids using the semi adiabatic pulse method. Here the sample is in thermal contact with a platform connected by wires that serve as the heater. An initial pulse in power is measured along with the subsequent decay to see how temperature changes over the period. From this the heat capacity can be determined with a simple

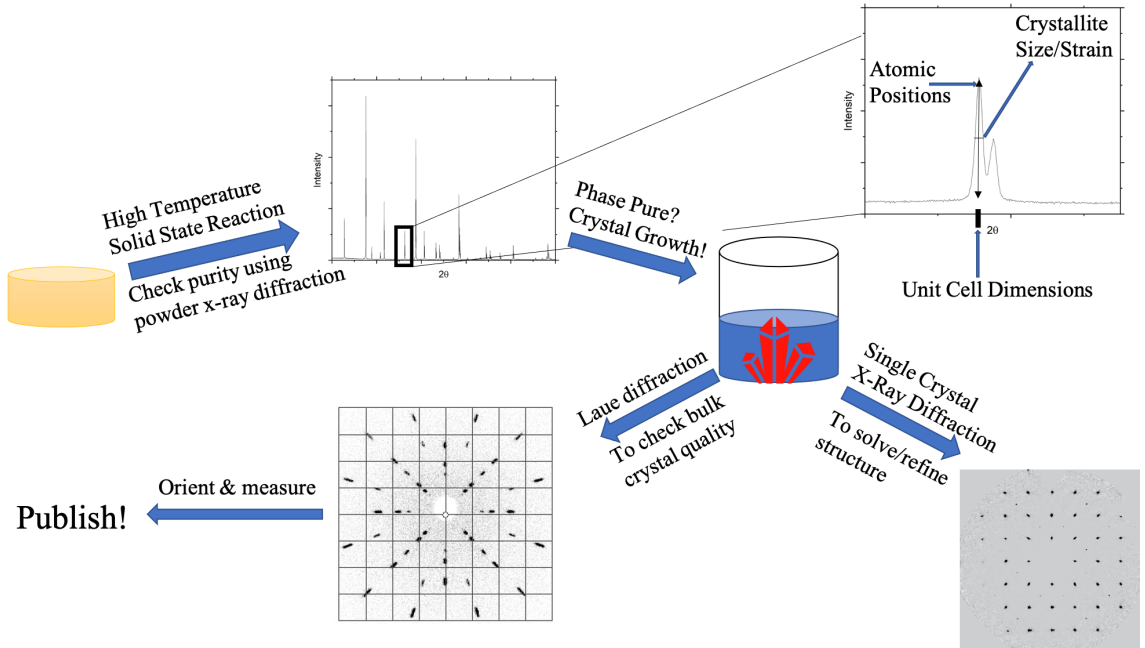


**Figure 2-2.** A case scenario for the complimentary utilization of different forms of X-ray diffraction in materials design

model being:

$$C_p \frac{dT}{dt} = -K_w(T - T_b) + P(t) \quad (2.5)$$

where  $C_p, T, K_w, T_b, P(t)$  is constant pressure heat capacity, temperature, thermal conductivity of wires, thermal bath temperature, and power applied to the platform. Here we note that while much of what is discussed later relates to specific heat at constant volume  $C_v$ ,  $C_p$  is a close approximation at low temperatures (below the Debye temperature) and is easier to measure.

Through specific heat, first order phase transition will show up as a discontinuity in the data, while second order transitions require the use of a long pulse to properly capture. At low temperatures the heat capacity can be broken into three main contributions: phonon, electronic and magnetic. Phonons (vibrations in the crystalline lattice) occurs in all materials and this lattice contribution can be modeled to extract the phonon density of states. The two main equations to model this behavior is the

Debye and Einstein models which are:

$$C_{Debye} = 9sR \frac{T^3}{\theta_D} \int_0^{\theta_D/T} \frac{(\theta/T)^4 e^{(\theta/T)}}{[e^{(\theta/T)} - 1]^2} d\frac{\theta}{T} \quad (2.6)$$

$$C_{Einstein} = 3sR \frac{\theta_E}{T} \frac{e^{\theta_E/T}}{[e^{(\theta_E/T)} - 1]^2} \quad (2.7)$$

where  $s$  relates to the number of oscillators per formula unit,  $\theta_D$  is the Debye temperature, and  $\theta_E$  corresponds to the Einstein temperature. The Einstein model considers a localized optical oscillator, while the Debye model considers vibrations similar to a particle in the box model.

The fitting of such data tells us about the disorder present. The heat capacity of systems exhibiting atoms “rattling” in cages or stereochemical displacement due to lone pairs is best modeled by inclusion of an Einstein mode to account for the localized oscillator. [4] This is visualized in Figure 2-3 where we see a broad hump in the plotting of  $C_p/T^3$  as a function of  $\log(T)$ . For  $\text{Bi}_2\text{Ti}_2\text{O}_7$  and  $\text{Pb}_2\text{Ru}_2\text{O}_{6.5}$  this is attributed to lone pair of  $\text{Bi}^{3+}$  and  $\text{Pb}^{2+}$  respectively, while  $\text{Mg}_2\text{Ta}_3\text{Nd}_3\text{O}_{14}$  is discussed further in Chapter 3. [5, 6] This modeling of disorder pairs well with x-ray diffraction to determine the static and dynamic displacements in materials.

The electronic contribution of heat capacity primarily dominates at low temperatures and increases linearly with temperature. The slope of this linear region relates to the band gap of the material. Magnetic portion of heat capacity is primarily dominate also at low temperatures and proper extraction of this contribution requires the use of a nonmagnetic analogue who has the same structure and ideally similar mass. If one can isolate the magnetic portion, the magnetic entropy can be determined through integration of the heat capacity according to:

$$\Delta S = \int \frac{C_p}{T} dT \quad (2.8)$$

The saturation of entropy as temperature increases should correspond to the effective

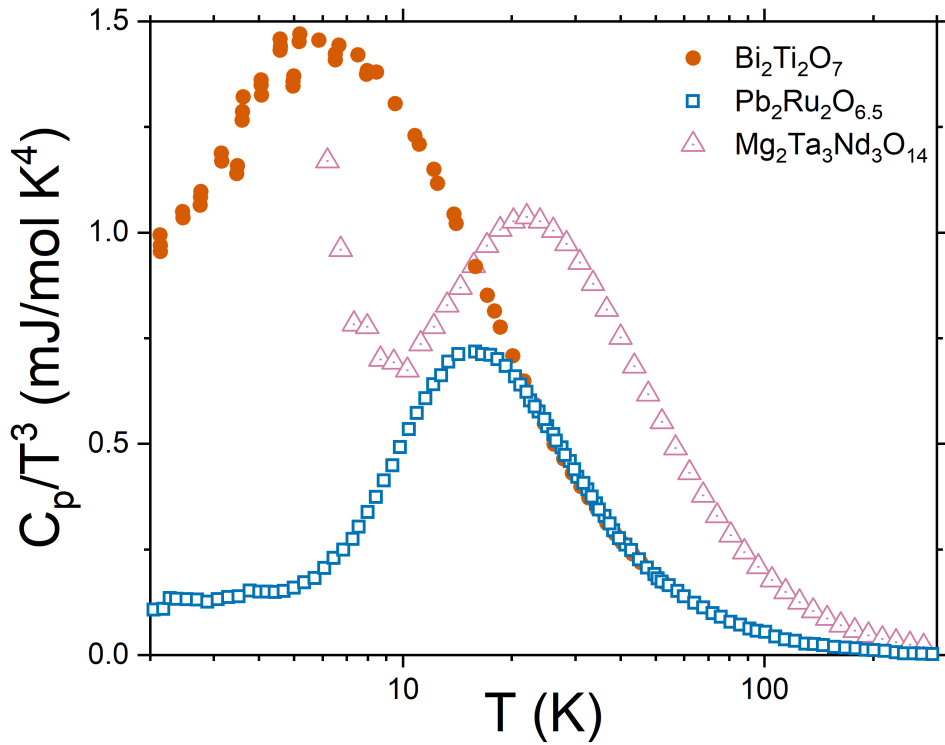


**Figure 2-3.** The heat capacity of  $\text{Bi}_2\text{Ti}_2\text{O}_7$ ,  $\text{Pb}_2\text{Ru}_2\text{O}_{6.5}$ , and  $\text{Mg}_2\text{Ta}_3\text{Nd}_3\text{O}_{14}$  showing a low lying optical phonon.

magnetic moment ( $S$ ) according to:

$$\Delta S = R \ln(2S + 1) \quad (2.9)$$

## Magnetization

As another physical property measurement, magnetization frequently pairs well with heat capacity to understand material's behavior. Materials with unpaired electrons experience a magnetic moment and will respond to an applied magnetic field. How the electrons respond depends primarily on the interaction term  $J$ , with the main types of ordering being ferromagnetic, all aligned one direction, and antiferromagnetic, all aligned alternating directions. The dimensionality of this ordering can also vary with such models being Ising (1D), xy (2D) or Heisenberg (3D). Measurement of magneti-

zation is primarily performed as function of temperature and field. Magnetization ( $M$ ) as a function of temperature can determine the transition to an ordered magnetic state while magnetization as a function of field ( $H$ ) can help us determine the suppression of certain states and presence of reversibility. The unordered paramagnetic state shows up as a linear region in the inverse of magnetization as a function of temperature. This region can be fit using the Curie-Weiss law:

$$\frac{1}{\chi} = \frac{T - \Theta}{C} \quad (2.10)$$

where  $\chi \sim M/H$ ,  $C$  is the Curie constant, and  $\Theta$  is the Weiss constant. [7] From the fitting of the linear region, the slope helps us determine the effective magnetic moment  $p_{eff}$  through:

$$p_{eff} = \sqrt{8C} \quad (2.11)$$

The x-intercept shows ferro vs antiferromagnetic ordering. To compare among a variety of materials or dopings, such fits can be normalized according to:

$$\frac{C}{\chi|\Theta|} = \frac{T}{|\Theta|} + 1 \quad (2.12)$$

Plotted this way, one is able to easily visualize deviations in magnetic behavior between samples. At low temperatures, magnetic impurities can result in an increased upturn in magnetization, commonly referred to as a Curie tail. Magnetization will also saturate at high fields, at which point the saturation value can be used to determine the magnetic concentration. This is particularly useful for diamagnetic materials (no unpaired electrons), where the observation of a saturated moment would give an estimate of the concentration of impurities present, whether or not intentionally doped.

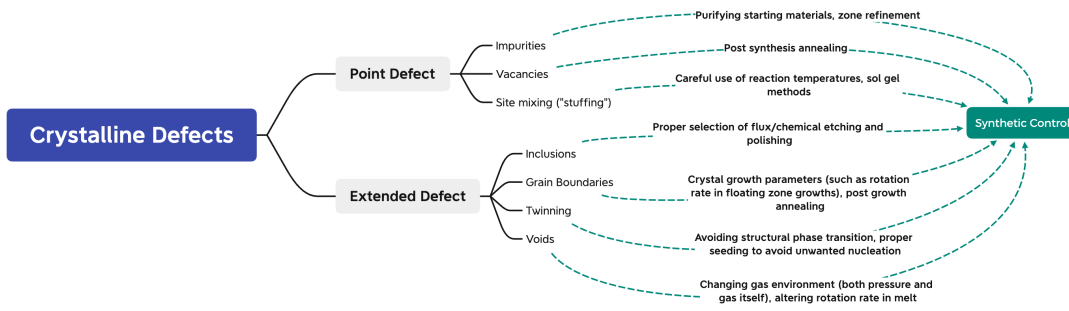


**Figure 2-4.** Examples of different specific kinds of crystalline defects and the corresponding synthesis tools to avoid or limit their concentration.

## Synthesis Methods

### Solid State Synthesis

These techniques give background into some of the important characterization tools used for this dissertation. Although controversial to some theorists, a material cannot be characterized if it is not first made! As this thesis focuses on the formation of oxides, air-free methods such as Schlenk line or sealed tubes will not be discussed. So, we will next look at some of the other synthetic tools available to us. Examples of how to use these tools in the reduction of crystalline defects is shown in Figure 2-4 Initial synthesis of a material often involves the formation of the phase in powder form. The formation of a new phase from precursor powders requires diffusion of the atoms between the constituent start materials. The method, commonly referred to as “shake and bake”, involves the intimate grinding and homogenization of powders and firing at high enough temperatures to overcome the activation energy, resulting in the formation of the thermodynamic product. [8] Loose powders can be reacted or as is or pressed into a pellet using uniaxial pressing to enhance the rate of diffusion.

Sintering of such pellets can impact grain sizes which may need to be avoided for application. In these cases, as well times when atomic level mixing or reduced reaction temperatures is needed use of a low temperature chimie douce method can

be performed. [9] In this method, precursors such as alkoxides or chlorides of the constituent elements are dissolved in a solvent and then reacted at low temperatures to create a gel (“sol-gel” method) and then subsequently heated at higher temperatures for calcination. This technique and other techniques such as microwave assisted synthesis benefits control of particle but can be require more experimental work on the front end. [10]

## Flux Crystal Growth

Once a material is made in powder form, synthesis of single crystals is often desired for the expansion of characterization possible with such material. While a variety of crystal growth techniques exist such as chemical vapor transport, Czochralski/bridgman, hydrothermal synthesis, and top seeded solution growth; the two techniques frequently used in this dissertation is flux and floating zone method. Generally, flux growth involves the use of a solvent with a readily accessible melting point (< 1000° C) to dissolve the target material, whereupon slow cooling results in the nucleation of single crystals. [11, 12]

Care must be taken in proper selection of flux, with phase diagrams often consulted to see if there exists a point in composition that can lower the material point and precipitate the target phase. Often however, the use of a secondary compound is needed to serve as a flux. In both cases flux must be removed, either mechanically through scraping/centrifugation or chemically using some type of etchant that can dissolve only the flux. [13] The benefit of this technique is in the cost of equipment as well the technical ease at which one can obtain single crystals of millimeter scale. The downside of this approach is the incorporation of defects, either impurities of the crucible from the corrosive flux or inclusions that are seeded inside the crystal along the growth direction. Both are detrimental to material’s performance and detection/elimination can be difficult due to the nature of the technique. In these

cases, a crucibleless technique can be utilized to grow low defect single crystals

## Floating Zone Crystal Growth

The floating zone technique, a crucibleless technique utilizing directional solidification, has rapidly advanced the development of single crystals with sample quality and size needed for a plethora of measurements. [14] This technique, as pictured in Figure 2-5, commonly requires the use of two polycrystalline rods, whereupon melting/joining of the two rods a solid liquid interface is created. Once established the rods are passed through this interface at such a rate (typically 1-10 mm/hr) to allow for the formation of a single crystalline domain.

A variety of parameters can impact both the stability of this zone as well as the resulting crystal, the most common of which are the rod preparation, growth speed, sample rotation, and gas environment. [15] To briefly elaborate on each:

1. The “straightness” of your rods allows for free rotation without worry of inhomogeneous heating due to sample precession out of the hot zone. Poor rod density will cause your zone to shrink and collapse
2. Growths attempted at too fast of a travel rate will result in crystal twinning and, in the case of traveling solvent growths, potential phase segregation. For volatile systems growing at too slow a rate will lead to the zone shrinking as well sample deficiencies
3. Sample rotation can impact the heat distribution and effective mixing in the liquid region. Faster rotation can lead to low angle grain boundaries and increased vaporization due to pushing to the surface. Low rotation can poorly affect the convexity of the molten zone as well and lead to poor heat distribution.
4. The gas environment impacts the chemical potential applied to the melt. High oxygen pressure can be utilized for the growth of high valence materials ( $\text{Ni}^{3+}$ )

while low oxygen partial pressure can allow for tunable valences ( $V^{3/4/5+}$ ) and oxygen vacancies. Use of applied static/dynamic argon pressure can also suppression vaporization in volatile materials (demonstrated in Chapter 6)

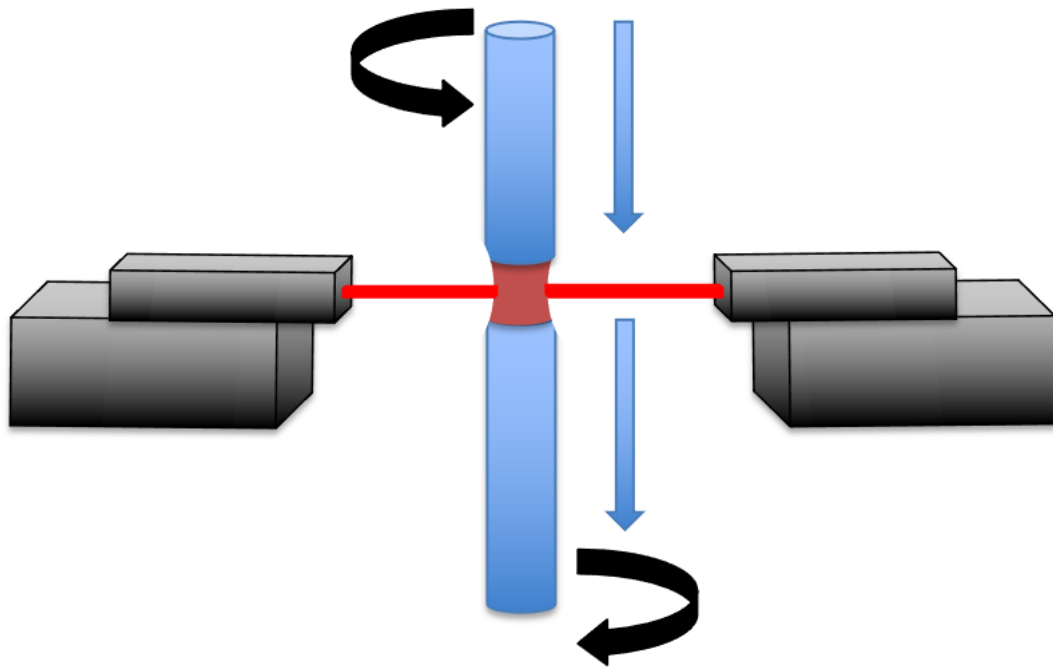


**Figure 2-5.** A cartoon rendering of a floating zone set up showing the formation of a solid liquid interface using laser diodes as the heating source.

One specific variation of this technique involves the use of laser diodes as the heating source. Compared to conventional four mirror furnaces that use halogen or xenon bulbs, the laser diode has the benefit of a sharper temperature gradient, making a more easily controlled solid-liquid interface, especially important for incongruently melting materials. [16] There are a variety of helpful scientific literature that showcases the breadth of variation in how growth parameters impact sample quality. Instead one such material is shown below to demonstrate the depth and difficulty in growing single crystal of novel materials using the floating zone technique.

# Crystal Growth of Kondo Insulator YbB<sub>12</sub>

## Background

YbB<sub>12</sub> is a kondo insulator who has frequently lived in the shadow of it's more popular cousin SmB<sub>6</sub>. This family of rare earth borides are widely investigated for their proposed topological surface states that arise due to the spin orbit coupling of the rare earth ions. [17, 18] One reason for less understanding of YbB<sub>12</sub> is in part due to the difficulty in synthesizing single crystals. [19] Unlike SmB<sub>6</sub>, YbB<sub>12</sub> is an incongruent melter, precipitating out a mixture of YbB<sub>6</sub> and YbB<sub>12</sub> if the original phase is targeted. The use of Al flux, similar to SmB<sub>6</sub> would result in sample inclusions affecting physical properties (as discussed in Chapter 5). The high melting point makes floating zone growth the only other reasonable/feasible synthesis method. In the case of incongruent melters the use of the traveling solvent technique is needed. Previously Xenon lamp furnaces were used to melt YbB<sub>12</sub>, but such furnaces often have a poorly defined solid liquid interface, making stabilization of experimental conditions difficult.

## Experimental Methods and Results

We utilize the laser diode floating zone furnace for its benefits mentioned above to overcome these difficulties. Due to the incongruent nature of this material, a traveling solven approach is needed. [20] For our traveling solvent we target a Boron rich phase  $\sim \text{YbB}_{30}$  and aim to grow slow enough to ensure chemical equilibrium in the molten zone. Initial growths performed here using a laser diode floating zone showed “melt sucking” occurring, where the molten zone retreats into the feed rod due to low density. This results in an unstable zone and high defect crystal. Further sintering using a high vacuum furnace operating at 1700° C and  $10^{-5}$  torr was performed to help densify the material. However, a shrinking zone occurred at lower growth speeds (5 mm/hr).

To overcome this, I employed the twice-scanning technique. This involves “pre-

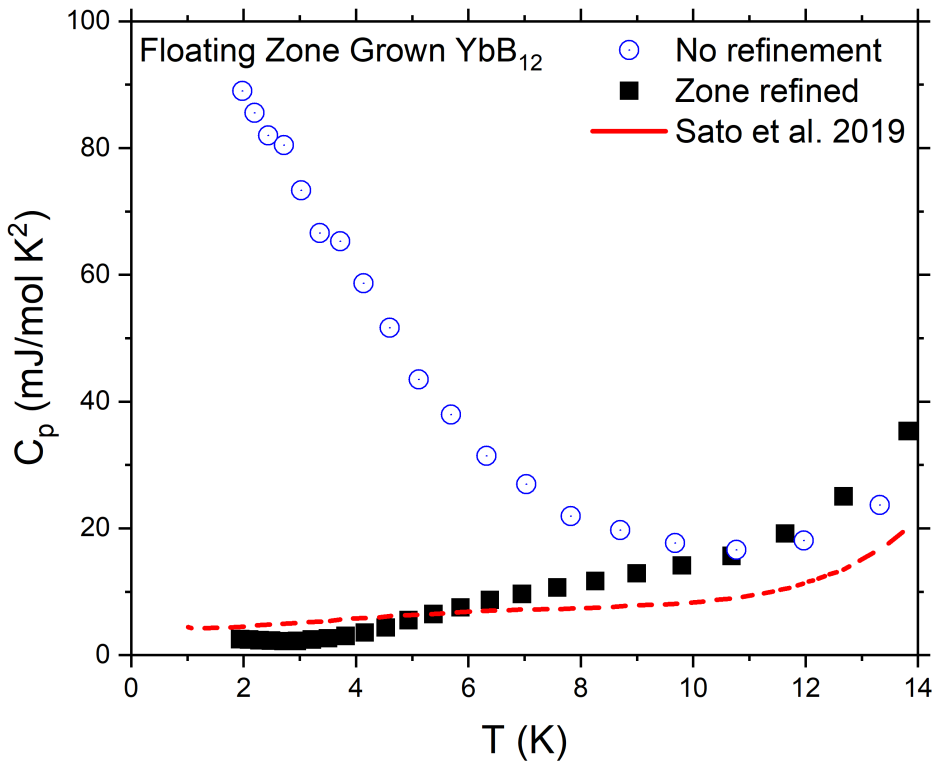


**Figure 2-6.** The low temperature heat capacity divided by temperature as a function of tempearture for different samples of  $\text{YbB}_{12}$ . The sample that was from a zone refined floating zone growth shows significantly less upturn at low temperature, similar in magnitude to that reported by Sato et al. [21]

melting” your feed rod by rapidly passing it through the hot zone, at which point the rod is reused now theoretically 100% dense. This not only resulted in a stable zone but had the added benefit of refining impurities out of the crystal. This is best evidenced by the heat capacity performed on two samples of differing quality. At low temperatures we see an upturn in heat capacity like a Curie tail in magnetization resulting from sample impurities. We see the twice grown crystal resulted in lower magnitude tail and accordingly less defects, similar in magnitude to those reported by Sato et al. [21] This one example is the result of many samples of work to further refine the growth parameters and demonstrates both the difficulty of mastering the technique for just one material as well as the proverbial fruits of such labor.

# References

1. Williamson, G. & Hall, W. X-ray line broadening from filed aluminium and wolfram. *Acta Metallurgica* **1**, 22–31 (1953).
2. Arpino, K. E., Trump, B. A., Scheie, A. O., McQueen, T. M. & Koohpayeh, S. M. Impact of Stoichiometry of  $\text{Yb}_2\text{Ti}_2\text{O}_7$  on its Physical Properties. *Physical Review B* **95** (2017).
3. Trump, B. A. *et al.* Universal Geometric Frustation in Pyrochlores. *Nature Communications* **9** (2018).
4. Winiarski, M. J. *et al.* Rattling-enhanced superconductivity in  $M\text{V}_2\text{Al}_{20}$  ( $M = \text{Sc}, \text{Lu}, \text{Y}$ ) intermetallic cage compounds. *Phys. Rev. B* **93**, 134507 (13 Apr. 2016).
5. Shoemaker, D. P. *et al.* Atomic Displacements in the Charge Ice Pyrochlore  $\text{Bi}_2\text{Ti}_2\text{O}_6\text{O}'$  Studied by Neutron Total Scattering. *Physical Review B* **81** (2010).
6. Shoemaker, D. P., Llobet, A., Tachibana, M. & Seshadri, R. Reverse Monte Carlo neutron scattering study of the ‘ordered-ice’ oxide pyrochlore  $\text{Pb}_2\text{Ru}_2\text{O}_{6.5}$ . *Journal of Physics: Condensed Matter* **23**, 315404 (July 2011).
7. Mugiraneza, S. & Hallas, A. M. Tutorial: a beginner’s guide to interpreting magnetic susceptibility data with the Curie-Weiss law. *Communications Physics* **5**, 95 (Apr. 2022).
8. Chamorro, J. R. & McQueen, T. M. Progress toward Solid State Synthesis by Design. *Accounts of Chemical Research* **51**, 2918–2925. eprint: <https://doi.org/10.1021/acs.accounts.8b00382> (2018).
9. Rouxel, J. & Tournoux, M. Chimie douce with solid precursors, past and present. *Solid State Ionics* **84**, 141–149 (1996).
10. Levin, E. E., Grebenkemper, J. H., Pollock, T. M. & Seshadri, R. Protocols for High Temperature Assisted-Microwave Preparation of Inorganic Compounds. *Chemistry of Materials* **31**, 7151–7159. eprint: <https://doi.org/10.1021/acs.chemmater.9b02594> (2019).
11. Phelan, W. A. *et al.* Adventures in crystal growth: synthesis and characterization of single crystals of complex intermetallic compounds. *Chemistry of Materials* **24**, 409–420 (2012).
12. Bugaris, D. E. & Loya, H.-C. z. Materials discovery by flux crystal growth: quartnerary and higher order oxides. *Angewandte Chemie - International Edition* **51**, 3780–3811 (2012).

13. Canfield, P. C. & Fisk, Z. Growth of single crystals from metallic fluxes. *Philosophical Magazine B* **65**, 1117–1123 (1991).
14. Koohpayeh, S. M., Fort, D. & Abell, J. S. The Optical Floating Zone Technique: A Review of Experimental Procedures with Special Reference to Oxides. *Progress in Crystal Growth and Characterization of Materials* **54**, 121–137 (2008).
15. Dabkowska, H. A. & Dabkowski, A. B. in *Springer Handbook of Crystal Growth* 367–390 (Springer Heidelberg Dordrecht London New York, 2010).
16. Ito, T. *et al.* Laser-diode-heated Floating Zone (LDFZ) Method Appropriate to Crystal Growth of Incongruently Melting Materials. *Journal of Crystal Growth* **363**, 264–269 (2013).
17. Hagiwara, K. *et al.* Surface Kondo effect and non-trivial metallic state of the Kondo insulator YbB<sub>12</sub>. *Nature Communications* **7**, 12690 (Aug. 2016).
18. Rosa, P. F. S. & Fisk, Z. in *Rare-Earth Borides* 1st, 817–875 (Jenny Stanford Publishing, 2021).
19. Iga, F., Shimizu, N. & Takabatake, T. Single crystal growth and physical properties of Kondo insulator YbB<sub>12</sub>. *Journal of Magnetism and Magnetic Materials* **177-181**. International Conference on Magnetism, 337–338 (1998).
20. Koohpayeh, S. Single crystal growth by the traveling solvent technique: A review. *Progress in Crystal Growth and Characterization of Materials* **62**. Special Issue: Recent Progress on Fundamentals and Applications of Crystal Growth; Proceedings of the 16th International Summer School on Crystal Growth (ISSCG-16), 22–34 (2016).
21. Sato, Y. *et al.* Unconventional thermal metallic state of charge-neutral fermions in an insulator. *Nature Physics* **15**, 954–959 (Sept. 2019).

# Chapter 3

## Discovery and Single Crystal Growth of High Entropy Pyrochlores

### Introduction

The pyrochlore structure type has been extensively investigated in attempts to reveal novel magnetic states of matter, including the quantum spin ice and spin liquid states. [1–3] Composed of two interpenetrating networks of corner sharing tetrahedra, the A and B sublattices, the  $A_2B_2O_7$  pyrochlore is an ideal candidate to harbor frustrated spins in the presence of antiferromagnetic or even ferromagnetic interactions. [4, 5] Combined with the chemical flexibility in atomic species that can occupy the A and B site, this system allows for a wide variety of compounds to be synthesized. [6] This gives way to an expansive range of possible magnetic states that can arise, from antiferromagnet to spin glass to spin ice. [7–9] More recently, ordered derivatives of pyrochlores that isolate individual kagomé layers of magnetic ions within one of the two sublattices have also been prepared, via careful control of relative ionic sizes. [10]

When considering the stability of a compound, having a large entropic term can drive the free energy to favor phases that normally would not form. This can be seen in high entropy alloys, a newly recognized class of materials in which the thermodynamic

driving force for formation is provided by the mixing/entropic term. They differ from traditional alloys in which enthalpic contributions are sufficient to drive stability, and already find industrial applications, e.g. 5th generation Ni superalloys used in high pressure blades of jet engines. [11] High entropy oxides have also been discovered, including the rocksalt  $(\text{Mg},\text{Co},\text{Ni},\text{Cu},\text{Zn})_{0.2}\text{O}$  and spinel  $(\text{Co},\text{Cr},\text{Fe},\text{Mn},\text{Ni})_3\text{O}_4$ . [12, 13] Recently, we reported similar stabilization in the pyrochlore family of materials by way of partial ion substitution on the A and B sites, stabilizing  $\text{Mn}_2\text{Sb}_2\text{O}_7$  which only existed as a pyrochlore previously in metastable form. [14]

Here we report the discovery of a new family of high entropy pyrochlores of general formula  $\text{Mg}_2\text{Ta}_3Ln_3\text{O}_{14}$  ( $Ln=\text{La}, \text{Pr}, \text{Nd}, \text{Sm}, \text{Eu}, \text{Gd}$ ), and report the single crystal growth of this high entropy oxide for  $Ln=\text{Nd}$ . We note that a high entropy material, sometimes known as a multiple principle element alloy, is one with a high configurational entropy term, i.e. a large positive  $\Delta S$  due to compositional disorder. This is related to, but separate from, “entropy stabilized” materials, where a positive  $\Delta S$  overcomes a positive  $\Delta H$  of formation to provide stability (a distinction that sometimes causes confusion in the field). The formula is derived from the pyrochlore form as  $(\text{Ta}_{0.75}\text{Mg}_{0.25})_2(\text{Nd}_{0.75}\text{Mg}_{0.25})_2\text{O}_7$ . These materials are related to the previously reported high temperature pyrochlore  $\text{Mg}_2\text{TaLaO}_6$ , where the Ta/La disorder was proposed to help optimize parameters for dielectric application. [15] We show that this series of pyrochlores exhibit paramagnetic behavior down to  $T=2$  K, as well as further expand the family to include magnetic transition metals in replace of Mg. This provides substantial tunability of the magnetic response, and may find use in developing new devices, e.g. cryogenic microwave isolators and filters. Furthermore, this demonstrates the feasibility of using laser-based floating zone techniques to grow single crystals of high entropy oxides, potentially leading to transformative advances in devices utilizing such oxides.

## Experimental Procedure

### Powder Synthesis of $A_2\text{Ta}_3\text{Ln}_3\text{O}_{14}$ ( $A=\text{Mg, Co, Mn, Zn}$ ; $\text{Ln}=\text{La, Pr, Nd, Sm, Eu, Gd}$ )

Starting reagents of  $\text{Ln}_2\text{O}_3$  ( $\text{Ln}=\text{La, Nd, Sm, Eu, Gd}$ ) (Alfa Aesar, 99.99% REO basis, NOAH Technologies, 99.9% REO basis, Alfa Aesar, 99.99% REO basis, Beantown Chemical, 99.99% REO basis, Alfa Aesar, 99.9% REO basis),  $\text{Pr}_6\text{O}_{11}$  (Alfa Aesar, 99.9% REO basis), and  $\text{MgO}$  (NOAH Technologies, 99.99%) were dried at  $T \approx 1000^\circ\text{C}$  for 24 hours so as to remove water that normally manifests as  $\text{Ln}(\text{OH})_3$ .  $\text{MgO}$  was also replaced with  $\text{Co}_3\text{O}_4$  (NOAH Technologies 99.5%),  $\text{ZnO}$  (NOAH Technologies, 99.999%), and  $\text{Mn}_3\text{O}_4$  (NOAH Technologies, 99.9%) for further synthesis in the family, following a similar procedure. Powders were intimately mixed with  $\text{Ta}_2\text{O}_5$  (NOAH Technologies, 99.99%) in stoichiometric ratios of approximately 500 mg total in an agate mortar and pestle. The mixed powders were then heated in alumina crucibles in a tube furnace for 12 hours at  $T \approx 1450^\circ\text{C}$  ramping both up and down in temperature at a rate of  $100^\circ\text{C}/\text{hr}$ . After an initial firing, sample was reground at heated again at  $T \approx 1450^\circ\text{C}$  for 12 hours, upon which Powder X-Ray Diffraction (PXRD), was used to confirm phase purity.

### Powder Synthesis of $\text{Ni}_2\text{Yb}_3\text{Sb}_3\text{O}_{14}$

Approximately 500 mg total of stoichiometric powders of  $\text{Ni}(\text{NO}_3)_2 \cdot 6\text{H}_2\text{O}$  (Alfa Aesar, 98% pure),  $\text{Yb}_2\text{O}_3$  (Alfa Aesar, 99.9% pure), and  $\text{Sb}_2\text{O}_3$  (NOAH Technologies, 99.9% pure) were initially dissolved in 1 M  $\text{HNO}_3$ . The  $\text{HNO}_3$  solution was boiled to remove liquids and the remaining powder was ground up, calcined in alumina crucibles at  $T \approx 400^\circ\text{C}$  for 12 hours, reground, and then heated in a tube furnace at  $T \approx 1450^\circ\text{C}$  for 12 hours ramping both up and down in temperature at a rate of  $100^\circ\text{C}/\text{hr}$ . After a first firing, sample was reground for a second firing at  $T \approx 1450^\circ\text{C}$ , using PXRD to confirm phase purity.

## Single Crystal Growth of $\text{Mg}_2\text{Ta}_3\text{Nd}_3\text{O}_{14}$

Polycrystalline  $\text{Mg}_2\text{Ta}_3\text{Nd}_3\text{O}_{14}$  was compacted into rod shapes using rubber balloons, put under vacuum, and subsequently subjected to hydrostatic pressure. Upon removal from the balloon, the rod was sintered at  $T \approx 1450^\circ \text{ C}$  in an open alumina boat in a tube furnace for 12 hours. Resulting rods were mounted in a Laser Diode Floating Zone (LDFZ) furnace (Crystal Systems, Inc., FD-FZ-5-200-VPO- PC) with  $5 \times 200$  W GaAs lasers ( $\lambda = 976 \text{ nm}$ ), with the seed rod mounted using Nichrome wire on an alumina holder attached to the lower shaft and the feed rod suspended from Nichrome wire attached to a hook on the upper shaft. The seed rod was melted, whereupon the feed rod was joined to create a stable molten zone. Both rods were translated downward at a rate of 5 mm/hr, with both counter-rotating at 10 rpm each, under flowing  $\text{Ar}_{(\text{g})}$  at 1.5 L/min with the lasers tilted at  $5^\circ$  above the plane.

## Characterization

Single crystals were oriented using backscattered X-ray Laue diffraction with a tungsten source operating at 10 kV and 10 mA with a Multiwire Laboratories MWL 110 real-time back reflection Laue camera. Laboratory-based X-ray diffraction patterns of the powders and ground up single crystals were collected using a Bruker D8 Focus diffractometer with  $\text{Cu } K_\alpha$  radiation and a LynxEye position sensitive detector. Rietveld refinements to check phase purity and extract unit cell parameters were performed using Bruker TOPAS software (Version 4.2, Bruker AXS). Single crystal x-ray diffraction (SXRD) data was collected using a SuperNova diffractometer (equipped with an Atlas detector) employing  $\text{Mo } K_\alpha$  radiation ( $\lambda = 0.71073 \text{ \AA}$ ) under the CrysAlisPro software package (version 1.171.36.28, Agilent Technologies, 2012). The structure was solved using DIRDIF-2008, with refinements done using SHELXL-97. [16, 17] After initial refinements an empirical absorption correction with spherical harmonics implemented in SCALE3 ABSPACK scaling algorithm was used, with

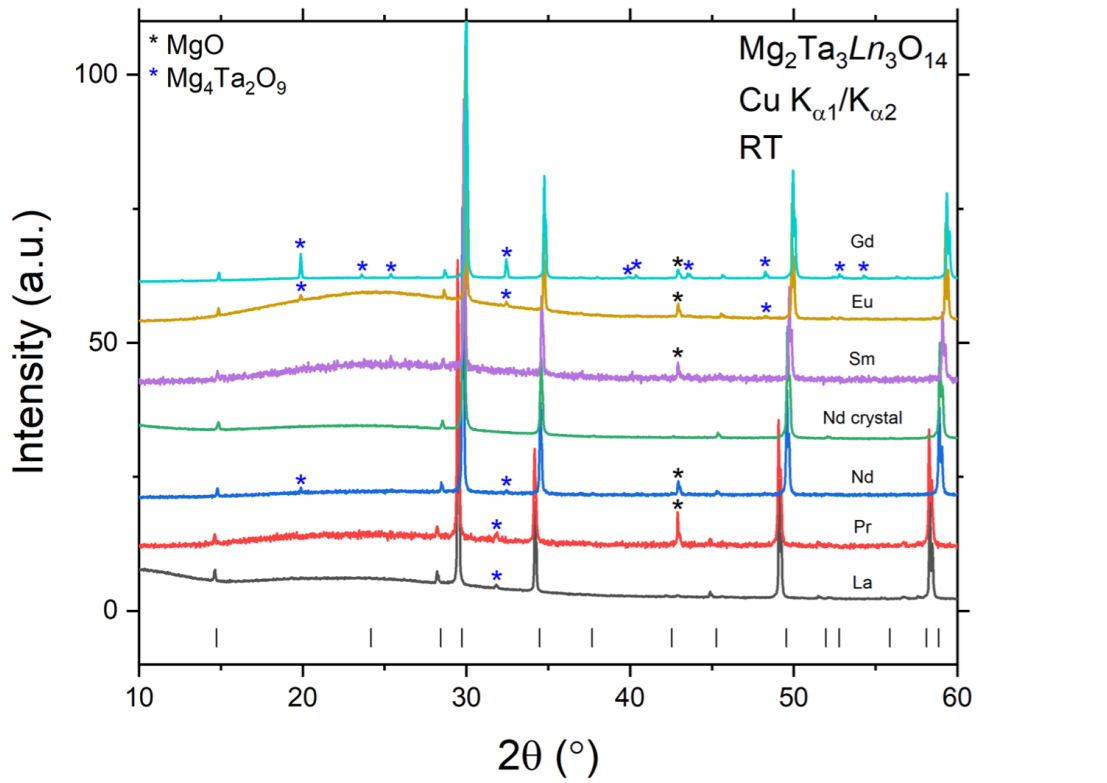


**Figure 3-1.** PXRD data of initial synthetic attempts for  $\text{Mg}_2\text{Ta}_3\text{Ln}_3\text{O}_{14}$  compounds, scaled according to the largest peak, with tick marks showing the allowed ( $hkl$ ) reflections. The impurities that arise when targeting  $\text{Mg}_2\text{Ta}_3\text{Ln}_3\text{O}_{14}$  are denoted with an asterisk symbols and disappear when the appropriate stoichiometry is targeted.

weighting schemes applied near the end of refinements. [18]

Magnetization measurements were carried out on both powder and crystal samples using a Quantum Design Physical Properties Measurement System (PPMS) with the ACMS option from  $T=2$ –300 K. Heat capacity measurements were also taken in the PPMS using the semi-adiabatic pulse method. The crystal structures were rendered using Vesta software. [19]

Formula	$\text{Mg}_2\text{Ta}_3\text{Nd}_3\text{O}_{14}$					
Crystal System	Cubic					
Space Group	$Fd - 3m$ (no. 227), setting 2					
$a$ (Å)	10.3967(2)					
$V$ (Å)	1123.79(4)					
$Z$	8					
Radiation	Mo $K_{\alpha}$ , $\lambda=0.71073$ Å					
Temperature (K)	293					
Adsorption Coefficient	44.56					
$F(0\ 0\ 0)$	2189					
Reflections collected/unique/internal data agreement	6793/129 $R_{\text{int}}=0.037$					
Data/parameters	129/13					
Goodness-of-fit	1.243					
$R = \sum   F_o  -  F_c   / \sum  F_o $	0.018					
$wR(F^2) = [\sum w(F_o^2 - F_c^2)^2 / \sum w(F_o^2)^2]^{1/2}$	0.052					
Largest diff. peak and hole	0.949 and -0.563 e Å <sup>-3</sup>					
	Occ.	Wyckoff Positions	x (Å)	y (Å)	z (Å)	$U_{\text{iso}}$ (Å <sup>2</sup> )
Mg1	0.23(3)	16c	0	0	0	0.0193(8)
Nd	0.77(3)	16c	0	0	0	0.0193(8)
Mg2	0.22(3)	16d	0.5	0.5	0.5	0.0171(7)
Ta	0.78(3)	16d	0.5	0.5	0.5	0.0171(1)
O1	1	48f	0.4234(4)	0.6250	0.6250	0.0214(11)
O2	1	8a	0.1250	0.1250	0.1250	0.039(3)

**Table 3-I.** Crystallographic parameters of the SXRD for  $\text{Mg}_2\text{Ta}_3\text{Nd}_3\text{O}_{14}$

## Results and Discussion

Figure 3-1 shows the PXRD of the family  $\text{Mg}_2\text{Ta}_3Ln_3\text{O}_{14}$  ( $Ln=\text{La}, \text{Pr}, \text{Nd}, \text{Sm}, \text{Eu}, \text{Gd}$ ), targeted using the formula  $\text{Mg}_2\text{Ta}Ln\text{O}_6$ , following a previous report. [15] This original solution has a missing oxygen, which can occur for the defect pyrochlore structure. However, while the formula  $\text{Mg}_2\text{Ta}Ln\text{O}_6$  works from a charge balancing perspective, targeting this stoichiometry consistently led to impurities of  $\text{MgO}$  and  $\text{Mg}_4\text{Ta}_2\text{O}_9$ , which are visibly present in all the families. Further synthesis attempts were done varying the defect concentrations while following charge balance rules to derive the true chemical formula. This led to an arrival of the form  $\text{Mg}_2\text{Ta}_3Ln_3\text{O}_{14}$ , as evidenced in  $Ln=\text{Nd}$ , which became the focus for further study.

With appropriate stoichiometry, the structure is pure phase, as seen from the

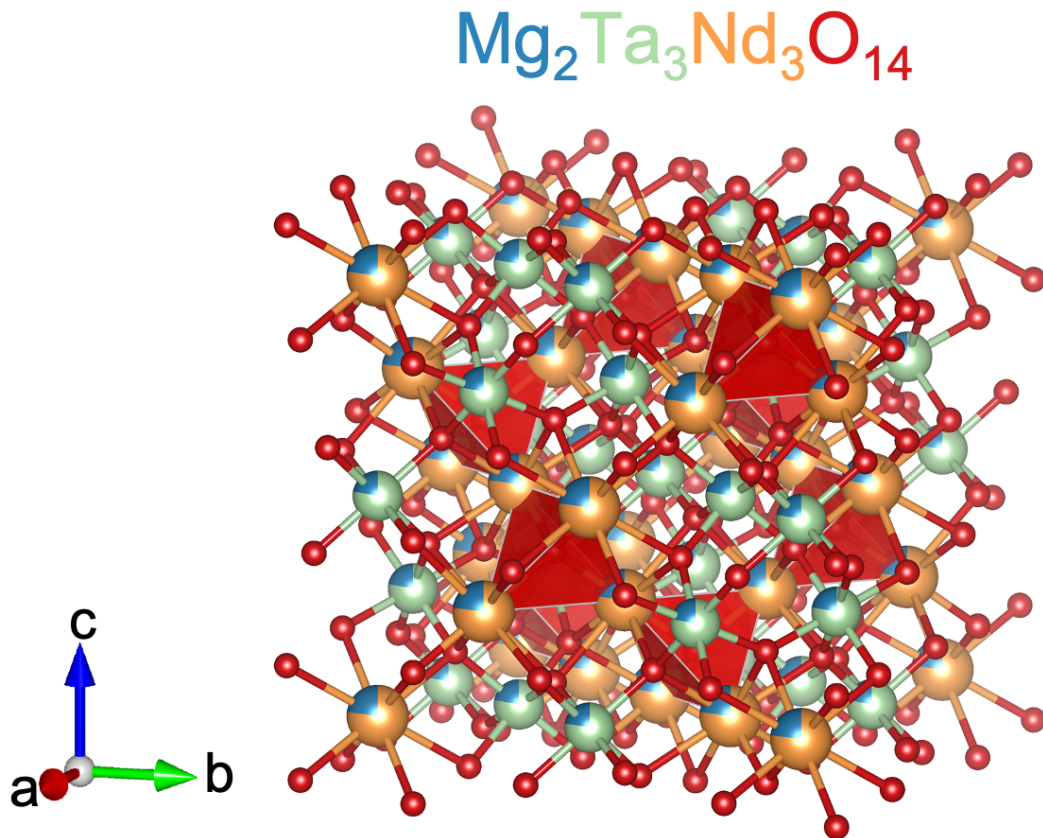


**Figure 3-2.** The crystal structure of the defect pyrochlore, with the corner-sharing tetrahedra being shown between the Nd atoms.

PXRD of a powdered single crystal of  $Ln=\text{Nd}$ , also shown in Figure 3-1. No residual  $\text{MgO}$  or other secondary phases are observed in this pattern, as compared to the PXRD for  $Ln=\text{Nd}$  when targeting  $\text{Mg}_2\text{TaNdO}_6$ . The structure, solved via single crystal x-ray diffraction, is found to be a partially disordered pyrochlore, space group Fd-3m. Full crystallographic parameters from the single crystal structure solution are shown in Table 3-I. Rietveld refinement of the PXRD of the Nd crystal using the solved parameters from single crystal x-ray diffraction gives a fit closely matching the experimental data, with no significant change in the overall fit or  $R_{wp}$  value when allowing occupancies to refine. Both sets of data are consistent with the proposed chemical formula of  $\text{Mg}_{2-(x+y)}\text{Ta}_{3+x}\text{Ln}_{3+y}\text{O}_{14+1.5x+0.5y}$  ( $Ln=\text{La, Pr, Nd, Sm, Eu, Gd}$ ), with  $x=0.08$  and  $y=0.12$  for the case of  $Ln=\text{Nd}$ .

The structure, as shown in Figure 3-2, is a typical pyrochlore, with the Mg randomly substituted on both the A and B sites. This is unlike the family  $Mg_2Sb_3Ln_3O_{14}$ , where the Mg is an ordered substitution which results in a kagomé lattice. [10] This compound, while a defect pyrochlore, is distinct from the fluorite structure as it maintains the characteristic pyrochlore-only reflections in the x-ray diffraction patterns. Related, the deviation of the x coordinate on the O1 site is also an indicator to the pyrochlore-like nature of a compound. In the case of  $Mg_2Ta_3Ln_3O_{14}$ , the x parameter refined to 0.4234(4), substantially away from the value of 0.375 required for a fluorite, showing that this compound does conform to typical pyrochlore classification. [6]

When comparing the average effective radii for the different lanthanides, the A site ranges from 1.01 to 1.10 Å, while the B site is 0.69 Å. [20] Predicting the stability of the pyrochlore phase by calculating  $R_A/R_B$ , popularized by Subramanian, gives a ratio ranging from: 1.46 to 1.59, which lies within the pyrochlore stability regime ( $1.36 < R_A/R_B < 1.71$ ). [6, 21]  $Mg_2Ta_2O_7$  is reported to exist as a pyrochlore above  $T \approx 1400^\circ C$ . [22] An increase in the in the  $R_A/R_B$  (from 1.39 for  $Mg_2Ta_2O_7$  to 1.46 for  $Mg_2Ta_3Gd_3O_{14}$ ) shows that it is likely a combination of chemical pressure and entropy that stabilizes this family.

The ability to substitute Mg for other elements shows the flexibility of the pyrochlore structure is maintained, as evidenced by the use of Zn, Co, Mn, and Ni. The Ni variant was only able to be substituted for the compound  $Ni_{1.5}Yb_{3.25}Sb_{3.25}O_{14.5}$ , whose chemical formula was found by experimentally varying the defect concentration and arranging the formula according to charge balance rules. No residual NiO is visibly detected in the PXRD of the sample. If one considers the average effective radii for the A and B site, the  $R_A/R_B$  ratio comes out to be 1.39, putting it near the edge of the pyrochlore stability regime. The ability to simultaneously substitute both A and B sites with elements that have an overall spin in the +2 oxidation state is shown with Co, Mn, and Ni.

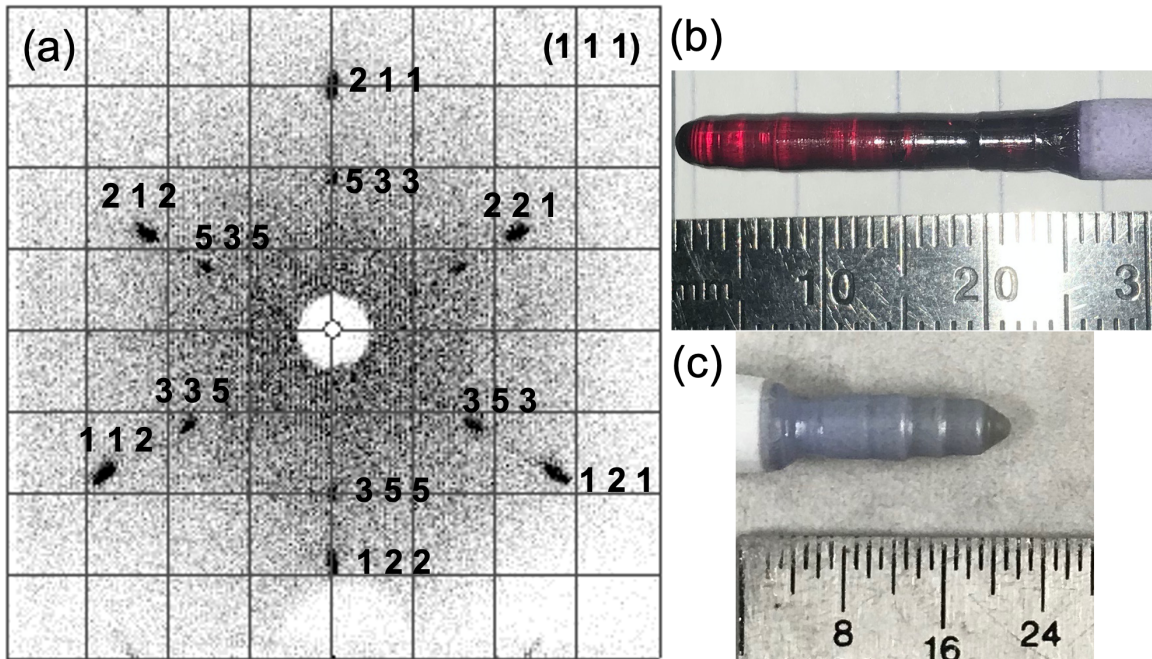


**Figure 3-3.** (a) Laue image of the  $\text{Mg}_2\text{Ta}_3\text{Nd}_3\text{O}_{14}$  crystal aligned along the (111) plane with the various ( $hkl$ ) indices labeled appropriately. This image shows well defined spots and no evidence of twinning. (b)  $\text{Mg}_2\text{Ta}_3\text{Nd}_3\text{O}_{14}$  crystal as grown in  $\text{Ar}_{(\text{g})}$ . (c) Another crystal of  $\text{Mg}_2\text{Ta}_3\text{Nd}_3\text{O}_{14}$  as grown in  $\text{O}_{2(\text{g})}$ .

Figure 3-3(a) shows a typical Laue image taken from a single crystal of  $\text{Mg}_2\text{Ta}_3\text{Nd}_3\text{O}_{14}$  grown in the LDFZ furnace. Images collected along the length of the rod indicate a uniform single crystal region approximately 5 mm OD x 2.5 cm length with no evidence of twinning. The as-grown crystal is a ruby red color, shown in Figure 3-3(b). This is likely due to an oxygen deficiency from growth in  $\text{Ar}_{(\text{g})}$ . The color of the crystal as grown in  $\text{O}_{2(\text{g})}$ , shown in Figure 3-3(c), is a light blue (the expected color from crystal field transitions within the Nd ions). This color change demonstrates the tunability of the oxygen concentration. Further evidence of this being due to oxygen stoichiometry is demonstrated in an annealing experiment using thermogravimetric analysis (TGA) whereupon heating under flowing  $\text{O}_{2(\text{g})}$  the crystal changes from the red to a purple (approaching the original blue). The TGA data also shows a significant uptake in mass upon annealing, shown in Figure 3-4. Future work should elucidate the precise nature and origin of this color change and explore the possible use as the

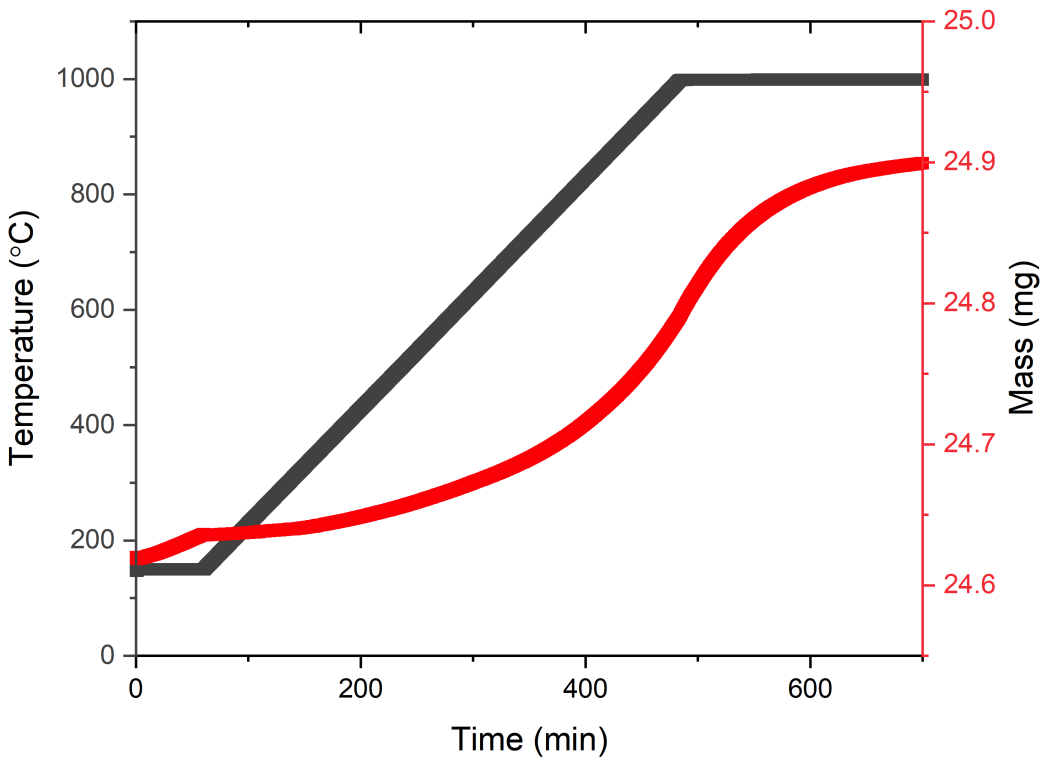


**Figure 3-4.** Annealing of oxygen deficient  $\text{Mg}_2\text{Ta}_3\text{Nd}_3\text{O}_{14}$  as measured using thermo-gravimetric analysis shows significant uptake in mass as the sample regains lost oxygen.

active element in a optical-based oxygen sensor. [23]

Crystal growth of high entropy materials (more specifically high entropy oxides) is a developing process in the field. [24, 25] The ability to easily grow single crystals on the scale of centimeters as shown here using the LDFZ furnace broadens the characterization tools available for the study of such materials. Further, the ability to tune both the cation and oxygen defect concentration provides a system where we can grow single crystals with the lattice parameter tailored to a desired application as a substrate. An example of this could be considered for the iridate pyrochlore  $\text{Bi}_2\text{Ir}_2\text{O}_7$ , where interactions between the spin orbit coupling and strongly correlated electrons could lead to novel topological states. [26] The ability to create lattice-mismatch precisely using these high entropy oxides can impact these interactions to access the

<i>Ln</i>	Fit Temperature Range	$p_{eff}$	$\Theta_{CW}$
Pr	2-20	0.393(6)	-3.2(2)
Nd	100-300	2.86(1)	-18.2(8)
Sm	2-20	0.424(2)	-1.60(5)
Eu	150-300	5.05(4)	-360(3)
Gd	150-300	8.264(9)	-3.5(3)

**Table 3-II.** Curie-Weiss fits done on magnetization measurements of the  $Mg_2Ta_3Ln_3O_{14}$  series as powders.

regime where these topological states lie.

The  $Mg_2Ta_3Ln_3O_{14}$  compounds all demonstrate paramagnetic behavior, with  $Ln=Eu$  showing Van Vleck paramagnetism. [27] Curie Weiss (CW) fits were done on the series of powders, with the resulting values shown in Table 3-II.  $Ln=Pr$  and  $Sm$  were fit at lower temperature ranges due to the low-lying crystal field levels. The  $p_{eff}$  value for  $Ln=Pr$ ,  $Nd$ , and  $Sm$  all are lower than their expected values of  $p_{obs}=3.5$ ,  $3.5$ , and  $1.5$  respectively, while  $Ln=Eu$  and  $Gd$  both are higher than the expected values of  $p_{obs}=3.4$  and  $8.0$ . [28] These discrepancies are common for some of the lanthanides, such as  $Sm$ , and can be accounted for due to a complex set of crystal fields caused by the variety of local chemical environments present in the compositional disorder. [10]

The DC magnetization data on the as-grown single crystal for  $Ln=Nd$ , presented in Figure 3-5, also demonstrates paramagnetic behavior. A fit to the CW law from  $T = 100$  to  $300$  K gives  $\Theta_{CW} = 21.7(4)$  K with an effective magnetic moment of  $p_{eff}=3.19(1)/Nd$  atom. The effective magnetic moment matches reasonably well with the observed magnetic moment for  $Nd$  of  $3.5$ . [28] The Weiss temperature, a measure of the net mean field interaction strength, of  $-21.7(4)$  K is higher than many comparable  $Nd$  compounds, and suggestive of low lying crystal field excitations. A CW analysis from  $T = 2$  K to  $T = 20$  K, gives  $p_{eff}=2.59(1)/Nd$  atom and  $\Theta_{CW}=-0.32(2)$  K, comparable to the  $Nd$  systems at low temperature shown in Table 2, and consistent with a much smaller mean field interaction. Given the first crystal field level for  $Nd$  pyrochlore derivatives is at  $\sim 20$  meV ( $T \approx 200$  K), it significantly alters the magnetic

Compound	$\text{Nd}_2\text{Zr}_2\text{O}_7$ [31]	$\text{Nd}_2\text{Pb}_2\text{O}_7$ [32]	$\text{Mg}_2\text{Nd}_3\text{Sb}_3\text{O}_{14}$ [30]	$\text{Mg}_2\text{Ta}_3\text{Nd}_3\text{O}_{14}$
Temperature (K)	1.8-10	0.15-15	1.8-10, 150-300	2-20, 100-300
$\Theta_{CW}$ (K)	0.200(8)	-0.069(4)	-0.12(1), -54.5(5)	-0.32(2), -21.7(4)
$p_{eff}$	2.543(2)	2.55(7)	2.50(5), 3.56(5)	2.59(1), 3.19(1)

**Table 3-III.** A list of comparable Nd compounds and their corresponding Weiss temperatures and effective magnetic moments over the listed temperature range.

	$A_2\text{Ta}_3\text{Nd}_3\text{O}_{14}$	Mg	Co	Mn
C	1.265(3)	7.31(2)	11.521(9)	
$\Theta_{CW}$	-20.6	-8.8(4)	-26.4(2)	

**Table 3-IV.** The constants obtained from CW fits of  $A_2\text{Ta}_3\text{Nd}_3\text{O}_{14}$  ( $A=\text{Mg, Co, Mn}$ ) can be used to create a normalized plot for comparison.

response above  $T \approx 20 - 50$  K. [29, 30] A higher  $p_{eff}$  is seen in our as-grown crystal compared to the powder Nd sample, likely due to crystalline anisotropy from the measurement of the single crystal magnetization along a single (but not experimentally defined) axis.

In order to see the impact of adding magnetic ions on both the A and B sites, a comparative study was done on the series  $A_2\text{Ta}_3\text{Nd}_3\text{O}_{14}$  ( $A=\text{Mg, Co, Mn}$ ). The data was normalized according to the rearranged CW formula Equation 2.12. Figure 3-6 shows that all three compounds demonstrate similar CW behavior to each other, with deviation from the CW law occurring at low temperature. The constants used for this normalization are shown in Table 3. Further studies should be done on the tunability between the magnetic and nonmagnetic defects to see their impact on magnetic response.

Heat capacity measurements can be used both as a sensitive bulk probe of magnetism, but also to explore phonon and lattice dynamics. [33–35] Figure 3-7 shows the heat capacity data for  $Ln=\text{Nd}$  from  $T = 2$  to 20 K. It shows an upturn at the lowest temperature, likely due to the loss of some magnetic entropy, possibility indicative of approaching magnetic order. This can be quantitatively modeled using a combination of a two-level (Schottky) system separated by an energy gap  $\Delta$ , combined with  $T^3$

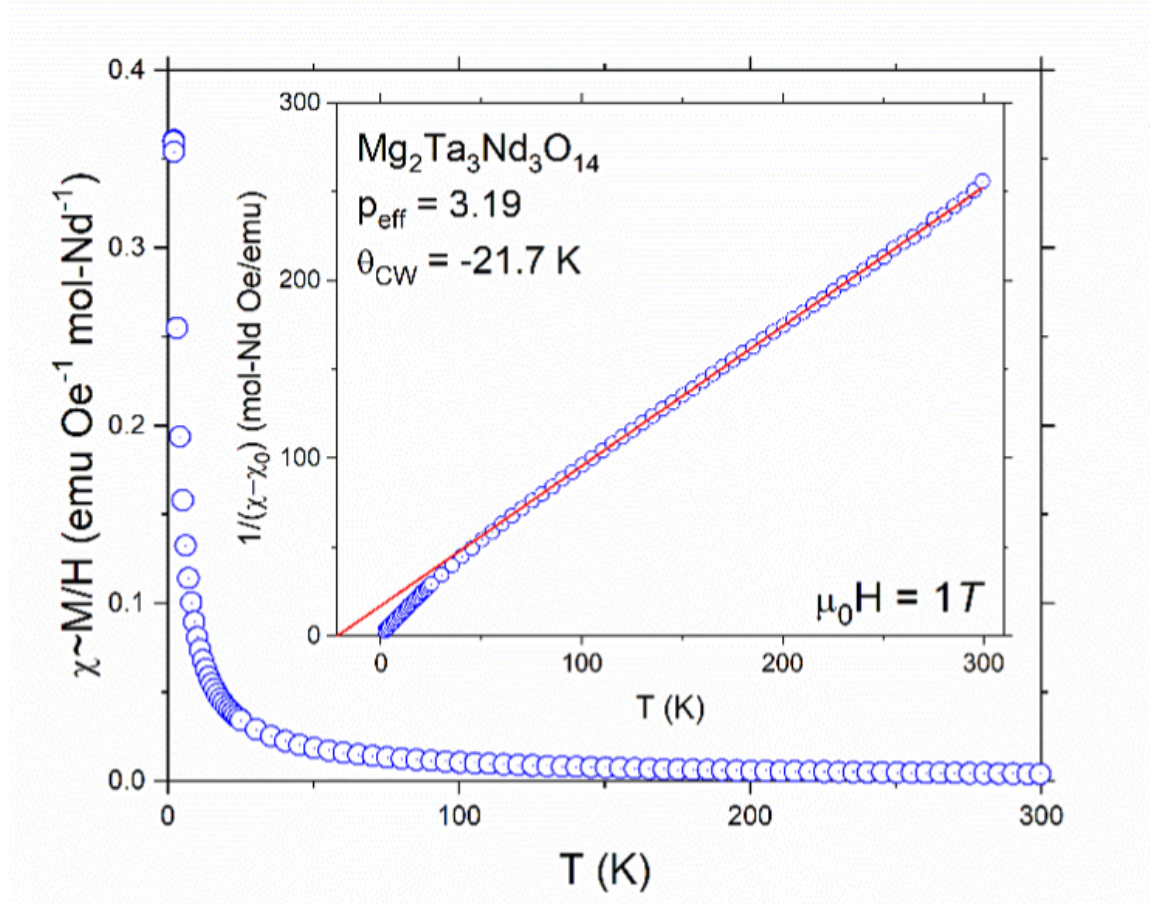


**Figure 3-5.** The DC magnetic susceptibility of a crystal of  $\text{Mg}_2\text{Ta}_3\text{Nd}_3\text{O}_{14}$  with  $\chi$  estimated as  $M/H$ . The inset shows the Curie-Weiss fit to the data. No magnetic order is apparent in this data.

and  $T^5$  terms for phonon contributions:

$$C_v = R \frac{\Delta^2}{T} \frac{e^{\frac{\Delta}{T}}}{[1 + e^{\frac{\Delta}{T}}]^2} + \beta_3 T^3 + \beta_5 T^5 \quad (3.1)$$

Where  $\Delta$  is related to the energy splitting between the two levels,  $\beta_3$  and  $\beta_5$  relate to the low temperature approximation for the Debye equation. [36] The resulting values to the fit are:  $\Delta=1.680(6)$  K,  $\beta_3=0.55(3)$  mJ K $^{-4}$  mol,  $\beta_5=1.4(1)$   $\mu\text{J K}^{-6}$  mol. At higher temperatures, where  $T \gg \Delta$ , the Schottky anomaly does not contribute much to the overall heat capacity. This matches with the data, as the Schottky contribution is most significant at  $T=2$  K, close to the size of the energy gap. The  $\beta_3$  relates to

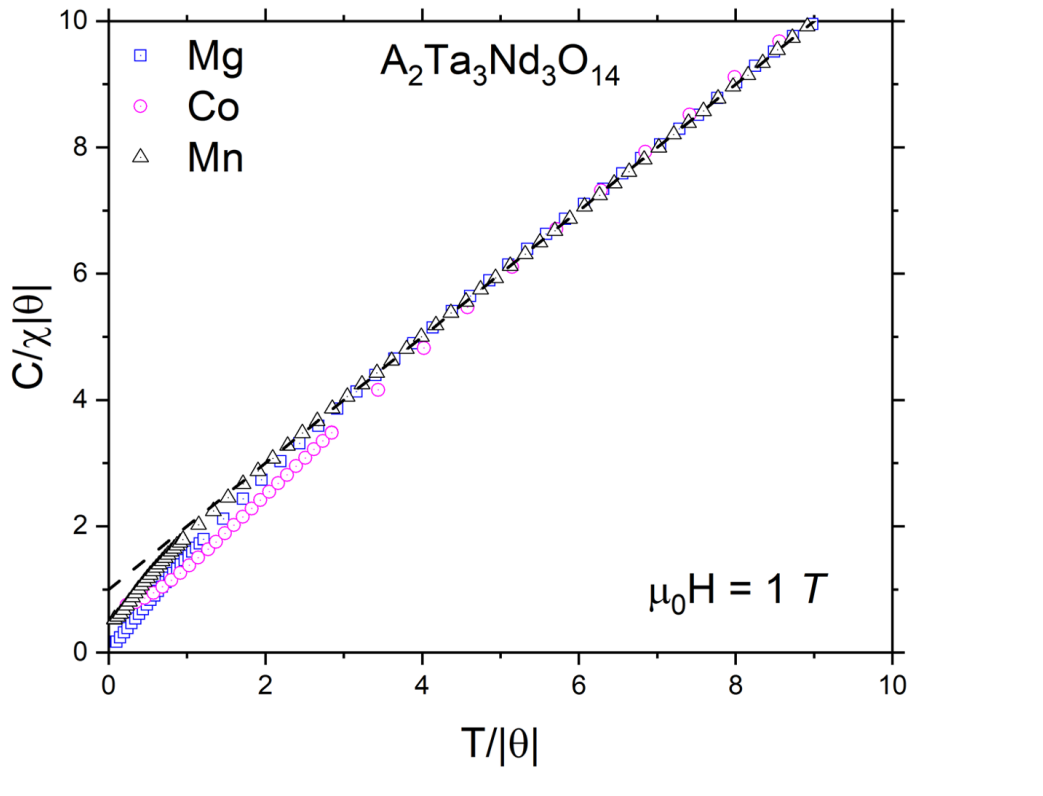


**Figure 3-6.** A dimensionless, normalized plot of  $A_2\text{Ta}_3\text{Nd}_3\text{O}_{14}$  ( $A=\text{Mg}, \text{Co}, \text{Mn}$ ). All analogs display CW behavior with antiferromagnetic deviations occurring at low temperatures. The dashed black line serves as a paramagnetic CW guide to the eye.

the Debye temperature as follows:

$$C_v = \frac{12\pi^4}{5} \frac{Rs}{\theta_D^3} T^3 = \beta_3 T^3 \quad (3.2)$$

In this equation R represents the molar gas constant and s represents the number of atoms per formula unit. This leads to an estimate of the Debye temperature to be  $\theta_D=426$  K.

Additional information on the phonon and lattice dynamics can be obtained by exploring the heat capacity up to  $T=300$  K, shown in Figure 3-8. The nonmagnetic analogue of the Nd variant,  $\text{Mg}_2\text{Ta}_3\text{La}_3\text{O}_{14}$  was synthesized and used for comparison. The heat capacity for both compounds was fit using a combination of Debye and Einstein terms from equations 2.6 and 2.7. The data was plotted as  $C_p/T^3$  vs.  $\log(T)$

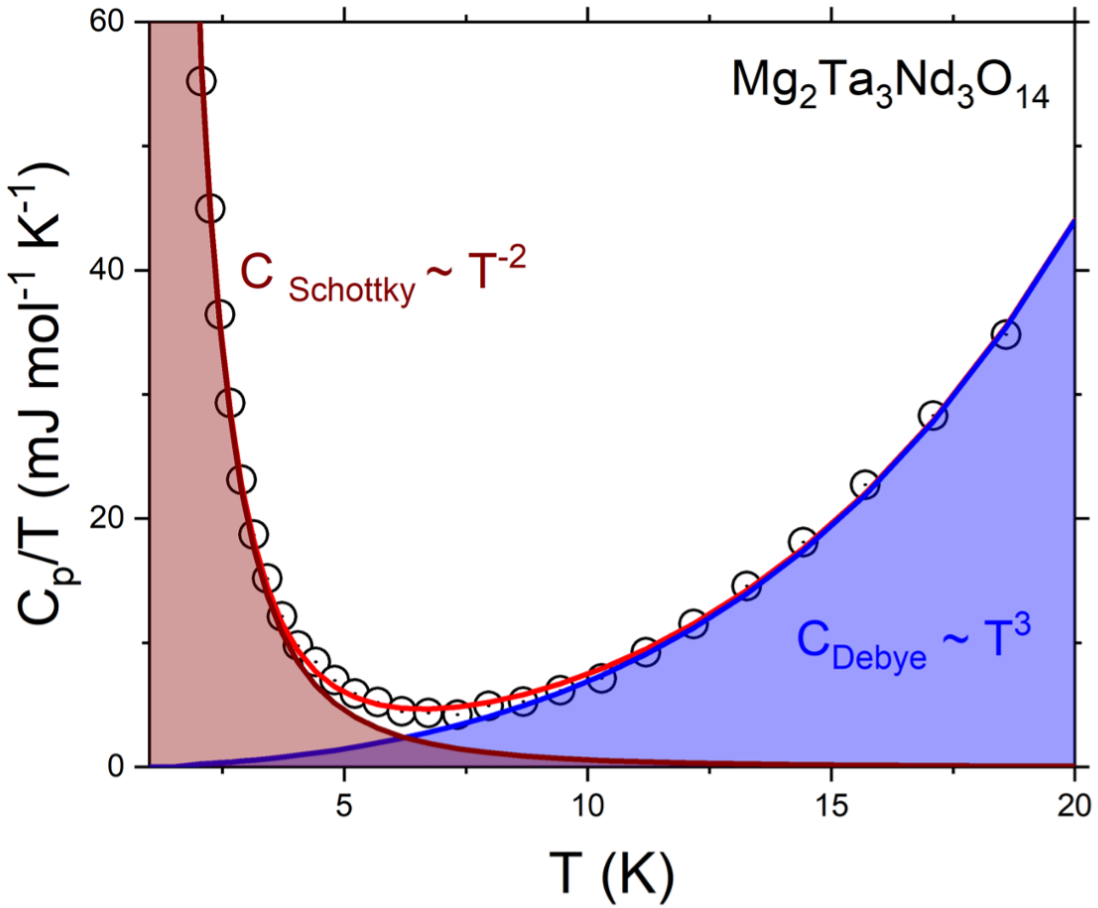


**Figure 3-7.** The low temperature heat capacity is fit to 3.1 with the Schottky and Debye contributions highlighted.

to emphasize these modes. The resulting terms are represented in Table 3-V, with uncertainties derived from the standard error of the fit.

The total number of oscillators for  $Ln=La$  and  $Ln=Nd$  add up to 19(2) and 22.8(4) respectively. Compared to the theoretical value of approximately 22, the  $Ln=La$  compound is slightly underfitting, while the  $Ln=Nd$  compound matches close to the actual value. Both compounds can be well-described by three Debye modes and one Einstein mode, reflected in the peak close to  $T=25$  K, a feature observed in other disordered pyrochlores. [37] The difference in the high temperature Debye terms could explain the poor matching between the two at higher temperatures when attempting

<i>Ln</i>	La	Nd
s	3.8(1)	4.67(8)
$\theta_{D1}$ (K)	232(2)	258(1)
s2	7(1)	11.1(3)
$\theta_{D2}$ (K)	518(34)	568(8)
s3	8(2)	6.1(3)
$\theta_{D3}$	821(59)	1400(110)
se	0.744(5)	0.998(3)
$\theta_E$ (K)	106.1(3)	110.9(1)
Sum of oscillators	19(2)	22.8(4)

**Table 3-V.** The fitting parameters to the  $C_p/T^3$  data for both  $Ln=La$  and  $Ln=Nd$ .

to subtract out the phonon contribution. This large difference can be attributed to a need for higher temperature heat capacity data to accurately fit the terms. In spite of this difference in number of oscillators, a plot of the phonon density of states (Figure 3-8(c)) shows that the spectral weight is higher in energy for  $Ln=La$  (even at lower phonon energies). This is indicative of a stiffer lattice for the Nd compound, which is the opposite of what one would expect. Further, comparing the two shows the high temperature heat capacity for the  $Ln=Nd$  compound can be attributed to just a phonon contribution, with no magnetic contribution arising above T=2 K besides what is fit to a two level Schottky anomaly.

## Conclusion

The family  $A_2Ta_3Ln_3O_{14}$  has been synthesized in powder form, with the ability to easily grow single crystals of high entropy oxides demonstrated using the LDFZ. The flexible structure of this family demonstrates the ability to design new pyrochlore compounds with intended defects. These magnetically disordered compounds have so far shown no deviation from paramagnetic behavior upon substitution of defects. The heat capacity data demonstrates no phase transitions down to T=2 K, with the presence of a Schottky anomaly at low temperatures and a low temperature Einstein mode at  $T \approx 25$  K. Further studies should be done to expand upon the

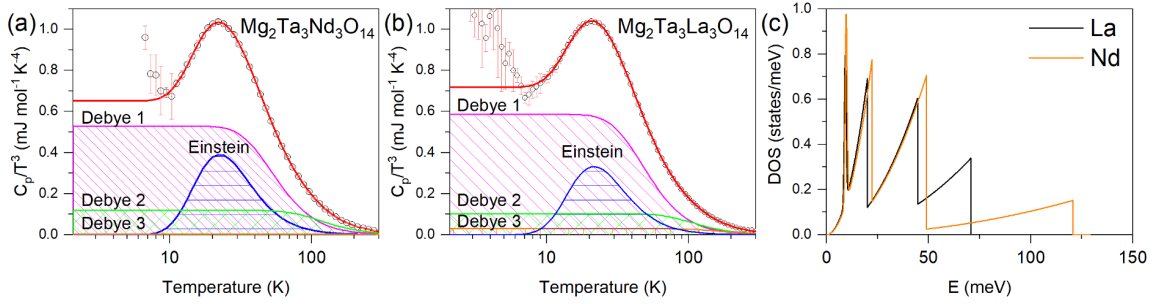


**Figure 3-8.** The phonon contribution to the heat capacity of (a)  $\text{Mg}_2\text{Ta}_3\text{Nd}_3\text{O}_{14}$  and (b)  $\text{Mg}_2\text{Ta}_3\text{La}_3\text{O}_{14}$  is fit to a combination of three Debye modes and one Einstein mode. The fit extends up to  $T=300$  K and shows no excess contribution to heat capacity as seen beyond the upturn at low temperatures that can be modeled using a two-level Schottky anomaly. A plot of the phonon density of states (c) shows the phonon modes for  $Ln=\text{Nd}$  shift to higher energy, even at lower phonon energies, indicating a stiffening of the lattice for  $Ln=\text{Nd}$  relative to  $Ln=\text{La}$ .

current work in understanding the local order in pyrochlores concerning the transition between ordered and disordered substitutions. [23] The capabilities of this family as wide-band-gap insulators to contain deliberate defects should be furthered pursued as a design principle in applications of controlled spin centers. [38]

## Associated Content

The raw data involved in this work is accessible at <https://data.paradim.org/99002>

## Acknowledgements

This work was funded by the Platform for the Accelerated Realization, Analysis, and Discovery of Interface Materials (PARADIM), a National Science Foundation Materials Innovation Platform (NSF DMR-1539918). Angela Torrejon gratefully acknowledges that research was sponsored by the Army Educational Outreach Program (AEOP) and was accomplished under AEOP Research & Engineering Apprenticeship Program FY20 Site Agreement. The views and conclusions contained in this document are those of the authors and should not be interpreted as representing the official policies,

either expressed or implied, of the Army Educational Outreach Program or the U.S. Government. The U.S. Government is authorized to reproduce and distribute reprints for Government purposes notwithstanding any copyright notation herein. L.A.P. would like to thank Dr. Maxime Siegler for helping with single crystal data collection, Veronica Stewart with assistance in PPMS measurements, and Juan Chamarro, Hector Vivanco, Tanya Berry, and Mekhola Sinha for their helpful conversations relating to heat capacity analysis.

# References

1. Rau, J. G. & Gingras, M. J. P. Frustrated Quantum Rare-Earth Pyrochlores. *Annual Review of Condensed Matter Physics* **10**, 357–386 (2019).
2. Broholm, C. L. *et al.* Quantum Spin Liquids. *Science* **367** (2020).
3. Bramwell, S. T. & Gingras, M. J. P. Spin Ice State in Frustrated Magnetic Pyrochlore Materials. *Science* **294**, 1495–1501 (2001).
4. Ishikawa, J. J., O'Farrel, E. C. T. & Nakatsuji, S. Continuous Transition Between Antiferromagnetic Insulator and Paramagnetic Metal in the Pyrochlore Iridate  $\text{Eu}_2\text{Ir}_2\text{O}_7$ . *Physical Review B* **85** (2012).
5. Arpino, K. E., Trump, B. A., Scheie, A. O., McQueen, T. M. & Koohpayeh, S. M. Impact of Stoichiometry of  $\text{Yb}_2\text{Ti}_2\text{O}_7$  on its Physical Properties. *Physical Review B* **95** (2017).
6. Subramanian, M. A., Aravamudan, G. & Subba Rao, G. V. Oxide Pyrochlores-A Review. *Progress in Solid State Chemistry* **15** (1983).
7. Sanders, M. B., Krizan, J. W., Plumb, K. W., McQueen, T. M. & Cava, R. J.  $\text{NaSrMn}_2\text{F}_7$ ,  $\text{NaCaFe}_2\text{F}_7$ , and  $\text{NaSrFe}_2\text{F}_7$ : Novel Single Crystal Pyrochlore Antiferromagnets. *Journal of Physics: Condensed Matter* **29** (2016).
8. Raju, N. P., Gmelin, E. & Kremer, R. K. Magnetic-Susceptibility and Specific-Heat Studies of Spin-Glass-Like Ordering in the Pyrochlore Compounds  $\text{R}_2\text{Mo}_2\text{O}_7$  ( $\text{R}=\text{Y}$ ,  $\text{Sm}$ , or  $\text{Gd}$ ). *Physical Review B* **46** (1992).
9. Koohpayeh, S. M., Wen, J. .-, Trump, B. A., Broholm, C. L. & McQueen, T. M. Synthesis, Floating Zone Crystal Growth and Characterization of the Quantum Spin Ice  $\text{Pr}_2\text{Zr}_2\text{O}_7$  Pyrochlore. *Journal of Crystal Growth* **402** (2014).
10. Sanders, M. B., Baroudi, K. M., Krizan, J. W., Mukadam, O. A. & Cava, R. J. Synthesis, Crystal Structure, and Magnetic Properties of Novel 2D Kagome Materials  $\text{RE}_3\text{Sb}_3\text{Mg}_2\text{O}_{14}$  ( $\text{RE}=\text{La}, \text{Pr}, \text{Sm}, \text{Eu}, \text{Tb}, \text{Ho}$ ): Comparison to  $\text{RE}_3\text{Sb}_3\text{Zn}_2\text{O}_{14}$  Family. *Basic Solid State Physics* **253**, 2056–2065 (2016).
11. Gao, M. C., Yeh, J.-W., Liaw, P. K. & Yong, Z. *High-Entropy Alloys: Fundamentals and Applications* 1st (Cham: Springer International Publishing, 2016).
12. Jimenez-Segura, M. *et al.* Long-Range Magnetic ordering in Rocksalt-Type High-Entropy Oxides. *Applied Physics Letters* **114** (2019).
13. Dabrowa, J. *et al.* Synthesis and Microstructure of the  $(\text{Co,Cr,Fe,Mn,Ni})_3\text{O}_4$  High Entropy Oxide Characterized by Spinel Structure. *Materials Letters* **216**, 32–26 (2018).

14. Winiarski, M. J. & McQueen, T. M. Stabilization of the Pyrochlore Phase of  $Mn_2Sb_2O_7$  by Double Substitution. *Journal of Solid State Chemistry* **278** (2019).
15. Kumar, S. S., Nair, K. V. O. & James, J.  $Mg_2MTaO_6$  ( $M=Nd$  or  $La$ ): a Group of New Pyrochlore Oxides. *Journal of Solid State Chemistry* **177**, 3873–3878 (2004).
16. Farrugia, L. J. WinGX Suite for Small-Molecule Single-Crystal Crystallography. *Journal of Applied Crystallography* **32**, 837–838 (1999).
17. Sheldrick, G. M. A Short History of SHELX. *Acta Crystallographica A* **A64**, 112–122 (2008).
18. Clark, R. C. & Reid, J. S. The Analytical Calculation of Absorption in Multifaceted Crystals. *Acta Crystallographica A* **A51**, 887–897 (1995).
19. Momma, K. & Izumi, F. VESTA: a three-dimensional visualization system for electronic and structural analysis. *Journal of Applied Crystallography* **41**, 654–658 (2008).
20. Shannon, R. D. & Prewitt, C. T. Effective Ionic Radii in Oxides and Fluorides. *Acta Crystallographica B* **25**, 925–946 (1969).
21. Gardner, J. S., Gingras, M. J. P. & Greidan, J. E. Magnetic Pyrochlore Oxides. *Reviews of Modern Physics* **82** (2010).
22. Pivovarova, A. P. Compound  $Mg_2Ta_2O_7$  and its Interaction with  $Nd_3TaO_7$ . *Refractories and Industrial Ceramics* **43**, 172–175 (2002).
23. Trump, B. A. *et al.* Universal Geometric Frustation in Pyrochlores. *Nature Communications* **9** (2018).
24. Feuerbacher, M., Würtz, E., Kovács, A. & Thomas, C. Single-Crystal Growth of a FeCoCrMnAl High-Entropy Alloy. *Materials Research Letters* **5**, 128–134 (2017).
25. Musicó, B. L. *et al.* The Emergent Field of High Entropy Oxides: Design, Prospects, Challenges, and Opportunities for Tailoring Material Properties. *APL Materials* **8** (2020).
26. Yang, W. C. *et al.* Stoichiometry Control and Electronic and Transport Properties of Pyrochlore  $Bi_2Ir_2O_7$  Thin Films. *Physical Review Materials* **2** (2018).
27. Takikawa, Y., Ebisu, S. & Shoichi, N. Van Vleck Paramagnetism of the Trivalent Eu Ions. *Journal of Physics and Chemistry of Solids* **71**, 1592–1598 (2010).
28. Ashcroft, N. W. & Mermin, N. D. *Solid State Physics* (Saunders College Publishing, 1076).
29. Scheie, A. O. *et al.* Crystal Field Levels and Magnetic Anisotropy in the Kagome Compounds  $Nd_3Sb_3Mg_2O_{14}$ ,  $Nd_3Sb_3Zn_2O_{14}$ , and  $Pr_3Sb_3Mg_2O_{14}$ . *Physical Review B* **98** (2018).
30. Scheie, A. O. *et al.* Scalar Chiral Spin-1/2 Order on Kagome Lattices in  $Nd_3Sb_3Mg_2O_{14}$ . *Physical Review B* **93** (2016).
31. Ciomaga Hatnean, M. *et al.* Structural and Magnetic Investigations of Single-Crystals of the Neodymium Zirconate Pyrochlore,  $Nd_2Zr_2O_7$ . *Physical Review B* **91** (2015).
32. Swarnakar, D., Jana, Y., Alam, J. & Nandi, S. Chemical Pressure Effect in Magnetic Frustrated Pyrochlore  $Nd_2Pb_2O_7$ : A Crystal-Field Analysis. *Physica B: Condensed Matter* **521**, 93–97 (2017).

33. Winiarski, M. J. & Klimczuk, T. Crystal Structure and Low-Energy Einstein Mode in ErV<sub>2</sub>Al<sub>20</sub> Intermetallic Cage Compound. *Journal of Solid State Chemistry* **245**, 10–16 (2017).
34. Kelly, Z. A., Gallagher, M. J. & McQueen, T. M. Electron Doping a Kagome Spin Liquid. *Physical Review X* **6** (2016).
35. Morey, J. R., Scheie, A. O., Scheckton, J. P., Brown, C. M. & McQueen, T. M. Ni<sub>2</sub>Mo<sub>3</sub>O<sub>8</sub>: Complex Antiferromagnetic Order on a Honeycomb Lattice. *Physical Review Materials* **3** (2019).
36. Tari, A. *The Specific Heat of Matter at Low Temperatures* (Imperial College Press, 2003).
37. Melot, B. C. *et al.* Large Low-Temperature Specific Heat in Pyrochlore Bi<sub>2</sub>Ti<sub>2</sub>O<sub>7</sub>. *Physical Review B* **79** (2009).
38. Sinha, M. *et al.* Introduction of Spin Centers in Single Crystals of Ba<sub>2</sub>CaWO<sub>6- $\delta$</sub> . *Physical Review Materials* **3** (2019).

# Chapter 4

## Transition Metal (Dis)order in Single Crystal Multicomponent Rare Earth Perovskites

### Introduction

High entropy materials, multicomponent systems with a high configurational entropy term, i.e., a large positive  $\Delta S$  due to compositional disorder, have received an explosion of interest in the recent years due to the impact the disorder can have on the properties, an example seen in Ni super-alloys and coatings to protect from corrosion. [1–3] In the area of high entropy oxides (HEO), in particular systems with multiple components on the cation sublattice, there are intriguing questions regarding the presence of the local order/disorder in accordance with the single-phase structure present in these ceramics. [4–6] This naturally impacts the magnetic exchange interactions and gives rise to the question of whether there is complete disorder or does new behavior emerge distinct from the parents’ ala a “cocktail effect”. [7] The perovskite structure serves as an attractive target thanks to its flexibility to accommodate a wide range of cations in the lattice. [8] Bulk single crystals are essential in these studies to allow for more characterization tools in both crystal structure and magnetism. Currently bulk single crystal growth for high entropy/multi component materials has only been briefly explored. [9–11] We report the first synthesis of bulk single

crystals of HEO perovskite  $\text{SmCo}_{1/4}\text{Cr}_{1/4}\text{Fe}_{1/4}\text{Mn}_{1/4}\text{O}_3$  using a laser diode floating zone furnace. Single crystal X-ray diffraction data (SCXRD) shows the material crystallizes in a distorted orthorhombic perovskite structure in the space group Pnma. DC magnetization measurements show antiferromagnetic ordering with spin glassiness suggested according to differences in zero-field and field cooled measurements. Magnetization as a function of field shows temperature dependent hysteresis indicative of spin canting of the transition metals with ferrimagnetic interactions. Compared to the parent  $\text{SmMO}_3$  ( $M=\text{Co, Cr, Fe, Mn}$ ) perovskites, these transitions occur at different temperatures, with the HEO lacking the complete reversal in magnetization seen in  $\text{SmFeO}_3$  due to the ferrimagnetic behavior between the disordered transition metals. [12] The non-magnetic rare earth analogue of  $\text{LaCo}_{1/4}\text{Cr}_{1/4}\text{Fe}_{1/4}\text{Mn}_{1/4}\text{O}_3$  shows that Sm interaction with the transition metal sublattice increases as temperature decreases, with heat capacity measurements used to extract out the Sm magnetic contribution from the phonon behavior. Overall, this paper supports the use of the floating zone technique in synthesizing bulk single crystals of high entropy materials of interest and shows the impact disorder can have even for a “low entropy” HEO.

## Methods

### Synthesis

Starting rare earth oxides  $\text{La}_2\text{O}_3$  (Alfa Aesar 99.99% E12W028)  $\text{Sm}_2\text{O}_3$  (Alfa Aesar 99.99%, T24B047) were dried at  $T \sim 1000^\circ \text{ C}$  overnight. Rare earth oxides were weighed out along with  $\text{Co}_3\text{O}_4$  (NOAH Technologies 99.5% 100541),  $\text{CrO}_2$  (Dupont)  $\text{Fe}_3\text{O}_4$  (Cerac 99.5%, X8089), and  $\text{MnO}_2$  (NOAH Technologies 99.9% 211512) targeting the formula  $\text{LnCo}_{1/4}\text{Cr}_{1/4}\text{Fe}_{1/4}\text{Mn}_{1/4}\text{O}_3$  and mixed intimately in an agate mortar and pestle.  $\text{SmCo}_{1/4}\text{Cr}_{1/4}\text{Fe}_{1/4}\text{Mn}_{1/4}\text{O}_3$  were heated as loose powder in an uncovered alumina boat in a horizontal tube furnace at  $T \sim 1450^\circ \text{ C}$  for 12 hours with a ramp rate of  $100^\circ \text{ C/hr}$  and allowed to cool to room temperature over 12 hours.

$\text{LaCo}_{1/4}\text{Cr}_{1/4}\text{Fe}_{1/4}\text{Mn}_{1/4}\text{O}_3$  powder were heated similarly to dwell at  $T \sim 1350^\circ \text{ C}$ .

$\text{SmCo}_{1/4}\text{Cr}_{1/4}\text{Fe}_{1/4}\text{Mn}_{1/4}\text{O}_3$  were compacted into rod shapes using rubber balloons, evacuated, and subsequently subjected to hydro-static pressure ( $\sim 75 \text{ MPa}$ ). Upon removal from the balloon, the rods were sintered in an open alumina boat in a box furnace at  $T \sim 1450^\circ \text{ C}$  for 12 hours with a ramp rate of  $100^\circ \text{ C/hr}$  and allowed to cool to room temperature over 12 hours. The sintered rods were mounted in a Laser Diode Floating Zone (LDFZ) furnace (Crystal Systems, Inc., FD-FZ-5-200-VPO-PC) with  $5 \times 200 \text{ W}$  GaAs lasers ( $\lambda = 976 \text{ nm}$ ); the seed rod was affixed to an alumina holder on the lower shaft using Nichrome wire while the feed rod was suspended from a hook on the upper shaft using Nichrome wire. An applied pressure of 2 bar of  $\text{O}_{2(\text{g})}$  was used flowing at  $250 \text{ mL/min}$  with lasers tilted at  $5^\circ$  above the plane. The seed rod was melted, and the feed rod was joined to create a stable molten zone. Both rods were translated downward through the hot zone. The steady state conditions were found to occur when the upper and lower shaft traveled at a rate of 5.5 and 5 mm/hr respectively while counter rotating at 10 rpm.

## Characterization

Heat capacity measurements from  $T=2\text{-}300 \text{ K}$  were taken with a Quantum Design Physical Properties Measurement System (PPMS) using the semi adiabatic pulse method with a 1% temperature rise. Phonon subtraction of heat capacity using the La containing analog was performed by scaling according to Hofmann and extrapolating to  $T=0 \text{ K}$ . [13, 14] Magnetization data were collected as a function of temperature and field from  $T=2\text{-}300 \text{ K}$  and  $\mu_0 H=-7$  to  $7 \text{ T}$  on both powder and aligned crystals using a Quantum Design Magnetic Property Measurement System (MPMS). Energy dispersive X-ray spectroscopy (EDS) to estimate transition metal ratios was performed using a JEOL JSM IT100 scanning electron microscope (SEM) at 20 keV operating in backscatter mode.

Laboratory-based X-ray diffraction patterns of the powder and ground up single crystals were collected using a Bruker D8 Focus diffractometer with Cu  $K_{\alpha}$  radiation and a LynxEye position sensitive detector. Rietveld refinements to check phase purity were performed using Bruker TOPAS software (Version 4.2, Bruker AXS). For the SCXRD analysis, all reflection intensities were measured at 213(2) K using a Rigaku Oxford Diffraction SuperNova diffractometer (equipped with Atlas detector) with Mo  $K_{\alpha}$  radiation ( $\lambda=0.71073$  Å) under the program CrysAlisPro (Version CrysAlisPro 1.171.42.49, Rigaku OD, 2022). The same program was used to refine the cell dimensions and for data reduction. The structure was solved with the program SHELXS-2018/3 and was refined on  $F^2$  with SHELXL-2018/3. [15] Data were corrected for absorption using an analytical numeric absorption correction using a multifaceted crystal model under CrysAlisPro. The temperature of the data collection was controlled using the system Cryojet (manufactured by Oxford Instruments). The occupancies of the 3d transition metals were fixed at 0.25 according to input stoichiometries and absence of impurity phase in PXRD. Crystal structure were visualized using VESTA. [16] Point charge calculations for Sm<sup>3+</sup> were performed using PyCrystalField. [17]

## Results and Discussion

In the discussion of HEO, there is a distinction of entropy stabilized vs high entropy that should be noted. [18, 19] The family of HEO  $LnMO_3$  are shown to be phase pure when cooled slowly, so the configurational entropy is not decisive to the stability of the phase, compared to other systems such as the HEO rock salt  $Co_{0.2}Cu_{0.2}Mg_{0.2}Ni_{0.2}Zn_{0.2}O$ . [20] Commonly in designing HE materials, a 5-component equimolar substitution is instituted on the sublattice and has been done for previously synthesized HEO perovskites. [21] Initial attempts to synthesize the 5-component  $Sm(Co_{0.2}Cr_{0.2}Fe_{0.2}Mn_{0.2}Ni_{0.2})O_3$  were successful for powder form but crystal growth using the floating zone method resulted in an impurity of NiO in PXRD of the grown

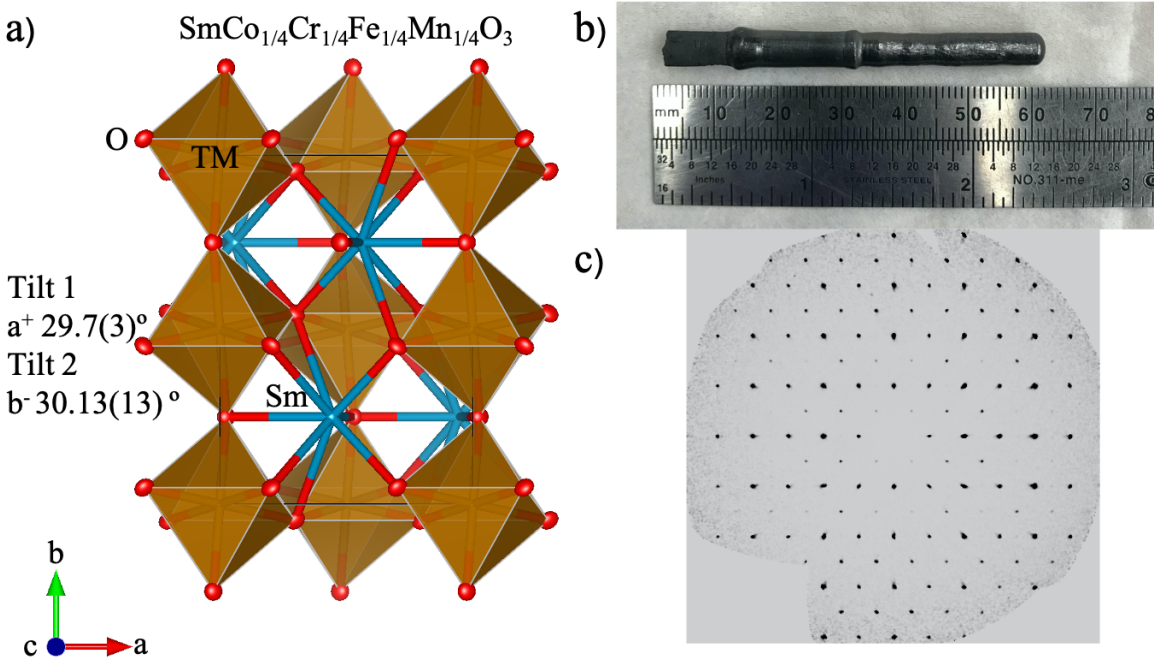


**Figure 4-1.** a) Crystal structure of  $\text{SmCo}_{1/4}\text{Cr}_{1/4}\text{Fe}_{1/4}\text{Mn}_{1/4}\text{O}_3$  with Glazer notation  $a^+b^-b^-$  for the tilted transition metal octahedra. Atomic displacement parameters are visualized at 80% probability b) Floating zone grown crystal of  $\text{SmCo}_{1/4}\text{Cr}_{1/4}\text{Fe}_{1/4}\text{Mn}_{1/4}\text{O}_3$  c) Digitally reconstructed precession photograph from SCXRD data along the  $(0kl)$  plane

crystal. This is due to  $\text{Ni}^{3+}$  requiring high oxidizing conditions for crystal growth, as seen in the rare earth nickelates. [22, 23] Given the multiple valence states optional for many of these transition metals, it is likely that each element is in the 3+ state based on this experiment, further supported by the calculated bond valence sums approximating 3. [24]

Much discussion has been had concerning label of “high entropy” for materials and its impact. [25] For this material for example, the configurational entropy per formula unit is  $1.39R$ , where  $R$  is the molar gas constant. This traditionally places it in the category of medium entropy. If one accounts for the other sublattices and calculate this per atom, the categorization drops to  $0.28R$ , firmly in low entropy. If one uses an entropy metric to account for different sublattices, the calculated value is 0.84, keeping it under the classification of low entropy. [26] In the case of HEO

Formula	SmCo <sub>1/4</sub> Cr <sub>1/4</sub> Fe <sub>1/4</sub> Mn <sub>1/4</sub> O <sub>3</sub>					
Crystal System	Orthorhombic					
Space Group	Pnma (no. 99)					
<i>a</i> (Å)	5.5568(2)					
<i>b</i> (Å)	7.6367(3)					
<i>c</i> (Å)	5.3679(2)					
<i>V</i> (Å <sup>3</sup> )	227.790(15)					
<i>Z</i>	1					
Radiation	Mo <i>K</i> <sub>α</sub> , $\lambda=0.71073$ Å					
Temperature (K)	213					
Absorption Coefficient (mm <sup>-1</sup> )	31.21					
F(0 0 0)	446					
Reflections collected/unique/internal data agreement	6196/459, <i>R</i> <sub>int</sub> =0.048					
Data/parameters	459/29					
Goodness-of-fit	1.18					
<i>R</i> = $\sum   F_o  -  F_c   / \sum  F_o $	0.017					
<i>wR</i> (F <sup>2</sup> ) = [ $\sum w(F_o^2 - F_c^2)^2 / \sum w(F_o^2)^2$ ] <sup>1/2</sup>	0.040					
Largest dif. peak/hole	1.660/-1.921 e Å <sup>-3</sup>					
	Occ.	Wyckoff Positions	x (Å)	y (Å)	z (Å)	U <sub>iso</sub> (Å <sup>2</sup> )
Co	1/4	4a	0.5	0	0.5	0.00380(14)
Cr	1/4	4a	0.5	0	0.5	0.00380(14)
Fe	1/4	4a	0.5	0	0.5	0.00380(14)
Mn	1/4	4a	0.5	0	0.5	0.00380(14)
Sm	1	4c	0.94341(4)	0.25	0.48773(4)	0.00560(10)
O1	1	4c	0.4746(6)	-0.25	0.4096(7)	0.0081(6)
O2	1	8d	0.7018(4)	0.0470(3)	0.2008(4)	0.0084(4)
	U <sub>11</sub> (Å <sup>2</sup> )	U <sub>22</sub> (Å <sup>2</sup> )	U <sub>33</sub> (Å <sup>2</sup> )	U <sub>12</sub> (Å <sup>2</sup> )	U <sub>13</sub> (Å <sup>2</sup> )	U <sub>23</sub> (Å <sup>2</sup> )
Co=Cr=Fe=Mn	0.0039(3)	0.0040(3)	0.0036(3)	-0.0003(2)	0.00007(19)	-0.00008(19)
Sm	0.00531(14)	0.00585(14)	0.00565(15)	0	0.00077(7)	0
O1	0.0086(15)	0.0095(14)	0.0062(15)	0	0.0019(12)	0
O2	0.0100(11)	0.0086(9)	0.0065(10)	0.0019(8)	-0.0015(9)	0.0014(8)

**Table 4-I.** Crystallographic parameters of the SXRD for floating zone grown SmCo<sub>1/4</sub>Cr<sub>1/4</sub>Fe<sub>1/4</sub>Mn<sub>1/4</sub>O<sub>3</sub>

*LnMO<sub>3</sub>*, we see that the configurational entropy likely isn't the leading contribution to its behavior but instead the chemically complex exchange interactions occurring. Due to familiarity, we will keep the using the term HEO to emphasize the design concept rather than the inherent classification.

Single crystal structure solution of HEO SmMO<sub>3</sub> shows the material crystallizes in space group Pnma with the structure type GdFeO<sub>3</sub>, with the resulting parameters shown in Table 4-I. This is a distorted orthorhombic perovskite as visualized in Figure 4-1a with Glazer notation *a*<sup>+</sup>*b*<sup>-</sup>*b*<sup>-</sup>. [27] The as-grown crystal is visualized in Figure 4-1b. Due to the high fluorescence of the transition metals, analysis of the crystallinity by use of Laue diffraction was not feasible. Precession images were digitally reconstructed from raw SCXRD data and show no sign of twinning or streaking as shown in Figure

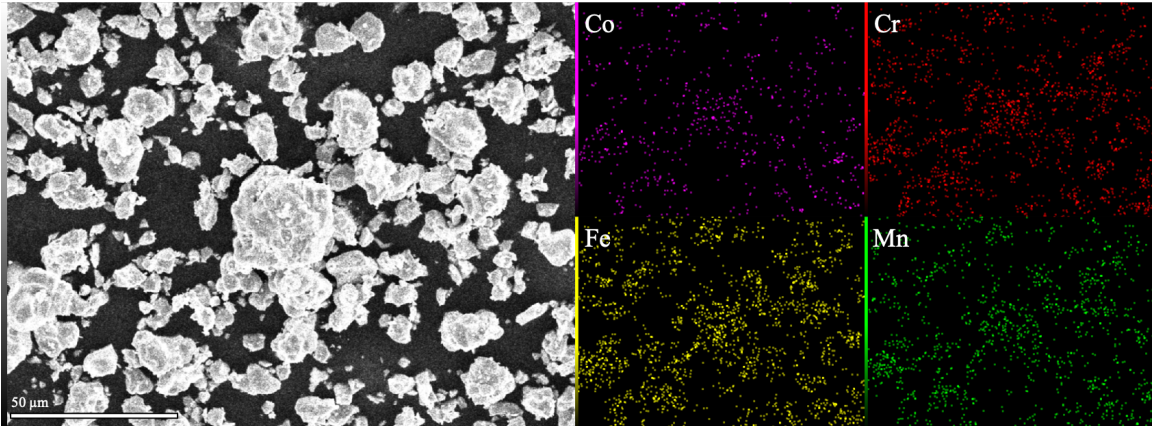


**Figure 4-2.** SEM image of  $\text{SmCo}_{1/4}\text{Cr}_{1/4}\text{Fe}_{1/4}\text{Mn}_{1/4}\text{O}_3$  powder with EDS mapping of the transition metal elements colored.

Element	Atom %
Co	6.09(21)
Cr	3.92(17)
Fe	4.70(23)
Mn	6.32(22)

**Table 4-II.** Elemental ratios for single crystal  $\text{SmCo}_{1/4}\text{Cr}_{1/4}\text{Fe}_{1/4}\text{Mn}_{1/4}\text{O}_3$  as determined by EDS

4-1c along the  $(0kl)$  plane. Powder samples of both HEO  $\text{SmMO}_3$  and  $\text{LaMO}_3$  as well as the ground up crystal are seen as phase pure in powder X-ray diffraction (PXRD). Due to the multicomponent substitution, occupancy was checked using EDS, results shown in Table 4-II, although the real error bars are likely larger due to the closeness in peak location. Mapping of the powder in Figure 4-2 shows homogeneous distribution, evidence of a single-phase perovskite.

Magnetization as a function of temperature in Figure 4-3a shows a bifurcation occurring between the field cooled (FC) and zero field cooled (ZFC) at  $T \sim 150$  K for powder samples of  $\text{SmMO}_3$ . Two transitions, independent of cooling method, are seen to occur below room temperature, one around the bifurcation, the second being a broad hump with its maxima centered around  $T \sim 12.5$  K. Application of increasing field (up to  $\mu_0 H = 7$  T) is shown in Figure 3b to suppress this second transition. Measurements with field both parallel and perpendicular to single crystal in Figure 3c and d show

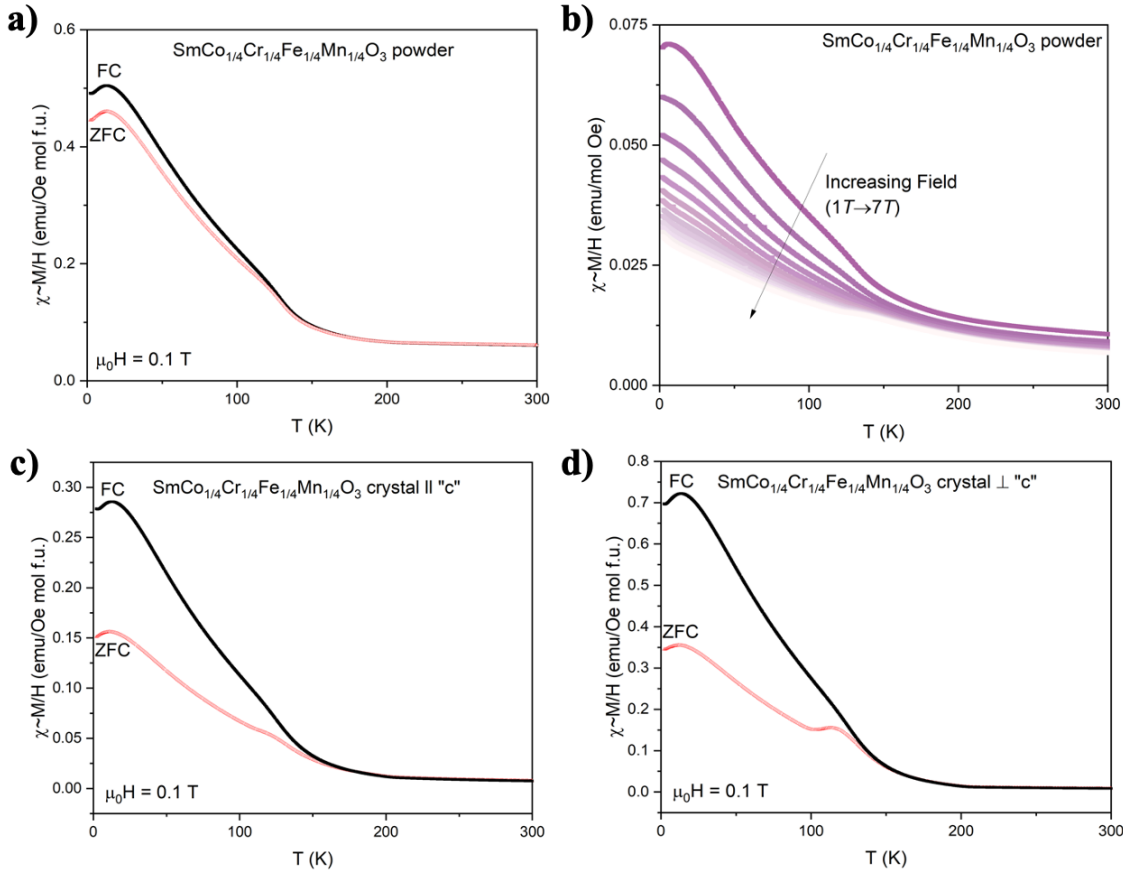


**Figure 4-3.** Field cooled (FZ) and zero field cooled (ZFC) magnetization as a function of temperature for a)  $\text{SmCo}_{1/4}\text{Cr}_{1/4}\text{Fe}_{1/4}\text{Mn}_{1/4}\text{O}_3$  powder, b)  $\text{SmCo}_{1/4}\text{Cr}_{1/4}\text{Fe}_{1/4}\text{Mn}_{1/4}\text{O}_3$  powder under multiple fields, c)  $\text{SmCo}_{1/4}\text{Cr}_{1/4}\text{Fe}_{1/4}\text{Mn}_{1/4}\text{O}_3$  parallel to crystal length, and d)  $\text{SmCo}_{1/4}\text{Cr}_{1/4}\text{Fe}_{1/4}\text{Mn}_{1/4}\text{O}_3$  perpendicular to crystal length

presence of anisotropy, with divergence occurring around  $T \sim 200 \text{ K}$ . Both magnetic transitions are still visible, with both perpendicular transitions now manifesting as broad humps under ZFC. Further, the bifurcation of ZFC and FC occurs at higher temperatures for both directions compared to the powder. A comparison with the non-magnetic rare earth analog  $\text{LaMO}_3$  shows similar behavior at high temperatures among ZFC and FC measurements, shown in Figure 4-4. Measurement below the bifurcation shows the downturn occurring at higher temperatures than the Sm as well over a larger temperature range.

Attempts to fit the upper magnetic region to the Curie Weiss law for the Sm

variant requires the use of a Van Vleck contribution. [28] The data can be fit as:

$$\chi^{-1} = \frac{T - \Theta_{CW}}{\chi_0 * (T - \Theta_{CW}) + C} \quad (4.1)$$

Attempting such a fit still results in no linear portion of the inverse susceptibility, excluding the meaningfulness of any extracted constants from the Curie-Weiss analysis. Fitting of the La analog gives  $C=1.645(1)$ , assuming 1 total magnetic ion per formula unit. As transition metal compounds can experience spin transition between low and high spin states as temperature crosses the spin gap energy, one must consider different situations depending on the crystal field splitting. [29–31] If all high spin,  $C=3.06$ , low spin (i.e.  $\text{Co}^{3+}$  is  $S = 0$ ),  $C=0.813$ , both out of range of our extracted value. A more likely intermediate spin state ( $S_{\text{Co}} = 0, S_{\text{Cr}} = 3/2, S_{\text{Fe}} = 5/2, S_{\text{Mn}} = 1$ ) gives  $C=1.81$ , close to our value. We see from this that even in complex disordered systems that CW analysis if applied carefully can serve to help understand the likely spin configuration, with further experiments such as X-ray magnetic circular dichroism (XMCD) available to investigate the systems magnetic behavior.

Measurements of magnetization as a function of field in Figure 4-5a show no saturation in magnetic moment up to 7 T, with hysteresis emerging and closing between the two magnetic transitions. This ferromagnetic behavior is likely to arise from spin canting in the transition metal sublattice, as discussed further below. Further the hysteresis is often not centered around the origin, and changes position with temperature. The exchange bias and coercive field are defined as:

$$H_{EB} = \frac{H_1 + H_2}{2} \quad (4.2)$$

Plotting this as a function of temperature is shown in Figure 4-5b. Two items of interest are seen in this plot. One, the coercive field does not decrease with increasing temperature but instead goes through two peaks near the magnetic transitions. Second, this behavior is also supported by the variation in exchange bias, indicating

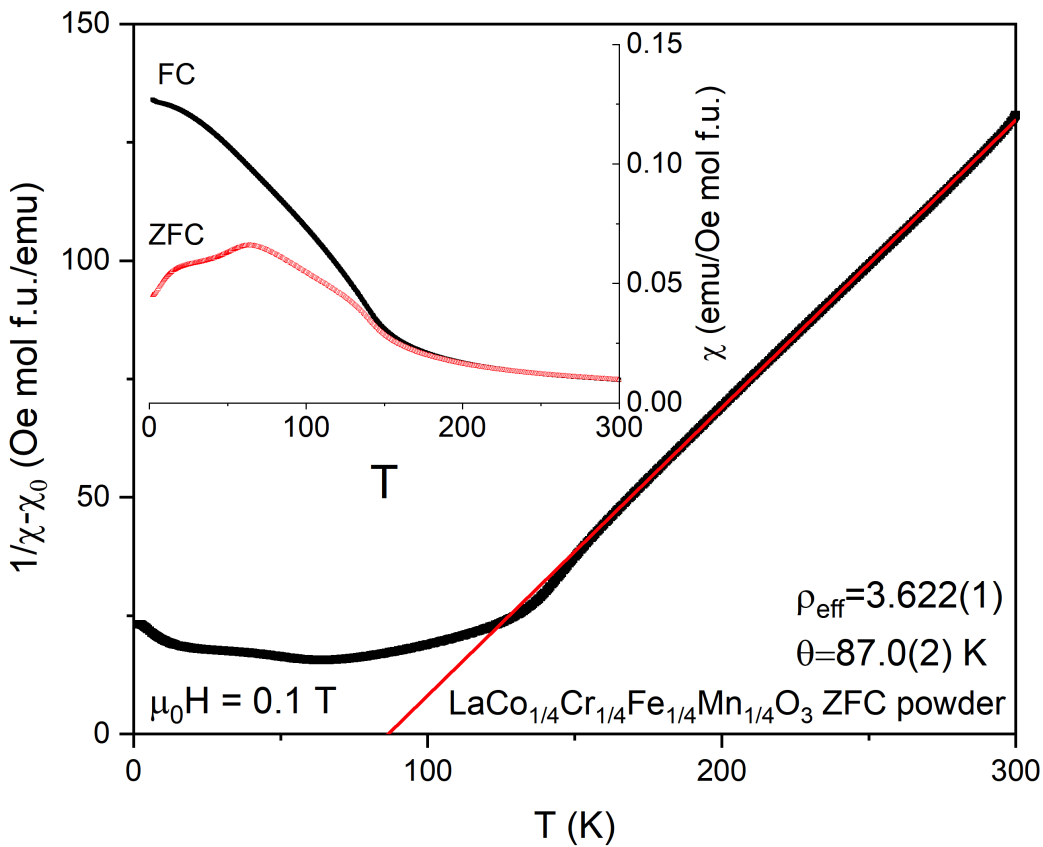


**Figure 4-4.** Curie Weiss fit to the paramagnetic region of zero field cooled (ZFC)  $\text{LaCo}_{1/4}\text{Cr}_{1/4}\text{Fe}_{1/4}\text{Mn}_{1/4}\text{O}_3$  powder. Inset shows the field cooled (FC) and zero field cooled (ZFC) magnetization as a function of temperature

interactions between the two magnetic sublattices at different energy scales. The ability to have a tunable exchange bias with varying disorder and temperature is highly desired for spintronic applications and has been demonstrated for systems exhibiting antiferromagnetic and spin glass coupling. [32, 33] Current research has explored this in other high entropy perovskites due to the high degree of disorder, with such systems also investigated for their magnetocaloric behavior. [34–36]

To better understand the nature of this system's magnetic behavior, it is best put in context of the parent compounds it's derived from. Such behavior is summarized in Table 4-III.  $\text{SmFeO}_3$  for example, orders antiferromagnetically below  $T=680$  K, with weak ferrimagnetism present from the canted spins of the Fe sublattice.[12]

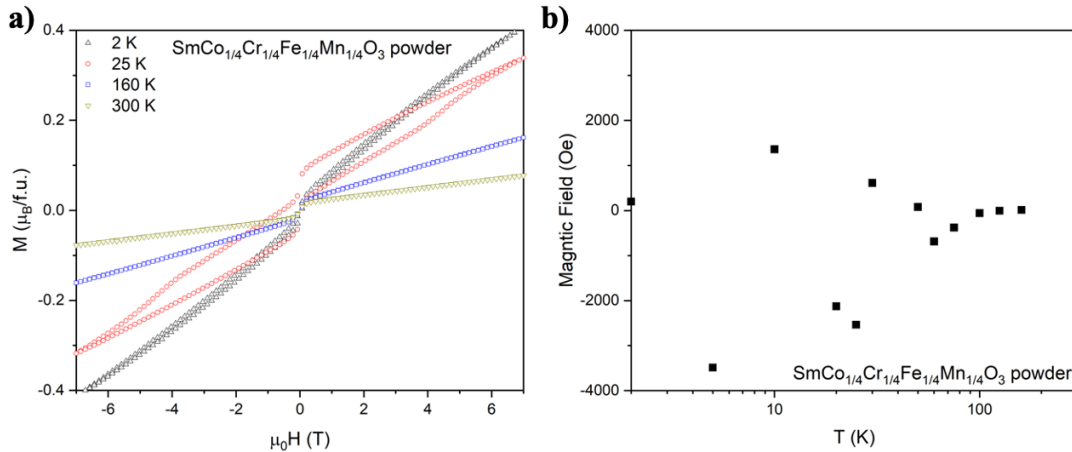


**Figure 4-5.** a) Magnetization as a function of field for  $\text{SmCo}_{1/4}\text{Cr}_{1/4}\text{Fe}_{1/4}\text{Mn}_{1/4}\text{O}_3$  powder over multiple temperatures. b) A plot of the exchange bias ( $H_{EB} = [H_1 + H_2]/2$ ) for  $\text{SmCo}_{1/4}\text{Cr}_{1/4}\text{Fe}_{1/4}\text{Mn}_{1/4}\text{O}_3$  powder over multiple temperatures.

	$T_N$	$T_{SR2}$	$T_{SR1}$	$T_{SSW}$	$T_{Comp}$
$\text{SmCoO}_3$ [37]	-	-	-	-	-
$\text{SmCrO}_3$ [38]	191 K	34 K	-	-	-
$\text{SmFeO}_3$ [12]	680 K	480 K	450 K	278.5 K	3.9 K
$\text{SmMnO}_3$ [39]	60 K	-	-	-	9 K

**Table 4-III.** Summary of magnetic behavior of parent compounds of HEO  $\text{SmMO}_3$ , where  $T_N$ ,  $T_{SR2}$ ,  $T_{SR1}$ ,  $T_{SSW}$ , and  $T_{Comp}$  are the Neel temperature, spin reorientation temperatures 1 and 2, spin switching transition, and compensation temperature respectively.

As the system is cooled further, a spin switching transition occurs, whereupon it later reaches a compensation temperature by the increased magnitude of the FM Sm moment opposite of the Fe moment. Similarly, for  $\text{SmCrO}_3$  and  $\text{SmMnO}_3$ , there exists a canted antiferromagnetic ordering along with a spin reorientation of the Cr lattice and a compensation temperature of the Mn and Sm moments, while  $\text{SmCoO}_3$  exhibits paramagnetic behavior. [37–39] From these we can see that the first broad transition in HEO  $\text{SmMO}_3$  is likely the AFM ordering of the TM sublattice, with the second broad transition involving the orientation of the Sm sublattice, supported by the weaker magnetic behavior for the La analog at low temperature. We see that the “high entropy” effect has altered the transition temperatures for this material compared to the parent as well as removed this large reversal in magnetization seen

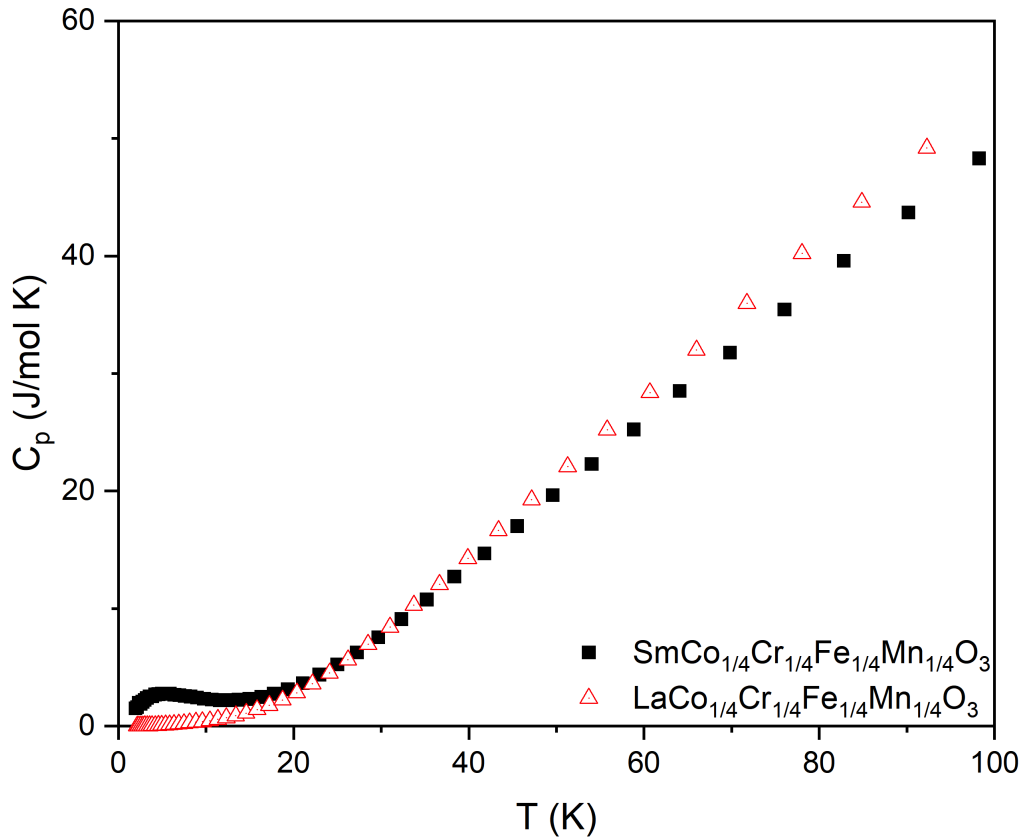


**Figure 4-6.** Heat capacity as a function of temperature for single crystal  $\text{SmCo}_{1/4}\text{Cr}_{1/4}\text{Fe}_{1/4}\text{Mn}_{1/4}\text{O}_3$  and  $\text{LaCo}_{1/4}\text{Cr}_{1/4}\text{Fe}_{1/4}\text{Mn}_{1/4}\text{O}_3$  powder.

for Fe, Mn, Cr.

Heat capacity data, specifically  $C_p/T$ , give no sign of magnetic ordering in the presence of sharp anomalies. A broad hump is seen in  $C_p$  as a function of temperature for Figure 4-6 occurring below both ordering transitions and could be a Schottky contribution. Comparison between the La analog shows  $C_{mag}$  being most evident below  $T \sim 20$  K. After appropriate scaling is applied, subtraction of the  $C_{lat}$  can be done using the La analog, upon which magnetic entropy can be obtained following 2.8. The entropy saturates at approximately 7.5 J/mol K, exceeding  $R\ln(2)$  by 30% as shown in Figure 4-7a. Point charge calculation performing using PyCrystalField shown in Figure 4-7b gives an effective  $S = 1/2$  ground state. The entropy offset

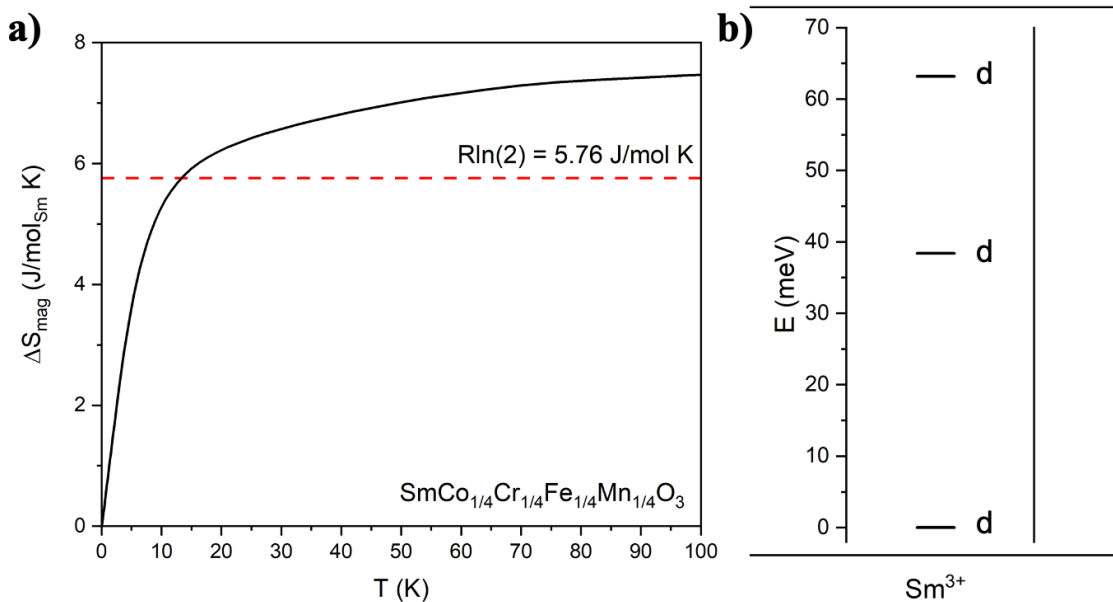


**Figure 4-7.** The magnetic entropy for  $\text{SmCo}_{1/4}\text{Cr}_{1/4}\text{Fe}_{1/4}\text{Mn}_{1/4}\text{O}_3$  obtained by integrated  $C_{\text{mag}}/T$  data after subtracting the scaled La analog. b) The computed single ion crystal field for Sm<sup>3+</sup> in the perovskite structure. Doublet states are indicated by d.

is unexpected but given the potential difference in stoichiometry between the two analogs, as well as difference in local environment and contributions of the transition metal spins. More work should be pursued to understand proper use of effective analogs for high entropy systems.

## Conclusion

Overall, the usefulness of single crystals in the design process of high entropy oxides for magnetic applications is demonstrated. We see the presence of single ion anisotropy in the Sm-containing multicomponent transition metal perovskite with magnetic behavior distinct from its parents. The field dependent behavior is of particular interest due to the variability at different temperature regimes for magnetocaloric behavior and tunable exchange bias. Nonmagnetic analogs are utilized to get a better understanding of the compared behavior, in heat capacity measurements specifically.

Further directions should utilize this development in single crystal growth to undergo further measurements such as single crystal pair distribution function to understand the development of short-range order combined with XMCD to get transition element resolved information on the magnetic transitions and spin canting.

## Acknowledgements

This work was funded by the Platform for the Accelerated Realization, Analysis, and Discovery of Interface Materials (PARADIM), a National Science Foundation Materials Innovation Platform (NSF DMR-2039380). The MPMS was funded by the National Science Foundation, Division of Materials Research, Major Research Instrumentation Program, under Award 1828490. Raw data from the facility related to these syntheses is available after publication at <https://data.paradim.org/XXXX>

# References

1. Cantor, B., Chang, I. T. H., Knight, P. & Vincent, A. J. B. Microstructural development in equiatomic multicomponent alloys. *Materials Science and Engineering: A* **375-377**, 213–218 (2004).
2. Yeh, J.-W. *et al.* Nanostructured High-Entropy Alloys with Multiple Principle Elements: Novel Alloy Design Concepts and Outcomes. *Advanced Engineering Materials* **6**, 299–303 (2004).
3. Gao, M. C., Yeh, J.-W., Liaw, P. K. & Yong, Z. *High-Entropy Alloys: Fundamentals and Applications* 1st (Cham: Springer International Publishing, 2016).
4. Musicó, B. L. *et al.* The Emergent Field of High Entropy Oxides: Design, Prospects, Challenges, and Opportunities for Tailoring Material Properties. *APL Materials* **8** (2020).
5. Jiang, B. *et al.* Probing the Local Site Disorder and Distortion in Pyrochlore High-Entropy Oxides. *Journal of American Chemical Society* **143**, 4193–4204 (2021).
6. Dabrowa, J. *et al.* Synthesis and Microstructure of the  $(\text{Co,Cr,Fe,Mn,Ni})_3\text{O}_4$  High Entropy Oxide Characterized by Spinel Structure. *Materials Letters* **216**, 32–26 (2018).
7. Sarkar, A., Kruk, R. & Hahn, H. Magnetic Properties of High Entropy Oxides. *Dalton Transactions* **50**, 1973–1982 (2021).
8. Goldschmidt, V. M. Die Gesetze der Krystallochemie. *Naturwissenschaften* **14**, 477–485 (1926).
9. Kinsler-Fedon, C. *et al.* Synthesis, Characterization, and Single-Crystal Growth of a High-Entropy Rare-Earth Pyrochlore Oxide. *Physical Review Materials* **4**, 104411 (2020).
10. Pianassola, M. *et al.* Crystal Growth and Elemental Homogeneity of the Multicomponent Rare-Earth Garnet  $(\text{Lu}_{1/6}\text{Y}_{1/6}\text{Ho}_{1/6}\text{Dy}_{1/6}\text{Tb}_{1/6}\text{Gd}_{1/6})_3\text{Al}_5\text{O}_{12}$ . *Crystal Growth and Design* **20**, 6769–6776 (2020).
11. Feuerbacher, M., Würtz, E., Kovács, A. & Thomas, C. Single-Crystal Growth of a FeCoCrMnAl High-Entropy Alloy. *Materials Research Letters* **5**, 128–134 (2017).
12. Cao, S., Zhao, H., Kang, B., Zhang, J. & Ren, W. Temperature Induced Spin Switching in  $\text{SmFeO}_3$  Single Crystal. *Scientific Reports* **4** (2014).
13. Hofmann, J. A., Paskin, A., Tauer, K. J. & Weiss, R. J. Analysis of ferromagnetic and antiferromagnetic second-order transitions. *Journal of Physics and Chemistry of Solids* **1**, 45–60 (1956).

14. Tari, A. *The Specific Heat of Matter at Low Temperatures* (Imperial College Press, 2003).
15. Sheldrick, G. M. SHELXT-Integrated space-group and crystal-structure determination. *Acta Crystallographica A* **71**, 3–8 (2015).
16. Momma, K. & Izumi, F. VESTA: a three-dimensional visualization system for electronic and structural analysis. *Journal of Applied Crystallography* **41**, 654–658 (2008).
17. Scheie, A. PyCrystalField: software for calculation, analysis and fitting of crystal electric field Hamiltonians. *Journal of Applied Crystallography* **54**, 356–362 (2021).
18. Navrotsky, A. & Kleppa, O. J. Thermodynamics of Formation of Simple Spinels. *Journal of Inorganic Nuclear Chemistry* **30**, 479–498 (1968).
19. Alexandra, N. Thermodynamics of Formation of Some Compounds with the Pseudo-brookite Structure and of the  $\text{FeTi}_2\text{O}_5$ - $\text{Ti}_3\text{O}_5$  Solid Solution Series. *American Mineralogist* **60**, 249–256 (1975).
20. Rost, C. M. *et al.* Entropy-Stabilized Oxides. *Nature Communications* **6** (2015).
21. Witte, R. *et al.* High-Entropy Oxides: An Emerging Prospect for Magnetic Rare-Earth Transition Metal Perovskites. *Physical Review Materials* **3**, 034406 (2019).
22. Zhang, J. High-Pressure Floating-Zone Growth of Perovskite Nickelate  $\text{LaNiO}_3$  Single Crystals. *Crystal Growth and Design* **17**, 2730–2735 (2017).
23. Zheng, H. *et al.* High  $p_{\text{O}_2}$  Floating Zone Crystal Growth of the Perovskite Nickelate  $\text{PrNiO}_3$ . *Crystals* **9**, 324 (2019).
24. Brown, I. D. Recent Developments in the Methods and Applications of the Bond Valence Model. *Chemical Reviews* **109**. PMID: 19728716, 6858–6919. eprint: <https://doi.org/10.1021/cr900053k> (2009).
25. Schneider, J. M. How High is the Entropy in High Entropy Ceramics? *Journal of Applied Physics* **130** (2021).
26. Dippo, O. F. & Vecchio, K. S. A Universal Configurational Entropy Metric for High-Entropy Materials. *Scripta Materialia* **201** (2021).
27. Glazer, A. M. The classification of tilted octahedra in perovskites. *Acta Crystallographica Section B* **B28**, 3384–3392 (1972).
28. Takikawa, Y., Ebisu, S. & Shoichi, N. Van Vleck Paramagnetism of the Trivalent Eu Ions. *Journal of Physics and Chemistry of Solids* **71**, 1592–1598 (2010).
29. Ovchinnikov, S. G., Orlov, Y. S., Nekrasov, I. A. & Pchelkina, Z. V. Electronic structure, magnetic properties, and mechanism of the insulator metal transition in  $\text{LaCoO}_3$  taking into account strong electron correlations. *Journal of Experimental and Theoretical Physics* **112**, 140–151 (2011).
30. Tanabe, Y. & Sugano, S. On the Absorption Spectra of Complex Ions II. *Journal of the Physical Society of Japan* **9**, 753–766 (1954).
31. Goodenough, J. B. & Raccah, P. M. Complex vs band formation in perovskite oxides. *Journal of Applied Physics* **36** (1965).
32. Maniv, E. *et al.* Exchange bias due to coupling between coexisting antiferromagnetic and spin-glass orders. *Nature Physics* **17**, 525–530 (2021).

33. Ali, M. *et al.* Exchange bias using a spin glass. *Nature Materials* **6**, 70–75 (2007).
34. Meisenheimer, P. B. & Heron, J. T. Oxides and the high entropy regime:a new mix for engineering physical properties. *MRS Advances* **5**, 3419–3436 (2020).
35. Mazza, A. R. *et al.* Designing Magnetism in High Entropy Oxides. *Advanced Science* **9**, 2200391 (2022).
36. Yin, Y. *et al.* Spin-glass behavior and magnetocaloric properties of high-entropy perovskite oxide. *Applied Physics Letters* **120** (2022).
37. Dudnikov, V. A. *et al.* Effect of Multiplicity Fluctuation in Cobalt Ions on Crystal Structure, Magnetic and Electrical Properties of NdCoO<sub>3</sub> and SmCoO<sub>3</sub>. *Molecules* **25**, 1301 (2020).
38. Tripathi, M., Choudhary, R. J., Phase, D. M., Chatterji, T. & Fischer, H. E. Evolution of Magnetic Phases in SmCrO<sub>3</sub>: A Neutron Diffraction and Magnetometric Study. *Phys. Rev. B* **96**, 174421 (2017).
39. Cheng, J.-G. *et al.* Exchange Field on the Rare Earth Sm<sup>3+</sup> in a Single Crystal Perovskite SmMnO<sub>3</sub>. *Physical Review B* **84**, 104415 (2011).

# Chapter 5

## Informing Quantum Materials Discovery and Synthesis using X-ray Micro-Computed Tomography

### Introduction

Materials behavior is critically impacted by extended structure complexity on the micron/nanometer scale. [1–3] These hierarchical structures can hinder or enhance the desired properties, especially for quantum materials where a balance of energy scales makes the ground states particularly sensitive. While more focus is directed on the atomic scale and periodicities, bulk features (on the scale of  $>1\text{ }\mu\text{m}$ ) can also mask the intrinsic behavior of a sample. To avoid these is impossible according to the third law of thermodynamics, but, to even controllably tune these intricacies is difficult depending on the synthesis conditions, as seen in materials such as metal alloys, crystal scintillators, and thermoelectrics. [4–7] This can be troublesome in particular for quantum materials, where inclusions, low angle grain boundaries, crystal twinning, and other structural imperfections can impact the physical properties of a material, such as in the superconductors  $\text{YBa}_2\text{Cu}_3\text{O}_{7-\delta}$  (impacting the critical current density) and  $\text{Sr}_2\text{RuO}_4$  (impacting the  $T_c$ ). [8–12]

Many characterization techniques commonly used probe too small-scales, focus solely on the surface, and/or require destruction of the sample to visualize and quantify such features. [13–15] X-ray micro-computed tomography ( $\mu$ CT) is a non-destructive alternative technique that allows one to obtain a 3D representation of the sample with resolution in the  $\mu\text{m}$  to nm range. This method uses high energy x-rays to transmit through the sample, collecting multiple images that are then reconstructed into a 3D object where extended structural features can be visualized through a variety of contrast methods. [16] Since its conception,  $\mu$ CT has been integrated as a routine characterization tool for a variety of fields, including medicine, biology, and geology. [17–19] While this method of characterization is used extensively in materials science, for the condensed-matter community it has only recently been adopted in the analysis of electronic and quantum materials. [20–23] Throughout this paper, we demonstrate examples in which  $\mu$ CT can be an important characterization tool to aid in materials design and show insights that would not be possible without this technique.

## Experimental Methods

### Synthesis

Crystals of  $\text{SmB}_6$  were grown following a similar procedure of Phelan et al. [21] Crystals of r- $\text{GeO}_2$  were grown following a similar procedure of Niedermeier et al. [24] Initial powder and floating zone rods of  $\text{YbMgGaO}_4$  were prepared following a similar procedure to Li et al. [25] Crystals were grown using the 300 bar high pressure floating zone furnace (SciDre GmbH) at the Platform for the Accelerated Realization, Analysis and Discovery of Interface Materials (PARADIM) user facility at Johns Hopkins University. A 5 kW Xenon arc lamp was utilized as a heating source at pressure of 20 bar with an oxygen flow rate of 0.1 L/min. Feed and seed rods were rotated together at 20 rpm. The feed rod and the seed rod were advanced at rates of 10 to 12 mm/h and 10 mm/h respectively. Crystals of r- $\text{TiO}_2$  were grown following

the procedure of Wright et al. [26] with no sample rotation applied for either the seed or feed rod.

## Characterization

Standard  $\mu$ CT data were collected using a Bruker SkyScan 1172 with an operating range of 20-100 kV for the x-ray source and 0.9  $\mu$ m maximum pixel resolution using an Al+Cu filter. Specifically, the point-spread function for each measurement is listed in Table 5-I following the procedure of Ketcham et al. [27] Reconstructions were done using NRecon with ring artifact removal and beam hardening correction algorithms applied. The reconstructed data were visualized and analyzed using Dragonfly software, Version 2021.1 for Windows (Object Research Systems (ORS) Inc, Montreal, Canada, 2020; software available at <http://www.theobjects.com/dragonfly>). Measurements used for the 3D rose diagrams were generated using Quant3D (<https://www.ctlab.geo.utexas.edu/software/quant3d/>). [28] Diffraction computed tomography data were collected using a Zeiss Versa 620 with a voxel size of 2.5  $\mu$ m. DCT projections were reconstructed using the commercial software GrainMapper3DTM developed by Xnovo Technology ApS. Back-scattered X-ray Laue diffraction was collected with a tungsten source operating at 10 kV and 10 mA with a Multiwire Laboratories MWL 110 real-time back reflection Laue camera. The tool MuCalc (<https://www.ctlab.geo.utexas.edu/software/mucalctool/>) was used to plot attenuation versus X-ray energy, drawing data from the NIST XCOM database. [29] Crystal structures were visualized using Vesta software. [30]

## Results and Discussion

### Volumetric Measurements

Figure 5-1 shows a general schematic of the key components of a  $\mu$ CT instrument. In this technique, X-rays transmits through the sample from a polychromatic source,

Sample	Point-Spread Function (vox)
Figure 2a	7.9(6)
Figure 3c	11.8(3)
Figure 3d	11.1(8)
Figure 4c	7(1)
Figure 4f	6.9(9)
Figure 5b	8.4(8)
Figure 6b	1.5(4)

**Table 5-I.** The point-spread function radius for each CT dataset is shown to give an estimation of length of distinguishable features.

usually following a cone or fan beam geometry. The X-rays then hit the scintillation detector, collecting a series of images while the sample rotates on a platform by 180° or 360° (dependent on sample geometry). From this point the collection of images is used to reconstruct the 3D sample, typically done using a filtered back-projection algorithm. There are a variety of collection/reconstruction strategies and algorithms to avoid artifacts that are better addressed in related reviews. [19, 31] The reconstruction is a 3D representation, with voxel (3D pixel) by voxel contrast measurement (e.g. Beer’s law in the case of X-ray attenuation contrast). This contrast allows for the characterization of a variety of defects that plague electronic and quantum materials, examples of which are shown in Figure 5-1 in accordance with the time and length scales they occur. Common inhomogeneities that impact materials’ properties, along with their corresponding dimensionalities, are listed in Table 5-II, adapted from Peter Rudolph. [32] These are wide ranging in dimensionality and much work has been dedicated to controlling their origin. [33–40]

A simple measurement attained from  $\mu$ CT is sample geometry down to  $\sim\mu\text{m-nm}$  resolution. This is especially helpful for thermal/electrical transport measurements of geometrically complex samples where an accurate volume or cross-sectional area are still needed. It enables determination of density, as well as observation of voids or cracks that can impact the transport properties. [41] Alongside techniques such as resonant ultrasound spectroscopy, it also enables rigid body simulations for determining

Type of Defect	Dimensionality
Point Defects (Interstitial/Vacancies)	0D
Dislocation	1D
Swirl Loop	1D
Grain Boundary	2D
Crystal Twinning	2D
Facets	2D
Precipitates	3D
Inclusions	3D
Voids	3D

**Table 5-II.** A list of some common inhomogeneities that can impact a material's properties, adapted from Peter Rudolph.

vibrational response, allowing extraction of phonon properties.

These volumetric measurements can be helpful when one is doing a high throughput search of materials where crystal growth may be too difficult or time consuming, instead relying on well-compacted powders using instruments such as a spark plasma sintering system. [42] In this example, being able to calculate the porosity, or % volume of voids in relation to the total volume, would be useful for comparison. Fig. 2a shows an example of Cu powder that was cold pressed to better emphasize the size of voids that can occur. As air is less attenuating than the bulk, the voids can be easily visualized and then quantified using  $\mu$ CT. One can quantify the number of voids to be 67 and their volume distribution can be visualized in the histogram distribution in Fig. 2b. In this example, most voids are a volume of similar magnitude of each other. While other techniques can be used to quantify pores,  $\mu$ CT gives us a look at the 3D structure, highlighting internal voids that may be more difficult to characterize. This type of measurement expands the characterization methods possible in determining sample quality, bolstering the validity of the results of transport measurements.

## Flux Crystal Growth

The previous example showed an important insight in the application of  $\mu$ CT, that sample components can be distinguished and visualized non-destructively throughout the bulk. This contrast method can occur when the compounds have different attenuation coefficients in the operating X-ray voltage of the instrument. This ability can be put to great use in flux crystal growth. In the flux method, one uses an excess of a compound to dissolve the desired material below its melting point, where upon gradual cooling the flux reaches supersaturation resulting in crystallization of the target sample. This technique is widely used in materials discovery as a low-cost method to grow millimeter scale crystals. [43, 44]

For both oxides and metals, one would normally use a flux that is chemically related to the target material, but sometimes an unrelated compound must be used. Poor selection of flux would result in a mixture of phases and poor crystallite size, where  $\mu$ CT could be utilized to help understand the growth formation mechanisms and segregation of phases if combined with a secondary technique such as powder X-ray diffraction to understand phase composition. Even use of a “successful” flux can still result in inclusions in the sample that can impact materials properties, as well as be indistinguishable without destroying the crystal. [45]

A classic example of this is the material  $\text{SmB}_6$ , a well-known Kondo insulator with reported quantum oscillations that supports the suspected topological behavior. [46] The most common method to grow this material is by using an excess of Al flux, which can show up as inclusions. [21] Figure 5-3a is a graph of the attenuation coefficients of Al and  $\text{SmB}_6$  as a function of x-ray voltage showing that provided one is in the right range of energy (in this case the operating range of the instrument), it is easy to distinguish these inclusions from the bulk sample. A comparison of the crystal structure between  $\text{SmB}_6$  and Al in Figure 5-3b shows that given the similar structure

and lattice parameter, the two materials will likely seed the growth of one another. Fig 5-3c and d demonstrates this, where flux grown SmB<sub>6</sub> crystals with epitaxially grown Al inclusions is visualized using  $\mu$ CT. Measurements of samples while systematically thinning the crystal shows a disappearance in the quantum oscillations. [47] Since the presence of Al makes it difficult to elucidate the inherent characteristic behavior of SmB<sub>6</sub>,  $\mu$ CT can be combined with other measurements (such as bulk magnetization) as an effective way to non-destructively screen samples.

## Anisotropic Measurements/Visualization

Screening samples is helpful, but in this example  $\mu$ CT also gives us new information regarding the formation of these extended features. Not only do we see the presence of inclusions, but we also see that they are not uniformly distributed throughout the sample and instead develop a preferred orientation. The absorption data collected lets us quantify the size, distribution, and orientation of these inclusions using software such as Blob3D and Quant3D. [28, 48]

One measurement that can be performed is the star volume distribution (SVD), with other examples being the mean intercept length and star length distribution. For a distribution of points in the segmented data, the SVD determines the distance traveled before interception of a boundary, with the measurement performed over the volume of the specimen. [49] We can use such measurements of the Al to calculate a degree of anisotropy of 0.96 (where a value of 0 is completely isotropic and 1 is completely anisotropic). The ratio of the largest eigenvalue over the smallest is another measure of the degree of anisotropy (DA) and is 220(20) for Figure 5-3c. We can then further generate a 3D rose diagram, a projection of the calculated SVD measurements, to visualize the directionality of these features relative to the crystal itself, as seen in Figure 5-3e. The diagram shows that the inclusions preferentially grow along the length of the crystal.

As the same material can form different crystal habits,  $\mu$ CT as a tool affords us the opportunity to compare the inclusions between different crystal shapes of  $\text{SmB}_6$ , previously never investigated in the community. The more cuboid shaped crystals, as rendered in Figure 5-3d, show sheets of aluminum form perpendicular to the main crystal axis. The eigenvalue DA determined through Quant3D is. 2.75(9). A visualization of the Al using a 3D rose diagram of the SVD in Figure 5-3f shows a different form of anisotropy compared to the  $\text{SmB}_6$  rods. In this case, two competing sheet like layers are developed in opposing crystalline directions. The data shows that in the discovery of new quantum materials, extended features do matter and techniques such as  $\mu$ CT should be implemented to carefully examine the distribution of such inhomogeneities. Further work can be performed using this method to analyze inclusions of other materials exhibiting quantum oscillations to correlate the orientation with the quantum oscillation frequency. [50]

While  $\text{SmB}_6$  serves as a shining example of the power of  $\mu$ CT, this technique can be used beyond detecting defects to also help optimize crystal growth parameters. This is demonstrated in the case of rutile  $\text{GeO}_2$  (r- $\text{GeO}_2$ ), an ultra-wide band gap semiconductor with predicted ambipolar doping. Much work has been invested in the development of controlled defects in bulk and thin film samples to invoke these aforementioned properties for electronic devices. [24, 51, 52] Here we discuss the improvement in crystal quality of flux grown single crystals of r- $\text{GeO}_2$ . In flux growths, the cooling rate can have a large impact on not only the size, but also the quality of the crystals obtained. In Figure 5-4a we see a single crystal of r- $\text{GeO}_2$  grown using flux method with a cooling rate of 3° C/hr. Laue diffraction shown in Figure 5-4b gives clear, defined spots along one of the facets.

Further inspection using X-ray  $\mu$ CT in Figure 5-4c shows voids present in the sample. We calculate the degree of anisotropy to be 0.79, with a 3D rose diagram generated in Figure 5-4d. The eigenvalue DA determined through Quant3D is 7.6(7).

In this instance, the axes were aligned to the [011] direction, showing a preferred orientation of the voids parallel to the crystal facet. A similar crystal of r-GeO<sub>2</sub> cooled at a rate of 0.5° C/hr through the same temperature range shows no sign of voids above the  $\mu\text{m}$  scale. The improved quality of this crystal is seen in the optical microscope image of Figure 5-4e, and the volumetric rendering shown in Figure 5-4f. This example follows the common logic that a slower growth leads to better quality crystals, although this need not always be the case. Through this comparison we show how  $\mu\text{CT}$  can be implemented in flux crystal growth to screen crystals for inclusions as well as help optimize the growth parameters. We also see that dependent on the crystal habits, one can quantify features accurately along crystallographic orientations.

## Floating Zone Crystal Growth

Flux growth has been the primary form of synthesis discussed so far, but X-ray  $\mu\text{CT}$  can assist other synthesis approaches and crystal growth methods. Techniques involving directional solidification, such as Bridgman and floating zone, can also be affected by inclusions as well as voids and air pockets that incorporate into the grown crystal. [53–55] These defects impact crystal quality but can be prevented by improvements in sample preparation or changes in the growth parameters. An example of this can be considered in the floating zone technique. Internal voids can form in this technique due to air pockets in poorly densified rods as well as the generation of gas as a side product when the compound melts. [56] A less obvious method of void formation is due to the gas environment itself. While applied pressure of different gas species can be useful in floating zone growths to reduce volatility or stabilize certain oxidation states, it can be detrimental to growth stability as well. [57, 58]

We demonstrate the applicability of  $\mu\text{CT}$  in analyzing these internal voids in the floating zone growth of YbMgGaO<sub>4</sub>. This material, whose crystal structure is shown in Figure 5-5a, is a quantum spin liquid candidate due to the frustrated triangular

lattice Yb<sup>3+</sup> ions occupy. [25, 59]  $\mu$ CT data collected on a section of a sample grown in PARADIM’s 300 bar optical high pressure floating zone is visualized in Figure 5-5b to highlight the presence of internal voids. In this case a larger applied pressure of 20 bar of O<sub>2</sub> gas led to void formation compared to an applied pressure of 5 bar done in previous papers, likely due to the dissolution of the gas at higher pressures.

Figure 5-5c shows an optical microscope image of the melt as support for both the presence of detectable voids as well as their directionality. To further understand the anisotropic nature of these features, the relative orientations of the voids according to their volume are shown using a contour plot in Figure 5-5d. The larger voids tend to cluster around certain areas of orientation, showing a weak anisotropy present as a function of volume, supported by the calculated degree of anisotropy being 0.39. This intuitively makes sense, as the larger size pockets are present in the growth for a longer time and hence have more directionality applied to them because of the growth method itself. Examining the distance between the largest pockets show angles of  $\sim 30^\circ$  and  $\sim 120^\circ$ , supporting the proposed trigonal structure of the material.

## Diffraction Computed Tomography and Other Future Directions

All experiments shown so far were accomplished using a typical lab-bench sized  $\mu$ CT instrument, showcasing the power of this technique in an accessible research environment. Further advances in instrumentation open new possibilities in using  $\mu$ CT to inform materials synthesis. The onset of accessible hyperspectral detectors has given  $\mu$ CT the ability to perform 3D bulk elemental analysis on the scale of  $\mu\text{m}$ . [60] This capability could easily be applied to materials synthesis involving complex phase diagrams. In these cases, distinguishing between the different components may not be naively easy without the use of hyperspectral detectors.

Where hyperspectral detector allows for elemental analysis, Diffraction  $\mu$ -Computed

Tomography (DCT) allows for orientation analysis of 3D volumes of both polycrystalline and single crystalline samples. [61] This has already had some use in ceramics to track grain growth while sintering and has been shown to inform crystal morphology in materials discovery. [62, 63] Being able to follow grain selection in floating zone growths using DCT could be used alongside current methods to allow for a better optimization of growth conditions. [26]

An example of such visualization is shown in Figure 5-6a, where we have performed DCT on a floating zone-grown crystal of rutile TiO<sub>2</sub>. Since rutile and other similar materials are desired for their large birefringence, low angle grain boundaries can be harmful to their optical properties. [64, 65] The grains are clearly highlighted in the diffraction data, as this was a piece from early in the growth where multiple domains are still competing. An interesting observation in the absorption data is shown in Figure 5-6b, where a Sobel filter was applied to emphasize edges. Without any knowledge of the diffraction data, one can still visualize some grains due to inherent gaps created between the domains. This can lead to normal  $\mu$ CT being a useful screener prior to DCT in identifying potential boundaries present. We can use the combined data to determine domains for sample extraction, as well as to understand more about growth mechanisms occurring, in particular for cases where competing polytypes and intergrowths could be occurring. [66, 67]

Techniques such as in-situ XRD available at synchrotron facilities already allow for novel insights into sample synthesis routes. [68, 69] Current  $\mu$ CT instruments allow for application of heating, cooling, and force to examine changes over time. Applying in-situ  $\mu$ CT in a crystal growth process would take us one step further and allow one to have pseudo “real-time” response to conditions to avoid defects and inclusions. A traditional floating zone set-up that incorporates translating/rotating samples could be adapted for such a purpose, where once steady state has been achieved, a crystal growth is occurring at a (normal) slow rate and rotating for each collection of images.

While data sets of  $\mu$ CT are normally gigabytes to terabytes in size, to process and describe this amount of data is an example of “big” data challenges the community needs to address in the future of guided materials discovery.

The numerous advantages of this technique should still be considered within its limitations. By and large the biggest detractor to the technique is the limit in resolution for the voxel size. While synchrotron sources improve this, one still only gets to nanometer level resolution. Features near the resolution of the instrument can also experience blurring artifacts that make it difficult to accurately quantify the size. The user may be limited in what X-ray voltage they can operate in if the sample is too attenuating or thick to achieve enough signal. This would limit certain contrast mechanisms such as absorption from being utilized. Finally, more defined rules of thumb for image segmentation and quantification, often helped to be define by the instrument and software developers, would enable quantified results to be comparable across the community.

## Conclusion

Throughout this review, we have shown the capabilities of  $\mu$ CT in aiding materials design. The data collected through this technique can aid other characterization methods through the calculation of volumes and quantification of pore sizes for transport measurements. The detection of inclusions can help non-destructively screen samples for quality as well as give insight into defect formation/orientation. Sample synthesis can be improved upon through analysis of extended features such as voids that are sometimes hidden in other techniques. Finally, we showed how advances in  $\mu$ CT instrumentation can expand upon the current capabilities by allowing for elemental and orientation analysis as well as in situ-measurements. Overall  $\mu$ CT is an effective non-destructive characterization tool that can be widely implemented throughout the materials community to assist in the synthesis of electronic and

quantum materials.

## Acknowledgements

This work was funded by the Platform for the Accelerated Realization, Analysis, and Discovery of Interface Materials (PARADIM), a National Science Foundation Materials Innovation Platform (NSF DMR-2039380). The UTCT facility is partially supported by NSF grant EAR 176245 with funding for the Zeiss Versa 620 funded by NSF MRI grant EAR-1919700. Access to the Bruker 1172 instrument was also possible via the Hopkins Extreme Materials Institute (HEMI). L.A.P, T.M.M, and M.A.K would like to thank Navindra Keerthisinghe, Vicky Li, Trent Kyrk, and Olivia Vilella for their group participation in the high-pressure floating zone growth of  $\text{YbMgGaO}_4$  at the 2021 PARADIM Summer School at JHU. L.A.P would like to thank Jessica Maisano for assistance with DCT data collection and Juan Chamorro for helpful discussions and providing  $\text{SmB}_6$  samples for analysis. Raw data from the facility related to these experiments is available after publication at <https://data.paradim.org>.

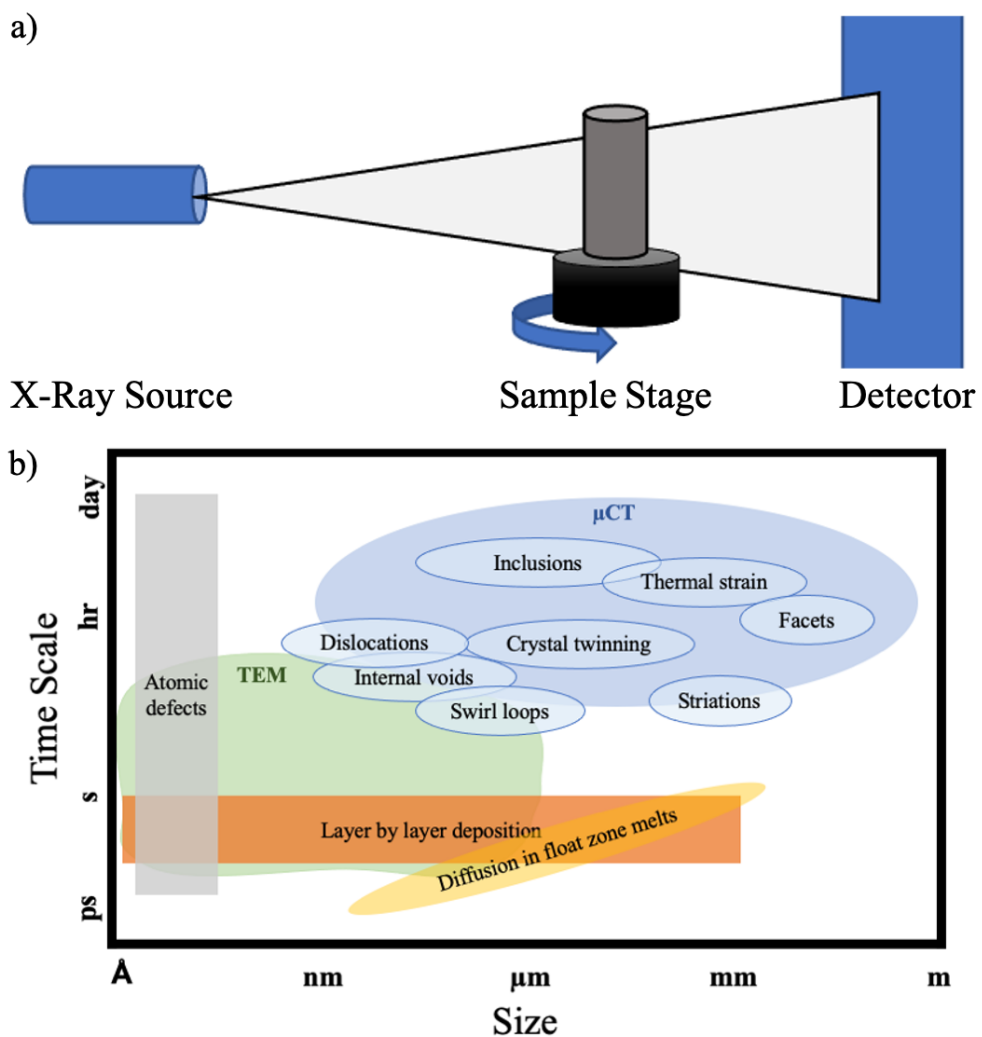


**Figure 5-1.** a) A representation of the key components in a  $\mu\text{CT}$  instrument. The x-ray source shown generates x-rays in a cone-beam geometry as they transmit through the sample and hit the scintillation detector, all while the sample rotates on a stage. b) A comparison of the various time and length scales defects can form in electronic and quantum materials.

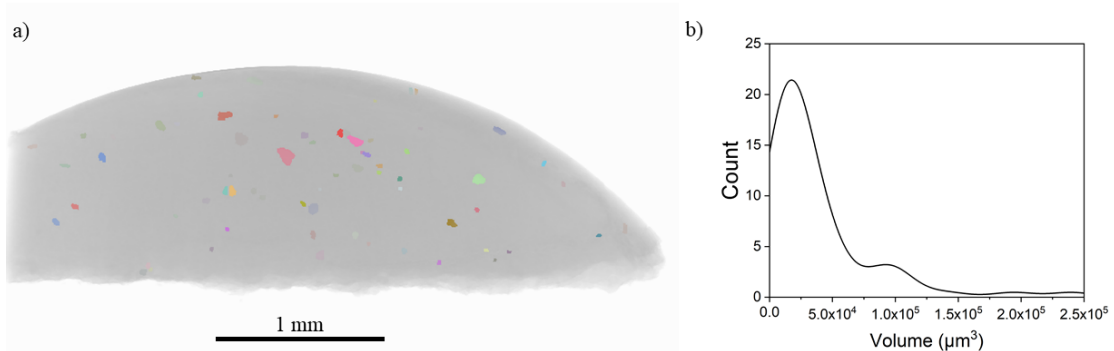


**Figure 5-2.** a) A 3D rendering of a portion of cold pressed Cu powder with voids in the sample colored to distinguish and emphasize their dispersal throughout the sample. b) A histogram distribution of volume for the various voids present.

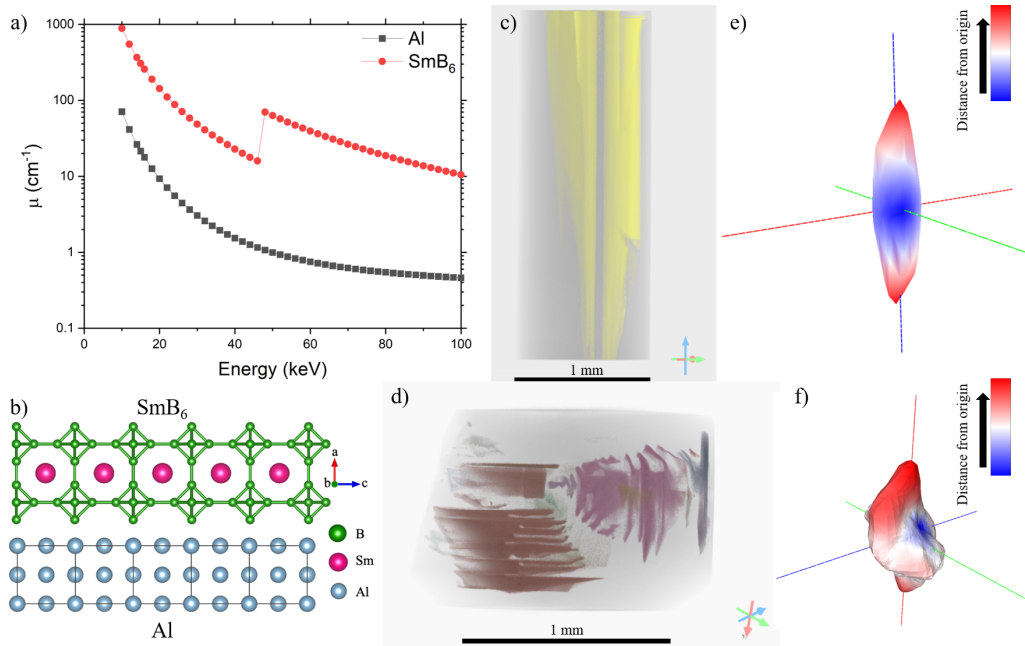


**Figure 5-3.** a) A comparison of the attenuation coefficients of Al and SmB<sub>6</sub> as a function of x-ray energy in the operating range of the instrument, demonstrating the feasibility of contrasting the two components using  $\mu$ CT. The K-edge for SmB<sub>6</sub> lies between 40-60 keV, resulting in the dip of attenuation. b) Visualizations of the crystal structure of SmB<sub>6</sub> and Al, demonstrating that given the similar lattice parameter, both systems mutually support the growth of one another c) A 3D rendering of a crystal of SmB<sub>6</sub> showing the presence of Al inclusions (colored yellow) that are epitaxially oriented. d) A rendering of a different crystal of SmB<sub>6</sub> with Al inclusions showing up as epitaxially oriented layered sheets. e) A 3D rose diagram generated from the star volume distribution (SVD) of the inclusions of (c). The data is oriented along the length of the crystal, showing a preferred growth direction following the crystal habit. The image is colored according to distance from origin f) A 3D rose diagram generated from the SVD of the inclusions of (d), showing the impact the opposing layers have on the overall anisotropy. The image is colored according to distance from origin

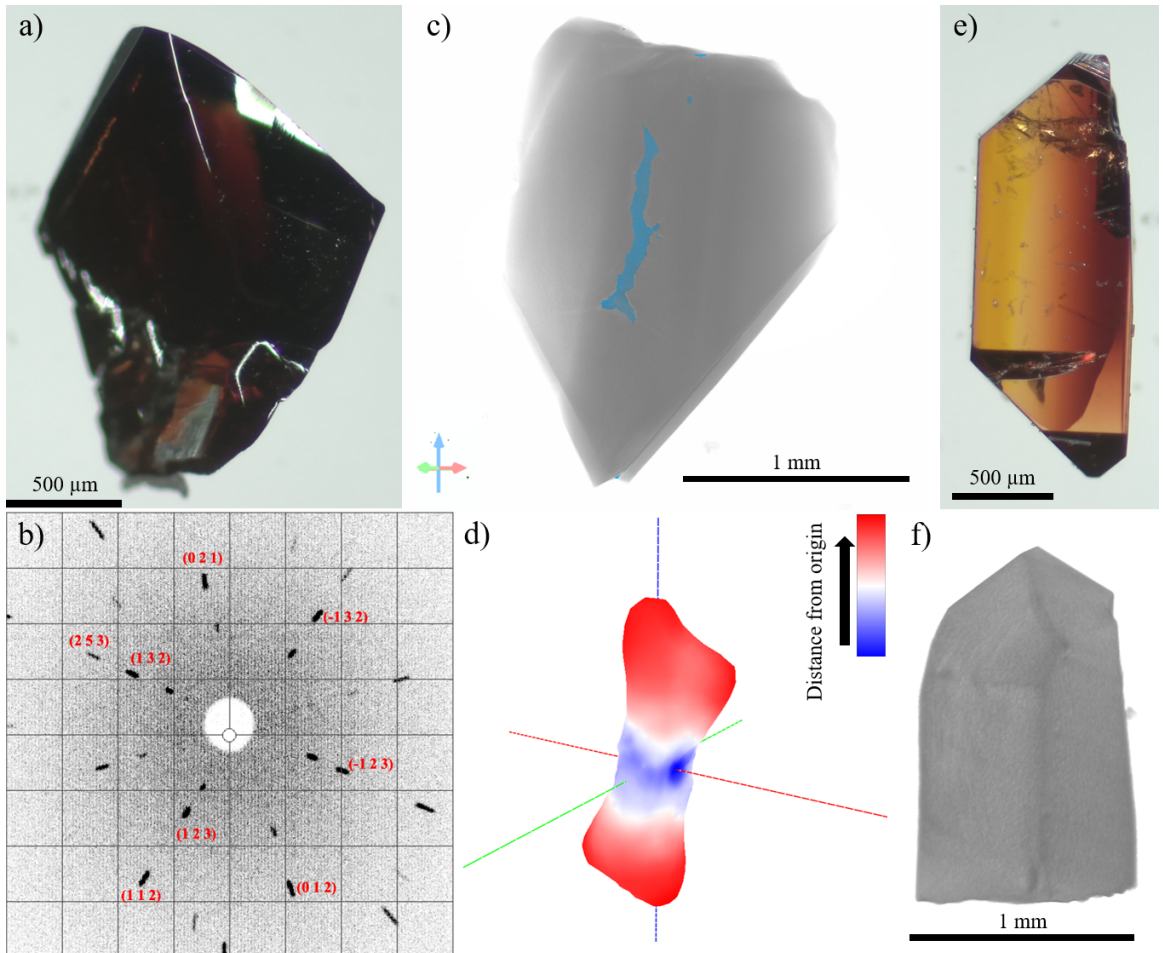


**Figure 5-4.** A single crystal of rutile- $\text{GeO}_2$  grown using a flux with a cooling rate of  $3^\circ \text{C/hr}$ . b) Laue diffraction image of the crystal along the [011] direction. c) A representation of a crystal from the same batch as (a) generated from  $\mu\text{CT}$  data with voids present (highlighted blue). d) A 3D rose diagram of the star volume distribution of the voids. The data was aligned such that the void shows a preferential orientation parallel to the [011] direction of the crystal axis. The image is colored according to distance from origin. e) A different crystal of rutile- $\text{GeO}_2$  grown using a flux with a cooling rate of  $0.5^\circ \text{C/hr}$ . f) A rendering of a crystal from the same batch as (e) showing no detectable voids.

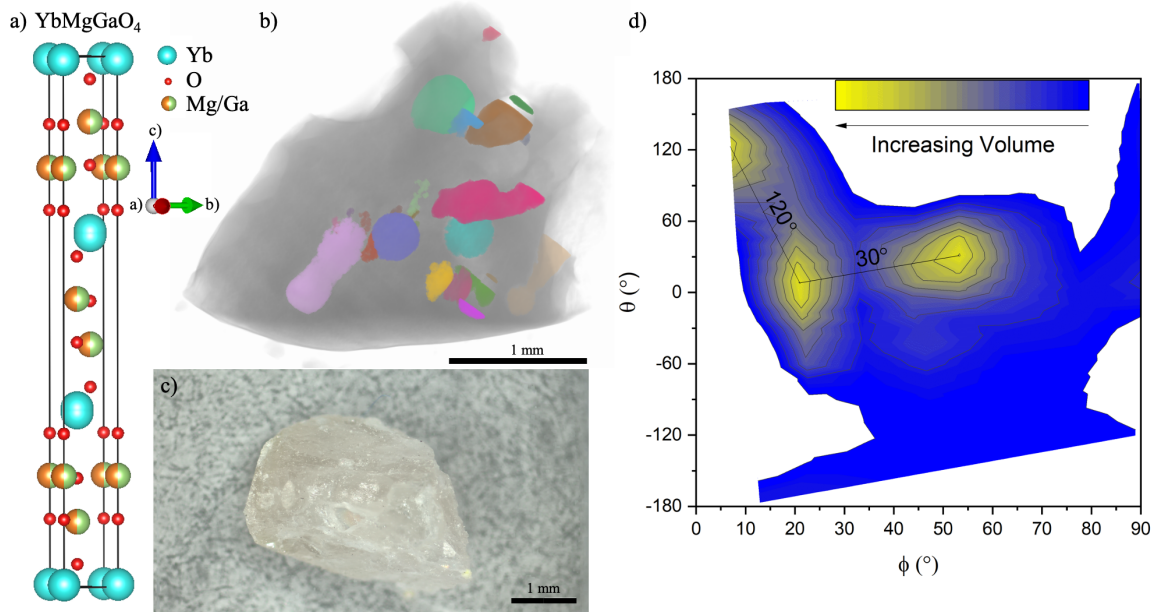


**Figure 5-5.** a) The crystal structure of YbMgGaO<sub>4</sub> showing its trigonal nature b) A rendering of the melt from a high-pressure floating zone growth of YbMgGaO<sub>4</sub> characterized by  $\mu$ CT to highlight the presence of internal voids, colored to be visually distinct from one another. c) An optical microscope image of the melt from the growth, showing the presence of external voids detectable by the eye. d) A contour map of the melt's void volume as a function of their relative orientation. Weak anisotropy is present as the samples grow larger in volume. Distances between the largest size voids are emphasized to show the directionality obeying the trigonal structure.

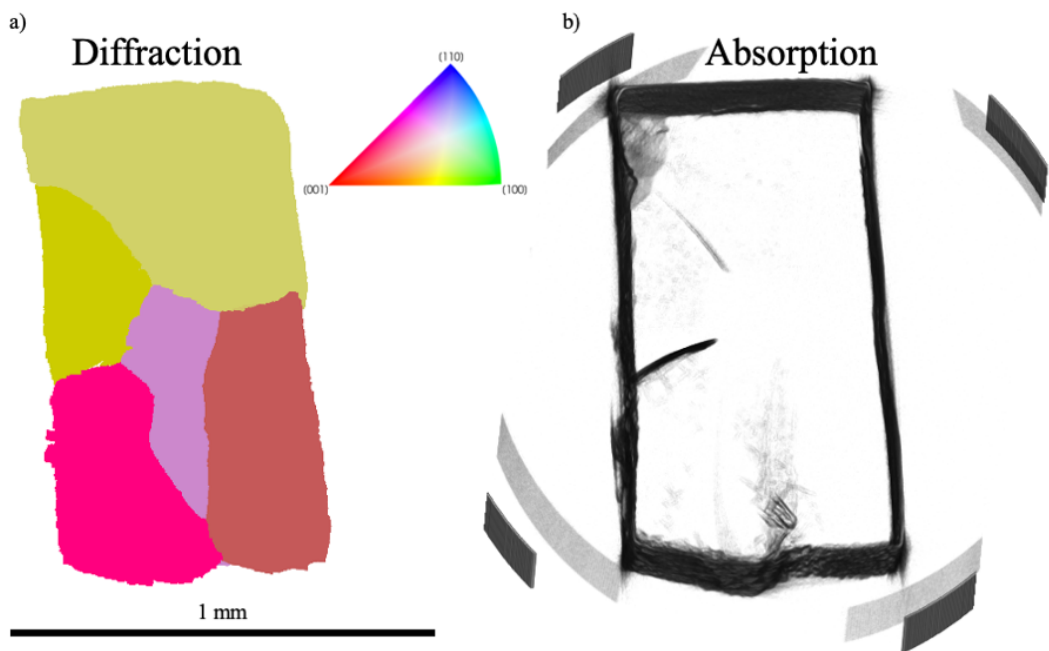


**Figure 5-6.** Floating zone-grown rutile-TiO<sub>2</sub> is visualized in both a) diffraction CT and b) absorption CT data. Multiple crystalline domains are present in the sample, as is expected for an early-stage portion of the growth. The absorption data shown has had a Sobel filter applied to highlight the edges.

# References

1. Council, N. R. *Frontiers in crystalline matter: From discovery to technology* (The National Academies Press, Washington, DC, 2009).
2. Broholm, C. *et al.* Basic research needs workshop on quantum materials for energy relevant technology 2016.
3. Sarrao, J. & Kwok, W.-K. On opportunities for basic research in superconductivity focused on science and energy relevant technologies 2006.
4. Thornton, P. A. The influence of nonmetallic inclusions on the mechanical properties of steel: a review. *Journal of Materials Science* **6**, 347–356 (1971).
5. Zhang, L. & Thomas, B. G. State of the art in the control of inclusions during steel ingot casting. *Metallurgical and Materials Transactions B* **37**, 733–761 (2006).
6. Zhang, P. *et al.* Enhancing carrier transport properties of melt-grown CsPbBr<sub>3</sub> single crystals by eliminating inclusions. *Crystal Growth and Design* **20**, 2424–2431 (2020).
7. Zhang, L. T., Tsutsui, M., Ito, K. & Yamaguchi, M. Effects of ZnSb and Zn inclusions on the thermoelectric properties of  $\beta$  – Zn<sub>4</sub>Sb<sub>3</sub>. *Journal of Alloys and Compounds* **358**, 252–256 (2003).
8. Gurevich, A. & Pashitskii, E. A. Current transport through low-angle grain boundaries in high-temperature superconductors. *Physical Review B* **57**, 13878 (1998).
9. Durrell, J. H. & Rutter, N. A. Importance of low-angle grain boundaries in YBa<sub>2</sub>Cu<sub>3</sub>O<sub>7- $\delta$</sub>  coated conductors. *Superconductor Science and Technology* **22**, 013001 (2009).
10. Maeno, Y. *et al.* Enhancement of superconductivity of Sr<sub>2</sub>RuO<sub>4</sub> to 3 K by embedded metallic microdomains. *Physical Review Letters* **81**, 3765–3768 (1998).
11. Jin, R., Zadorozhny, Y. & Liu, Y. Observation of anomalous temperature dependence of the critical current in Pb/Sr<sub>2</sub>RuO<sub>4</sub>/Pb junctions. *Physical Review B* **59**, 4433–4438 (1999).
12. Ying, Y. A. *et al.* Enhanced spin-triplet superconductivity near dislocations in Sr<sub>2</sub>RuO<sub>4</sub>. *Nature Communications* **4** (2013).
13. Bianco, E. & Kourkoutis, L. F. Atomic-resolution cryogenic scanning transmission electron microscopy for quantum materials. *Accounts of Chemical Research* **54**, 3277–3287 (2021).
14. Venables, J. A., Smith, D. J. & Cowley, J. M. HREM, STEM, REM, SEM-and STM. *Surface Science* **181**, 235–249 (1987).
15. Becker, J. S. & Dietze, H.-J. Inorganic trace analysis by mass spectrometry. *Spectrochimica Acta Part B: Atomic Spectroscopy* **53**, 1475–1506 (1998).

16. Stock, S. X-ray microtomography of materials. *International Materials Reviews* **44**, 141–164 (1999).
17. Ritman, E. L. Micro-computed tomography-current status and developments. *Annual Review of Biomedical Engineering* **6**, 185–208 (2004).
18. Rawson, S. D., Maksimcuka, J., Withers, P. J. & Cartmell, S. H. X-ray computed tomography in life sciences. *BMC Biology* **18** (2020).
19. Hanna, R. D. & Ketcham, R. A. X-ray computed tomography of planetary materials: a primer and review of recent studies. *Geochemistry* **77**, 547–572 (2017).
20. Vásárhelyi, L., Kónya, Z., Kukovecz, Á. & Vatjai, R. Microcomputed tomography-based characterization of advanced materials: a review. *Materials Today Advances* **8** (2020).
21. Phelan, W. *et al.* On the chemistry and physical properties of flux and floating zone grown SmB<sub>6</sub> single crystals. *Scientific Reports* **6** (2016).
22. Berry, T., Pressley, L. A., Phelan, W. A., Tran, T. T. & McQueen, T. M. Laser enhanced single crystal growth of non-symmorphic materials: applications to an eight-fold fermion candidate. *Chemistry of Materials* **13**, 5827–5834 (2020).
23. Sinha, M. *et al.* Twisting of 2D kagome sheets in layered intermetallics. *ACS Central Science* **7**, 1381–1390 (2021).
24. Niedermeier, C. A., Ide, K., Katase, T., Hosono, H. & Kamiya, T. Shallow valence band of rutile GeO<sub>2</sub> and P-type doping. *Journal of Physical Chemistry C* **124**, 25721–25728 (2020).
25. Li, Y. *et al.* Rare-earth triangular lattice spin liquid: A single-crystal study of YbMgGaO<sub>4</sub>. *Physical Review Letters* **115**, 167203 (2015).
26. Wright, C. J. ". *et al.* Toward in situ synchrotron mapping of crystal selection processes during crystal growth. *Chemistry of Materials* **33**, 3359–3367 (2021).
27. Ketcham, R. A. & Hildebrandt, J. Characterizing, measuring, and utilizing the resolution of CT imagery for improved quantification of fine-scale features. *Nuclear Instruments and Methods in Physics Research B* **324**, 80–87 (2014).
28. Ketcham, R. A. Computational methods for quantitative analysis of three-dimensional features in geological specimens. *Geosphere* **1**, 32–41 (2005).
29. Berger, M. J. *et al.* XCOM: photon cross section database (2010).
30. Momma, K. & Izumi, F. VESTA: a three-dimensional visualization system for electronic and structural analysis. *Journal of Applied Crystallography* **41**, 654–658 (2008).
31. ASTM. in *Annual Book of ASTM Standards, Section 3 Metals Test Methods and Analytical Procedures* 690–713 (Philadelphia, 1992).
32. Rudolph, P. in *Handbook of Crystal Growth* 159–201 (Springer Heidelberg Dordrecht London New York, 2010).
33. Hu, Z. W. *et al.* Synchrotron topographic characterization of Fe-doped flux-grown Potassium Niobate Tantalate. *Applied Physics Letters* **61** (1992).
34. Sadrabadi, P. *et al.* Evolution of dislocation structure and deformation resistance in creep exemplified on single crystals of CaF<sub>2</sub>. *Materials Science and Engineering: A* **510-511**, 46–50 (2009).

35. Cockayne, B. Developments in melt-grown oxide crystals. *Journal of Crystal Growth* **3-4**, 60–70 (1968).
36. Wang, X., Wang, J., Yu, Y., Zhang, H. & Boughton, R. I. Growth of cubic  $\text{KTa}_{1-x}\text{Nb}_x\text{O}_3$  crystal by Czochralski method. *Journal of Crystal Growth* **293**, 398–403 (2006).
37. Polgár, K., Peter, Á., Földvári, I. & Szaller, Z. Structural defects in flux-grown stoichiometric  $\text{LiNbO}_3$  single crystals. *Journal of Crystal Growth* **218**, 327–333 (2000).
38. Saeedi, H. *et al.* Thermal shocks influence on the growth process and optical quality of Nd: YAG crystal. *Journal of Crystal Growth* **363**, 171–175 (2013).
39. Föll, H. & Kolbesen, B. O. Formation and nature of swirl defects in silicon. *Applied Physics* **8**, 319–331 (1975).
40. Falster, R. & Voronkov, V. V. The engineering of intrinsic point defects in silicon wafers and crystals. *Materials Science and Engineering: B* **73**, 87–94 (2000).
41. Montes, J. M., Rodríguez, J. A. & Herrera, E. J. Thermal and electrical conductivities of sintered powder compacts. *Powder Metallurgy* **46**, 251–256 (2013).
42. Rondinelli, J. M. *et al.* Accelerating functional materials discovery. *American Ceramic Society Bulletin* **92** (2013).
43. Phelan, W. A. *et al.* Adventures in crystal growth: synthesis and characterization of single crystals of complex intermetallic compounds. *Chemistry of Materials* **24**, 409–420 (2012).
44. Bugaris, D. E. & Loyer, H.-C. z. Materials discovery by flux crystal growth: quartnerary and higher order oxides. *Angewandte Chemie - International Edition* **51**, 3780–3811 (2012).
45. Canfield, P. C. & Fisk, Z. Growth of single crystals from metallic fluxes. *Philosophical Magazine B* **65**, 1117–1123 (1991).
46. Rosa, P. F. S. & Fisk, Z. in *Rare-Earth Borides* 1st, 817–875 (Jenny Stanford Publishing, 2021).
47. Thomas, S. M. *et al.* Quantum oscillations in flux-grown  $\text{SmB}_6$  with embedded aluminum. *Physical Review Letters* **112** (2019).
48. Ketcham, R. A. Three-dimensional grain fabric measurements using high-resolution X-ray computer tomography. **2**, 1217–1228 (2005).
49. Smit., T. H., Schneider, E. & Odgaard, A. Star length distribution: a volume-based concept for the characterization of structural anisotropy. *Journal of Microscopy* **191**, 249–257 (1998).
50. Naumann, M. *et al.* Fermi surface of the Skutterudite  $\text{CoSb}_3$ : quantum oscillations and band-structure calculations. *Physical Review B* **103**, 085133 (2021).
51. Chae, S. *et al.* Toward the predictive discovery of ambipolarly dopable ultra-wide-bandgap semiconductors: The case of rutile  $\text{GeO}_2$ . *Applied Physics Letters* **118** (2021).
52. Takane, H. & Kaneko, K. Establishment of a growth route of crystallized rutile  $\text{GeO}_2$  thin film ( $\geq 1 \mu\text{m}/\text{h}$ ) and its structural properties. *Applied Physics Letters* **119**, 062104 (2021).
53. Morey, J. R. *et al.* Growth and characterization of Iron Scandium Sulfide ( $\text{FeSc}_2\text{S}_4$ ). *Journal of Crystal Growth* **454**, 128–133 (2016).

54. Yu, P. *et al.* Correlation between Te inclusions and the opto-electrical properties of CdMnTe and CdMgTe single crystals. *Journal of Crystal Growth* **571**, 126259 (2021).
55. Su, H. *et al.* Distribution control and formation mechanism of gas Inclusions in directionally solidified Al<sub>2</sub>O<sub>3</sub> – Er<sub>3</sub>Al<sub>5</sub>O<sub>12</sub> – ZrO<sub>2</sub> ternary eutectic ceramic by laser floating zone melting. *Journal of Materials Science & Technology* **66**, 21–27 (2021).
56. Berry, T., Bernier, S., Auffermann, G., McQueen, T. M. & Phelan, W. A. Laser Floating Zone Growth of SrVO<sub>3</sub> Single Crystals. *Journal of Crystal Growth* **583**, 126518 (2022).
57. Dabkowska, H. A. & Dabkowski, A. B. in *Springer Handbook of Crystal Growth* 367–390 (Springer Heidelberg Dordrecht London New York, 2010).
58. Phelan, W. A., Zahn, J., Kennedy, Z. & McQueen, T. M. Pushing boundaries: high pressure, supercritcal optical floating zone materials discovery. *Journal of Solid State Chemistry* **270**, 705–709 (2019).
59. Paddison, J. A. M. *et al.* Continuous excitations of the triangular-lattice quantum spin liquid YbMgGaO<sub>4</sub>. *Nature Physics* **13**, 117–122 (2017).
60. Egan, C. *et al.* 3D chemical imaging in the laboratory by hyperspectral X-ray computed tomography. *Scientific Reports* **5** (2015).
61. Ludwig, W. *et al.* Three-dimensional grain mapping by X-ray diffraction contrast tomography and the use of Friedel pairs in diffraction data analysis. *Review of Scientific Instruments* **80**, 033905 (2009).
62. McDonald, S. *et al.* Microstructural evolution during sintering of copper particles studied by laboratory diffraction contrast tomography (LabDCT). *Scientific Reports* **7** (2017).
63. Qu, K. *et al.* Morphology and growth habit of the new flux-grown layered semiconductor KBiS<sub>2</sub> revealed by diffraction contrast tomography. *Crystal Growth and Design* **22**, 3228–3234 (2022).
64. Higuchi, M., Hosokawa, T. & Kimura, S. Growth of rutile single crystals by floating zone method. *Journal of Crystal Growth* **112**, 354–358 (1991).
65. Hu, B. Q., Zhang, Y. Z., Wu, X. & Chen, X. L. Defects in large single crystals Nd:YVO<sub>4</sub>. *Journal of Crystal Growth* **226**, 511–516 (2001).
66. Witteveen, C. *et al.* Polytypism and superconductivity in the NbS<sub>2</sub> System. *Dalton Transactions* **50**, 3216–3223 (2021).
67. Sung, N. H. *et al.* Crystal growth and intrinsic magnetic behavior of Sr<sub>2</sub>IrO<sub>4</sub>. *Philosophical Magazine* **96**, 413–426 (2016).
68. Haynes, A. S., Stoumpos, C. C., Chen, H., Chica, D. & Kanatzidis, M. G. Panoramic synthesis as an effective materials discovery tool: the system Cs/Sn/P/Se as a test case. *Journal of the American Chemical Society* **139**, 10814–10821 (2017).
69. Xia, F. *et al.* Understanding solvothermal crystallization of mesoporous anatase beads by in situ synchrotron PXRD and SAXS. *Chemistry of Materials* **26**, 4563–4571 (2014).

# Chapter 6

## Optimization of PbTiO<sub>3</sub> single crystals with flux and laser floating zone method

### Introduction

Multiferroics, materials that exhibit two or more types of ordering below their corresponding Curie temperatures, are a highly desired class of materials due to their impact as potential memory devices. [1, 2] Of particular interest is the coupling between systems that demonstrate ferromagnetism and ferroelectricity. The perovskite family has served as a useful structure in designing multiferroics, as many already exhibit one of the features needed to be classified as such. [3, 4] Lone pair sterically active materials are often pursued due to the structural distortion present that gives rise to ferroelectricity. [5] Thus, PbTiO<sub>3</sub> has been an important compound due to its high Curie temperature and ability to be incorporated with other materials and systems. [6, 7]

Prior reports of single crystal growth of different solid solutions involving PbTiO<sub>3</sub> have used a variety of techniques. [8–13] Most reports of crystals use the flux method. [14–17] The floating zone technique is useful in preparing low-defect single crystals due to being crucible-free. It further has the benefit of purifying the material by zone

refinement. [18] Papers reporting using a floating zone furnace for PbTiO<sub>3</sub> had very fast growth speeds (100 mm/hr) and were largely unsuccessful due to the evaporation of PbO leading to an unstable, collapsing zone. [19] Recent progress in the use of laser diode floating zone (LDFZ) furnaces in synthesizing a wide variety of materials, including those with high vapor pressures, encourages revisit of this technique as applied to PbTiO<sub>3</sub>. [20–26]

Here we report the growth of bulk crystals (4 cm length, ~5mm OD) of PbTiO<sub>3</sub> using the LDFZ. The presence of oxygen vacancies is quantified using thermogravimetric analysis/differential thermal analysis (TGA/DTA) and shows that the floating zone-grown samples have fewer vacancies as prepared. Impurity metal concentrations are estimated from magnetization measurements and glow discharge mass spectrometry (GDMS). The presence of impurity driven room temperature ferromagnetism in flux grown crystals of PbTiO<sub>3</sub>, absent in LDFZ specimens, demonstrates the positive impacts of zone refinement and crucible-free techniques. Analysis of the low temperature heat capacity is also performed to probe the degree of structural disorder that is present. We see the expected off-centering of Pb through the fitting of the data to a series of phonon modes which serves as an explanation to previously suspect linear behavior at low temperatures. Overall, this comparison shows the usefulness of the LDFZ in growing low defect crystals of volatile materials through zone refinement as well as being crucible-free.

## Methods

### Synthesis

The flux growth for PbTiO<sub>3</sub> is adapted from the double crucible procedure of Sun et al. [14] PbO (Alfa Aesar 99.9%, Lot #B11T020) and TiO<sub>2</sub> (Alfa Aesar 99.8% metals basis, Lot #T05D048) were weighed in a 4:1 molar ratio. Materials were mixed in an

agate mortar and pestle and loaded into a Pt crucible with a Pt lid. Mortar, pestle, and Pt crucible were cleaned before use with 1 M HCl<sub>(aq)</sub>, rinsed with de-ionized water and baked at T 100° C in efforts to avoid potential contamination, especially from iron. The crucible was then placed in an alumina boat, surrounded with TiO<sub>2</sub> powder and a second alumina boat was placed upside down to serve as another lid to reduce PbO evaporation. The double crucible was placed into a tube furnace and heated to T ~ 1100° C over 10 hours, where it dwelled for 16 hours; quickly cooled to T ~ 1050° C over 1 hour; and then slow cooled to T ~ 930° C at a rate of 0.5° C/hr; at which point it cooled to room temperature over an additional 10 hours. The leftover flux was removed by sonicating in 2 M acetic acid, leaving behind rectangular crystals on average 2x1x1 mm in size.

PbTiO<sub>3</sub> powder (Alfa Aesar 99.9% metals basis, Lot #X15G039) was compacted into rod shapes using rubber balloons, evacuated, and subsequently subjected to hydro-static pressure (~75 MPa). Upon removal from the balloon, the rods were sintered in an open alumina boat in a box furnace at T ~ 1000° C for 2 hours. The sintered rods were mounted in a Laser Diode Floating Zone (LDFZ) furnace (Crystal Systems, Inc., FD-FZ-5-200-VPO-X PC) with 5 × 200 W GaAs lasers ( $\lambda = 976$  nm); the seed rod was affixed to an alumina holder on the lower shaft using Nichrome wire while the feed rod was suspended from a hook on the upper shaft using Nichrome wire. An applied pressure of 7.5 bar of Ar<sub>(g)</sub> was used flowing at 2 L/min with lasers tilted at 5° above the horizontal plane. The seed rod was melted, and the feed rod was joined to create a stable molten zone. Both rods were translated downward through the hot zone. The steady state conditions were found to occur when the upper and lower shaft traveled at a rate of 13 and 10 mm/hr while counterrotating at 10 and 20 rpm, respectively.

PbTi<sub>0.99</sub>Er<sub>0.01</sub>O<sub>3</sub> samples were doped by mixing the aforementioned PbTiO<sub>3</sub> and PbO powders with previously dried Er<sub>2</sub>O<sub>3</sub> powder in an agate mortar and pestle.

The powder was compacted into rods and sintered following the same procedure as the undoped samples. In these floating zone growths, growth conditions occurred as mentioned above except for the upper and lower shaft translating at 13.5 mm/hr and 7 mm/hr respectively. For both sets of samples, after the first initial growth, a portion of the as-grown crystal was used as the seed for subsequent growths.

## Characterization

Crystal orientation was determined using back-scattered X-ray Laue diffraction with a tungsten source operating at 10 kV and 10 mA with a Multiwire Laboratories MWL 110 real-time back reflection Laue camera. Laboratory-based X-ray diffraction patterns of the ground up single crystals were collected using a Bruker D8 Focus diffractometer with Cu  $K_{\alpha}$  radiation and a LynxEye detector. Rietveld refinements to check phase purity were performed using Bruker TOPAS software (Version 4.2, Bruker AXS). Single crystal X-ray Diffraction were collected on a Bruker-Nonius X8 Proteum (Mo  $K_{\alpha}$  radiation) diffractometer using CrysAlisPro 1.171.41.93a (Rigaku Oxford Diffraction, 2020). Structure solution/refinement were performed using the WinGX software package. [27] The structures were solved by Patterson methods using DIRDIF, followed by least-squares refinement using SHELXL-97. After initial refinements an empirical absorption correction was used, with spherical harmonics implemented in SCALE3 ABSPACK scaling algorithm, with weighting schemes applied near the end of refinement. [28] Attempts to refine occupancy of Pb or Ti sites resulted in no significant improvement in fit and as such were fixed at 1.

Heat capacity measurements from T=2-300 K were taken with a Quantum Design Physical Properties Measurement System (PPMS) using the semi adiabatic pulse method with a 1% temperature rise. Magnetization data were collected as a function of field from -7 to 7 T on unaligned crystals using a Quantum Design Magnetic Property Measurement System (MPMS). Simultaneous thermogravimetric analysis/differential

thermal analysis (TGA/DTA) was done using a TA Instruments Q600 SDT. Crystals of both flux and floating zone grown samples (10-20 mg) were loaded in alumina pans and reacted under flowing  $O_{2(g)}$  (25 mL/min). Samples were heated at a rate of 2° C/min to T = 800° C and held there for approximately 4 h. The mass change during oxidation was calculated by comparing the sample mass observed after holding at T = 150° C for 1 hr to sample mass after annealing at T = 800° to avoid errors associated with buoyancy or with surface-adsorbed moisture.

GDMS to determine trace elements was performed by Evans Analytical Group on both a floating zone grown and flux grown crystals of  $PbTiO_3$ . Sample surface and composition from the cross section of the undoped  $PbTiO_3$  crystals grown using floating zone were probed using a JEOL JSM IT100 scanning electron microscope (SEM) at 20 keV operating in backscatter mode.

## Results

### Crystal Growth

Due to the volatility of  $PbTiO_3$ , stabilization of the floating zone was achieved by:

1. applying inert gas in the system
2. using a faster travel rate than for other materials
3. utilizing laser diodes as the heating source.

It has been shown in previous crystal growths of volatile materials that using inert gas at elevated pressures has been successful in reducing the evaporation. [29, 30] Here we noticed a visible reduction of volatilization occurred when applying  $Ar_{(g)}$  at 7.5 bar of pressure. A faster travel rate is often used in floating zone growths to reduce the amount of time any part of the sample is liquid if the material decomposes upon melting. This must be empirically balanced with a slow enough rate for crystallization

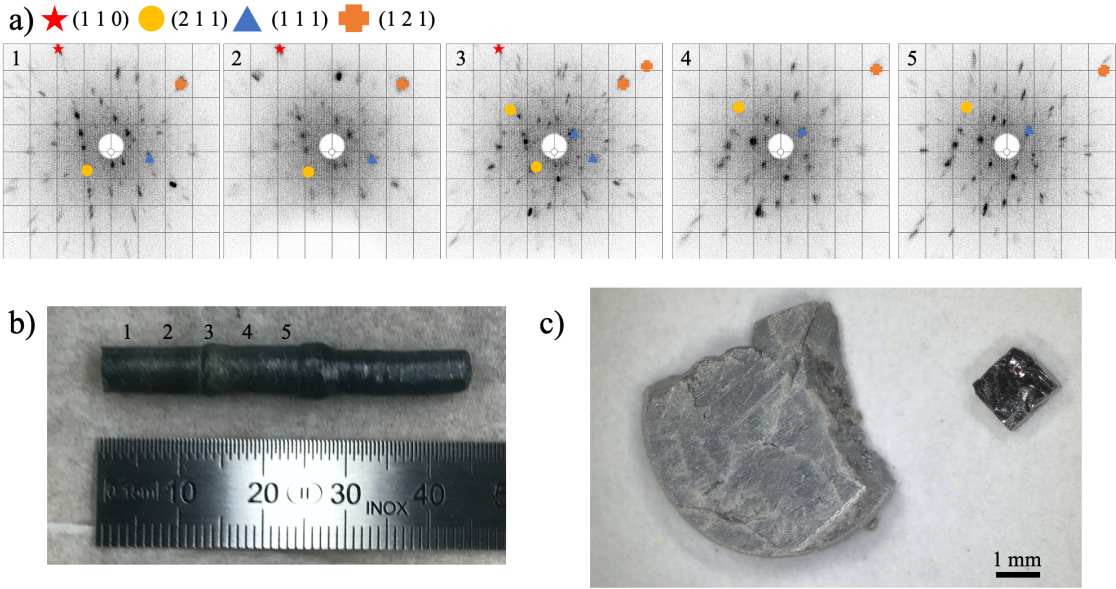


**Figure 6-1.** a) A series of Laue images taken along the length of the sanded crystal demonstrates multiple grains. Key orientations are symbolized to help one keep track of crystal reorientation, happening at pattern 3. b) The as-grown crystal of Er-doped  $\text{PbTiO}_3$  with the region labeled according to the section examined by Laue diffraction c) Piece of floating zone grown  $\text{PbTiO}_3$  (left) compared to a crystal grown using  $\text{PbO}$  flux (right).

to occur but has been demonstrated using growth speeds similar to those used here. [31] The use of laser diodes as a heating source significantly reduces the volume of the molten zone compared to conventional 4 mirror optical furnaces to approximately 1 mm in length zone with an average temperature gradient of  $150^\circ \text{ C/mm}$ .[20] This has the benefit of both an easier to maintain molten zone as well as reducing the volatility, as demonstrated in other systems utilizing laser diodes. [24–26]

Through the combination of these parameters, we were able to achieve a stable zone resulting in samples  $\sim 5$  mm diameter by 4 cm length. Laue diffraction performed on both Er-doped and stoichiometric  $\text{PbTiO}_3$  to confirm crystal quality initially shows no signal, however upon removal of an amorphous surface we see clear spots, as demonstrated for the Er-doped sample in Figure 6-1a. Indexing of the pattern along the length shows a slight reorientation occur when crystal shape changes. The doubled spots are indicative of twinning, expected for a crystal grown above the cubic to

tetragonal phase transition temperature of  $T \sim 490^\circ \text{ C}$ . An Er-doped floating zone crystal measured along its length is shown in Figure 6-1b, with a cross section of the undoped crystal shown in Figure 6-1c compared to the crystal grown via flux.

Analysis of the cross section using SEM gives us insight as to how the material loss via volatilization affects the grown crystal. [32] A combination of backscattered electron imaging and energy dispersive spectroscopy (EDS) shows that PbO loss causes the formation of  $\text{TiO}_2$  that show up preferentially as inclusions, shown in Figure 6-2. We see that while PbO loss is reduced using methods mentioned above such that stable growth is possible, defect formation is still possible. Further, these features are not random but instead have an orientation to them. Future developments in growths of this material would utilize the rotation rate to help control such formations.

The non-doped floating zone crystals are a yellowish-green color, similar to the starting powder. This is in stark contrast to dark crystals grown using flux method. The origin of color often gives us insight to the vacancies and off-stoichiometries present in a material. [33] For  $\text{PbTiO}_3$ , this color change to black has been found to occur when large amounts of excess PbO is used for the flux, with such color centers also studied computationally. [34, 35] Our experiment supports this hypothesis on the origin of the dark color, as no excess PbO was used for the floating zone growth.

Such color differences would suggest that the vacancies involved in these samples are highly impacted by the synthesis method. A flux growth technique requires the material to stay at high temperatures for long periods of time to slowly cool and crystallize. Even though the use of excess PbO as the flux reduces the melting point, there is still an issue of PbO evaporation as evidenced by the need for a double crucible. The floating zone technique uses a faster cooling rate despite its higher operating temperature. The opportunity for PbO loss should be lessened by this approach, given the other factors (applied pressure and use of laser diode heating). These two techniques are helpful comparatively in understanding the vacancies and impurities

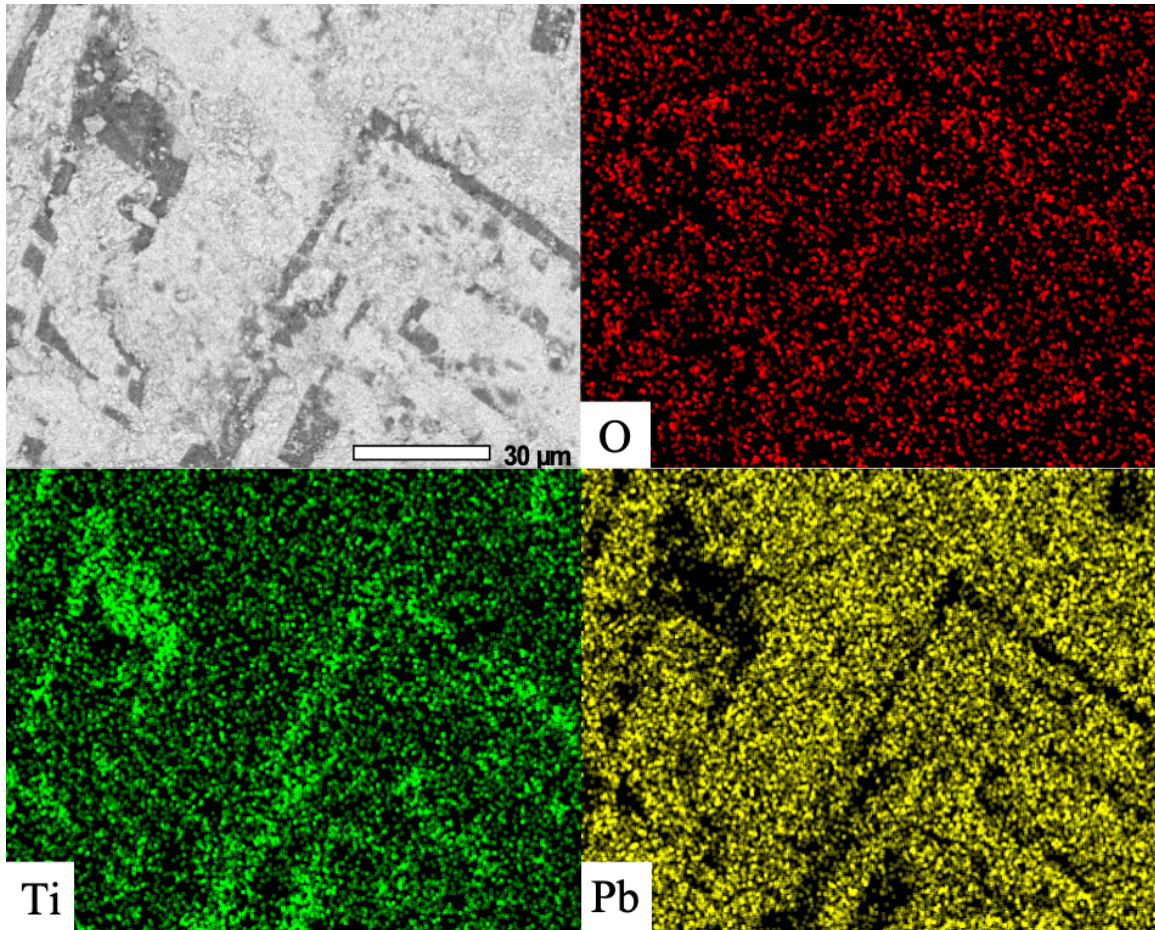


**Figure 6-2.** SEM backscattered image of the cross section of floating zone grown  $\text{PbTiO}_3$  with EDS elemental maps showing the areas of Pb deficiencies.  $\text{TiO}_2$  regions show up as inclusions with crystalline shapes.

in a material (an example being  $\text{SmB}_6$ ), and should apply for flux growths where volatization is utilized to help induce supersaturation. [36, 37]

## Structure

A comparison to the solved single crystal structure for both floating zone and flux grown samples is shown in Tables 6-I and 6-II. In both cases,  $\text{PbTiO}_3$  crystallizes in the  $P4mm$  space group below its Curie temperature, above which it transforms to the cubic  $Pm-3m$  phase. Like other ferroelectric perovskites like  $\text{BaTiO}_3$ , this cubic to tetragonal transition is an example of negative thermal expansion. Unlike  $\text{BaTiO}_3$

Formula	PbTiO <sub>3</sub>				
Synthesis Method	Floating Zone				
Crystal System	Tetragonal				
Space Group	P4mm (no. 99)				
<i>a</i> (Å)	3.8981(2)				
<i>c</i> (Å)	4.1601(3)				
<i>V</i> (Å <sup>3</sup> )	63.21(1)				
Z	1				
Radiation	Mo <i>K</i> <sub>α</sub> , $\lambda=0.71073 \text{ \AA}$				
Temperature (K)	213				
Absorption Coefficient (mm <sup>-1</sup> )	69.38				
F(0 0 0)	128				
Reflections collected/unique/internal data agreement	1662/176, <i>R</i> <sub>int</sub> =0.054				
Data/parameters	176/15				
Goodness-of-fit	1.20				
<i>R</i> = $\sum   F_o  -  F_c   / \sum  F_o $	0.020				
<i>wR</i> ( <i>F</i> <sup>2</sup> ) = $[\sum w(F_o^2 - F_c^2)^2 / \sum w(F_o^2)^2]^{1/2}$	0.047				
Largest dif. peak/hole	2.55/-1.80 e Å <sup>-3</sup>				
	Wyckoff Position	x (Å)	y (Å)	z (Å)	U <sub>iso</sub> (Å <sup>2</sup> )
Pb	1a	0	0	0	0.00879(16)
Ti	1b	0.5	0.5	0.537(2)	0.0067(14)
O1	1b	0.5	0.5	0.119(3)	0.010(2)
O2	2c	0.5	0.5	0.618(2))	0.0089(15)
	U <sub>11</sub> (Å <sup>2</sup> )	U <sub>22</sub> (Å <sup>2</sup> )	U <sub>33</sub> (Å <sup>2</sup> )	U <sub>12</sub> =U <sub>13</sub> =U <sub>23</sub> (Å <sup>2</sup> )	
Pb	0.00835(17)	0.00835(17)	0.0097(3)	0	
Ti	0.00446(6)	0.00446(6)	0.011(5)	0	
O1	0.009(3)	0.009(3)	0.011(5)	0	
O2	0.013(4)	0.003(4)	0.011(3)	0	

**Table 6-I.** Crystallographic parameters of the SXRD for floating zone grown PbTiO<sub>3</sub>

Formula	PbTiO <sub>3</sub>				
Synthesis Method	Flux				
Crystal System	Tetragonal				
Space Group	P4mm (no. 99)				
<i>a</i> (Å)	3.8969(1)				
<i>c</i> (Å)	4.1558(2)				
<i>V</i> (Å <sup>3</sup> )	63.11(1)				
Z	1				
Radiation	Mo $K_{\alpha}$ , $\lambda=0.71073$ Å				
Temperature (K)	213				
Absorption Coefficient (mm <sup>-1</sup> )	69.50				
F(0 0 0)	128				
Reflections collected/unique/internal data agreement	1911/176, $R_{int}=0.071$				
Data/parameters	176/16				
Goodness-of-fit	1.12				
$R = \sum   F_o  -  F_c   / \sum  F_o $	0.013				
$wR(F^2) = [\sum w(F_o^2 - F_c^2)^2 / \sum w(F_o^2)]^{1/2}$	0.029				
Largest dif. peak/hole	0.966/-1.244 e Å <sup>-3</sup>				
	Wyckoff Position	x (Å)	y (Å)	z (Å)	U <sub>iso</sub> (Å <sup>2</sup> )
Pb	1a	0	0	0	0.00782(15)
Ti	1b	0.5	0.5	0.5382(12)	0.0051(8)
O1	1b	0.5	0.5	0.113(2)	0.0084(16)
O2	2c	0.5	0.5	0.6178(14)	0.0060(10)
	U <sub>11</sub> (Å <sup>2</sup> )	U <sub>22</sub> (Å <sup>2</sup> )	U <sub>33</sub> (Å <sup>2</sup> )	U <sub>12</sub> =U <sub>13</sub> =U <sub>23</sub> (Å <sup>2</sup> )	
Pb	0.00846(16)	0.00846(16)	0.00654(19)	0	
Ti	0.0043(5)	0.0043(5)	0.007(3)	0	
O1	0.010(3)	0.010(3)	0.004(3)	0	
O2	0.004(3)	0.007(3)	0.007(2)	0	

**Table 6-II.** Crystallographic parameters of the SXRD for flux grown PbTiO<sub>3</sub>

## $\text{PbTiO}_3$

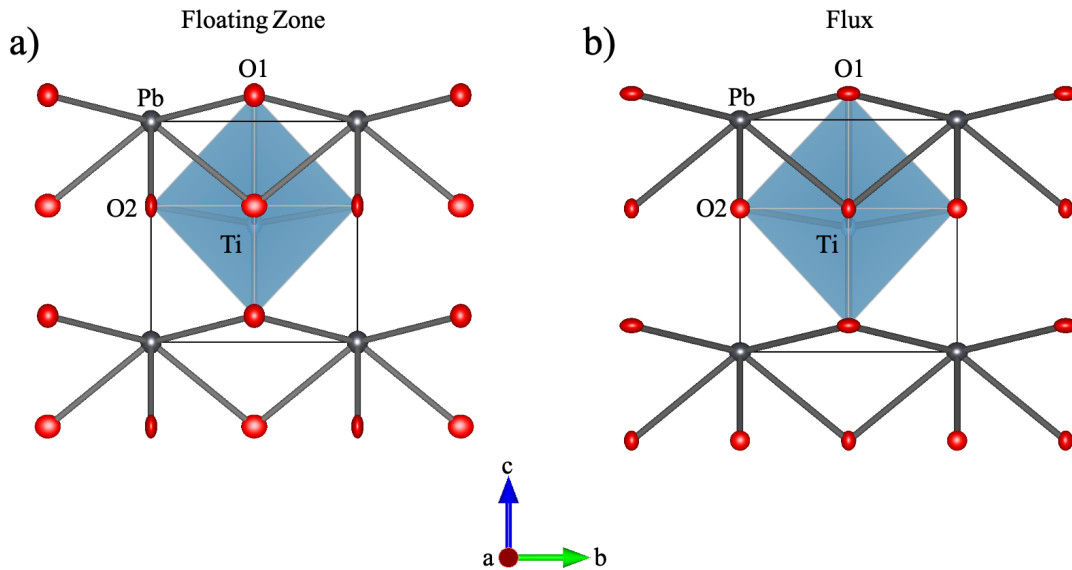


**Figure 6-3.** Visualizations of the solved crystal structure of  $\text{PbTiO}_3$  for a) floating zone grown and b) flux grown crystals. The anisotropic displacement parameters are displayed at 80% probability. [CCDC 2181876-2181877](#) contain the supplementary crystallographic data for this paper. These data can be obtained free of charge via [here](#)

however, this material exhibits no further distortion in structure upon cooling. In comparison of the unit cell volume, there is very little contraction (99.84(2)% ) in the flux method compared to the floating zone method.

Another useful comparison obtained from the diffraction data is the peak width in PXRD. This can be utilized to understand some of the strain present in the grown crystals. [38] Using equation 2.4 we can perform a Williamson Hall analysis to compare strain. While there are a variety of instrumental factors that affect such an analysis, one can still make relative comparisons between crystals. This analysis shows negative slope for both crystals, with the peak width being larger for the flux grown crystals by a factor of  $\sim 2$ .

Visualization of the anisotropic displacement parameters in Figure 6-3a for the floating zone grown sample shows “pancake”-shaped ellipsoids on the  $\text{O}_2$  site perpendicular to the  $\text{Ti}-\text{O}_2$  bond. Such values should be interpreted cautiously due

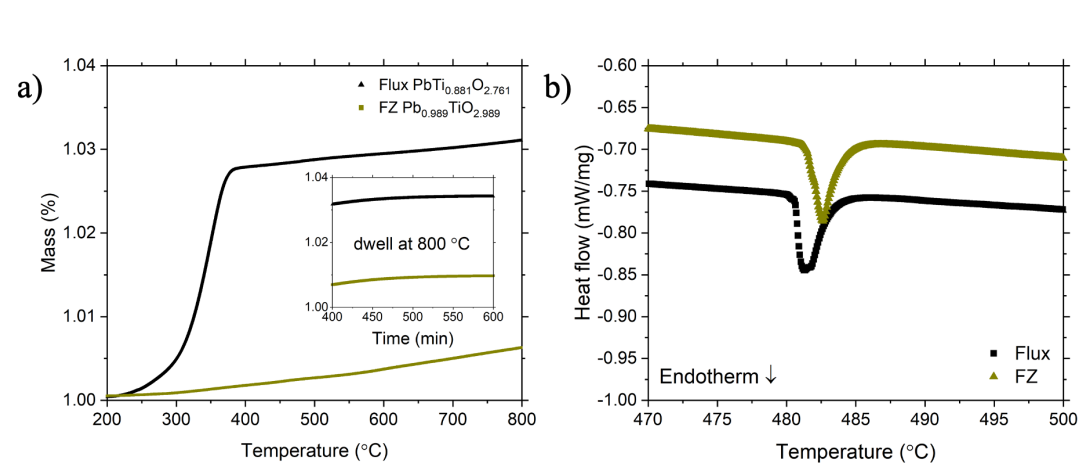


**Figure 6-4.** A comparison using TGA of the uptake in oxygen upon annealing for both samples of  $\text{PbTiO}_3$ . Samples grown using  $\text{PbO}$  flux demonstrate a greater amount of oxygen vacancies. Inset shows the saturation in mass once held at  $T=800^\circ \text{ C}$  b) The tetragonal-cubic transition for crystals grown by flux and floating zone.

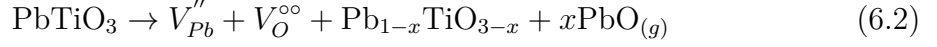
to the small mass of O compared to Ti/Pb, but such behavior has been seen in previous single crystal solutions of  $\text{PbTiO}_3$ . These shape effects can be illuminating to the dynamic and static displacements of the atoms. [39] This type of behavior has occurred before in lone pair displaced materials as well as pyrochlores in general because of tetrahedral tilting. [40, 41] The Ti ellipsoid is also elongated along the c-axis, suggesting this could be related to the displacement of the Ti atoms in the octahedral center. Interestingly, these features differ for the flux grown sample shown in Figure 6-3b, where the elongation on the O<sub>2</sub> occurs along the Ti-O<sub>2</sub> bond, with the O<sub>1</sub> atoms showing flattening perpendicular to the Ti-O<sub>1</sub> bond. Further experiments involving single crystal neutron diffraction would be helpful to better contrast O with Pb/Ti for thermal parameters and occupancy, given the color centers in the flux grown crystals.

To better quantify any oxygen deficiencies in the samples, annealing experiments under  $\text{O}_{2(g)}$  flow were performed with TGA/DTA, as shown in Figure 6-4a. Both samples gain some amount of mass after a long period of annealing, but the mass gain for the flux-grown samples is larger, as expected from the darker color. This is seen

in the initial heating and once held at  $T = 800^\circ \text{ C}$ , shown in the inset of Figure 4a. Before calculating the oxygen stoichiometry, one must consider the type of vacancy pair that is occurring. As proposed in a previous paper, the use of excess PbO would generate Ti-O deficiency, written in Kröger-Vink notation [42]:



while the floating zone method would have oxygen vacancies occurring as:



due to PbO loss (supported by the presence of  $\text{TiO}_2$  in the traveling zone at the end of the growth measured by PXRD). [34] This leads to a calculation of  $\text{PbTi}_{0.881}\text{O}_{2.761}$  and  $\text{Pb}_{0.989}\text{TiO}_{2.989}$  for flux and floating zone, respectively. Both sets of samples demonstrate an endothermic transition upon heating (seen in Figure 6-4b). This corresponds to the tetragonal-cubic transition that occurs at  $T = 482^\circ \text{ C}$  and  $T = 481^\circ \text{ C}$  for the floating zone and flux sample respectively. This slight difference in the transition could be due to an effect of the off stoichiometry of the two samples. No change in phase is observed in PXRD of samples after TGA/DTA measurements.

## Physical Properties

Heat capacity measurements are a useful way to examine the disorder and displacement in lone pair sterically active materials. [43, 44] Previous reports of the low temperature specific heat of undoped  $\text{PbTiO}_3$  indicate a Schottky anomaly at low temperatures, and a large broad peak represented as an Einstein oscillator that is generally present in ferroelectric perovskites. [44, 45] This localized optical mode results from the Pb lone pair off-centering and second order Jahn Teller distorted Ti atoms. [46] Figure 6-5 shows the data also plotted as  $C_p/T^3$  vs  $\log(T)$  to emphasize these features. In comparison to the data reported by Lawless et al., there is little to no upturn at low temperatures in our data coming from a Schottky term, proposed to exist due to

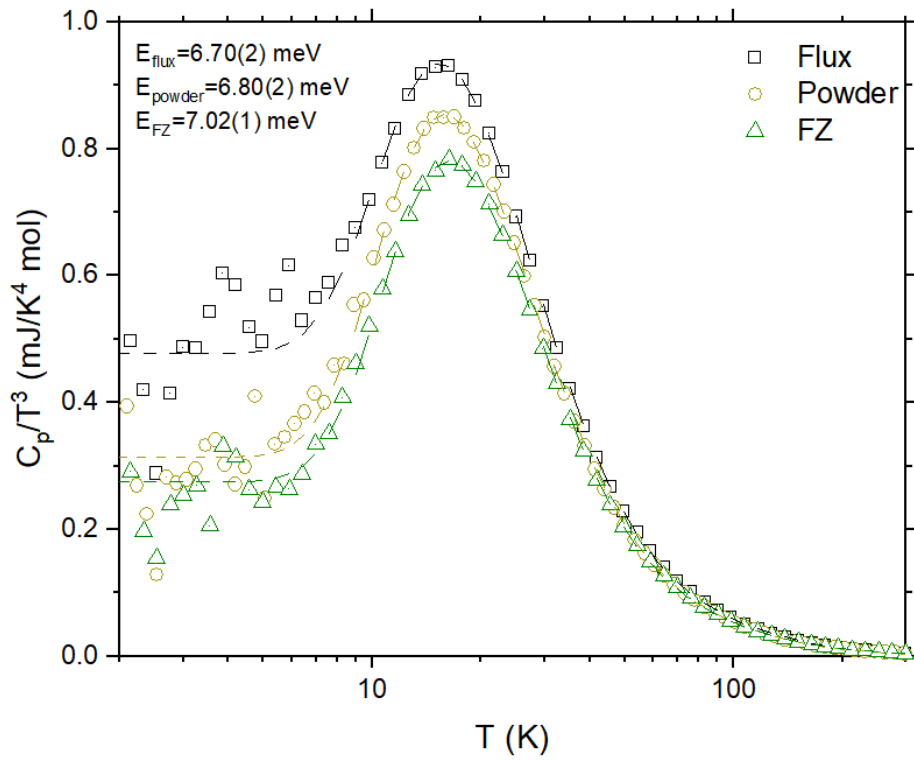


**Figure 6-5.** Heat capacity as plotted as  $C_p/T^3$  vs  $\log(T)$  to show the presence of a broad peak at low temperatures. All data sets were fit with a series of two Debye and one Einstein mode.

PbO-loss disorder. Both samples' Einstein peak are similar in width and intensity in accordance with the scale of the data.

As the presence of large broad peaks can give in-sight into the disorder present in the sample, the heat capacity data was fit to a series of Debye and Einstein modes to model the phonon behavior between samples. Purchased  $\text{PbTiO}_3$  powder used as starting material was also measured for comparison. To focus on the high temperature features, the data was fit above  $T \sim 8$  K. A minimum number of 2 Debye modes and 1 Einstein modes was needed to fit the data using equations 2.6 and 2.7. The resulting terms are represented in Table 6-III, with uncertainties derived from the standard error of the fit.

	Flux	FZ	Powder
$s_{D1}$ (oscillator strength/formula unit)	0.93(2)	0.76(1)	0.80(2)
$\theta_{D1}$ (K)	161(2)	183(2)	177(2)
$s_{D2}$	4.09(3)	3.84(3)	3.64(3)
$\theta_{D2}$ (K)	593(6)	608(5)	597(7)
$s_E$	0.420(6)	0.515(5)	0.501(6)
$\theta_E$ (K)	77.7(2)	81.4(1)	78.9(2)
Sum of oscillators	5.44(3)	5.12(3)	4.94(4)

**Table 6-III.** Fitting parameters to the  $C_p/T^3$  data for flux and floating zone crystal and starting powder

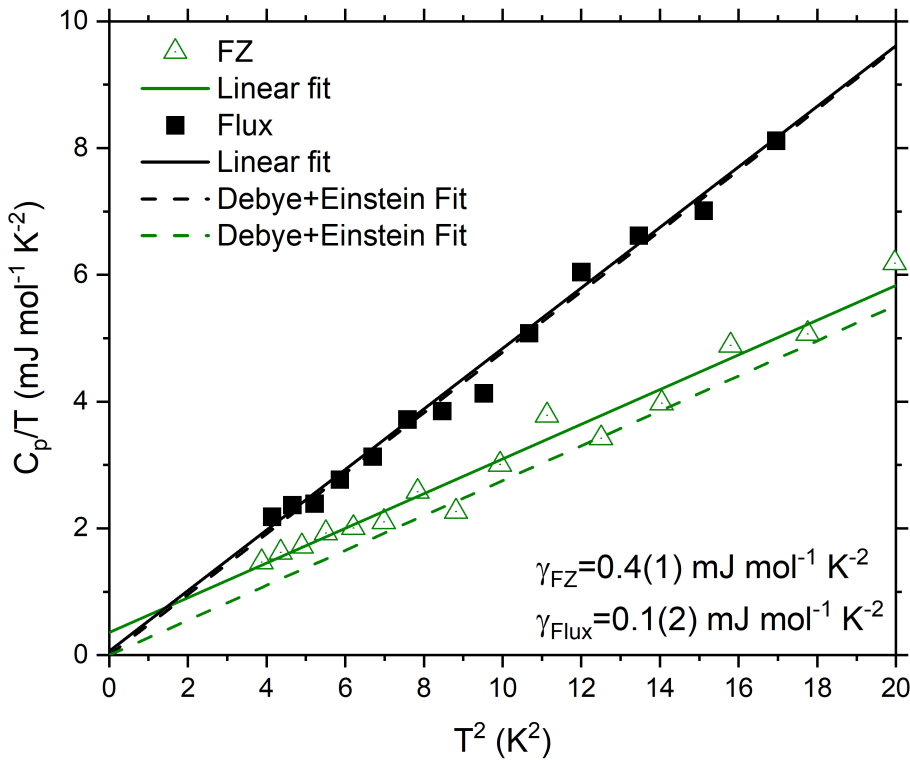
The sum of the oscillators should add up to the total number of atoms per formula unit, five in the case of PbTiO<sub>3</sub>. In our fits, the powder adheres best to this number, with the floating zone oscillator number slightly overshooting and the flux sample overshooting by a larger amount. All fits reach similar values for their Debye and Einstein temperatures. Scaling by the oscillators leads the powder and floating zone samples' Einstein peaks to have similar intensity, but the flux sample's peak grows in size.

Figure 6-6 shows the data plotted as  $C_p/T$  vs  $T^2$  to emphasize the presence of a term linear in  $T^2$  at low temperatures. At low temperatures ( $T \ll \theta_D/50$ ) the heat capacity can be approximated by the following equation:

$$C_v \approx \gamma T + \beta_3 T^3 \quad (6.3)$$

where  $\gamma$  is the electronic contribution and  $\beta_3$  corresponds to the phonon contribution. The heat capacity fit modeled from the full Debye and Einstein modes also shows approximately linear behavior when plotted this way. While one would expect an electronic contribution to show up for metals, this linear relationship holds true for many insulators as well. A variety of phenomena such as 1D spin chains, structural disorder, and lattice vacancies has been known to produce such behavior. [47–50]

The linear fits to the data give us  $\gamma$  values of 0.4(1) mJ mol<sup>-1</sup> K<sup>-2</sup> and 0.1(2) mJ



**Figure 6-6.** The low temperature region of heat capacity for both sets of crystals show a linear contribution, which can be fit to a simple linear model. The sample data can also be fit using the full Debye and Einstein terms derived from the  $C_p/T^3$  data, showing the energy of the Einstein term correlates to the “slope” of the seemingly linear data

$\text{mol}^{-1} \text{ K}^{-2}$  for the floating zone and flux samples respectively. While small, these values are not unusual in scale for such insulating oxides. [51, 52] The linear term can be correlated to the number vacancies according to:

$$\gamma_{calc} = c * n_{vac} \quad (6.4)$$

where  $c$  is the correlation value based on the distribution of the energy gap from the Schottky contribution of the vacancies present. According to this relation the number of vacancies for the flux sample should be smaller, contradicting the TGA/DTA data collected. The ordering of these vacancies can have an impact on the predictability of

this theory, which would indicate presence of defect clustering for these samples.

Thus, the more exotic phenomenon for the proposed linear term is ruled out by plotting the combined Debye and Einstein phonon contribution. One can see this fits the data almost identically to the linear fit. Given that both fits have a general phonon contribution, the addition of an Einstein oscillator best explains the linearity at low temperatures when plotted this way. The difference in energy between the two samples' Einstein terms best explains the proposed difference in slope between the samples at low temperature. This shows that when considering the presence of a linear contribution in insulators, the disorder present from off-centering can serve as a more reasonable explanation compared to rarer, exotic behavior. [53]

To investigate potential onset of magnetic behavior, magnetization as a function of applied magnetic field measurements were performed on the flux grown sample, floating zone sample, and a second floating zone sample doped with 1% Er at room temperature. Magnetic moments were seen for both Er-doped and flux grown samples, while the undoped floating zone sample showed diamagnetic behavior as seen in Figure 6-7. Of the three, the flux sample also showed presence of slight hysteresis at room temperature with a coercive field of approximately 50 Oe, shown in Figure 6-7 inset.

Given the hysteresis shown in the M vs H curve, this leads one to wonder, where is the ferromagnetic signal coming from and why is it only present in the flux grown sample? The presence of ferromagnetism in  $d^0$  oxides has been met with significant (and well deserved!) skepticism as to the origin. [54] Previous papers have predicted/reported the onset of room temperature ferromagnetism of similar magnitude in  $\text{PbTiO}_3$  due to the presence of oxygen vacancies. [55–57] If this behavior was indeed due to oxygen deficiencies, measurement of an annealed sample should show a decrease in response. Measurement of annealed flux grown crystals (supported by TGA measurements) show no decrease in magnetic signal. Due to the corrosive nature of  $\text{PbO}$  as a flux, it is possible for impurities being incorporated into the crystal.

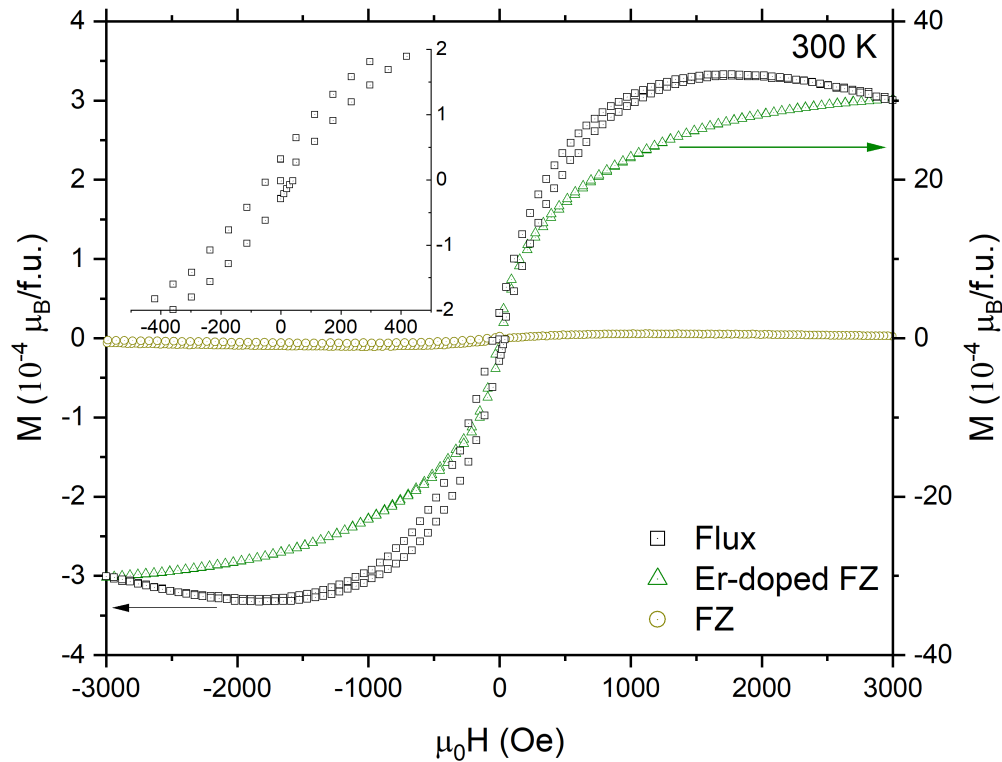


**Figure 6-7.** The presence of weak hysteresis in magnetization as a function of field for flux grown (left) crystals of  $\text{PbTiO}_3$ . The saturation in moment is quickly dispersed upon application of higher fields and is not impacted post-annealing under oxygen. This is contrasted with floating zone crystals (right showing Er-doped and inset shows the pure material).

Analysis of both crystal types using GDMS in Table 6-IV show a large impurity of Ir and Pt for the flux grown sample, likely etched off the crucible. The saturated magnetic moment can be utilized to estimate the impurity concentration.  $\text{Ir}^{4+}$  as the magnetic dopant gives us an estimated impurity of  $\sim 190$  ppm using the expected effective magnetic moment of  $1 \mu\text{B}/\text{Ir}$ . The actual observed saturated moment for such Ir-containing magnetic materials is often less however, such as the case of  $\text{Sr}_2\text{IrO}_4$ , and using such an expected saturated moment ( $0.7 \mu\text{B}/\text{Ir}$ ) gives  $\sim 2715$  ppm, closer to the determined value. [58, 59] With this evidence, we can conclude that samples grown by floating zone are not only less oxygen deficient but also have fewer impurities

(via avoiding crucible contamination and the zone refinement that naturally occurs in floating zone growths). Further research can be pursued to see the impact of Ir as an intentional dopant on the magnetic order in PbTiO<sub>3</sub>.

Element	Floating Zone Concentration (ppm wt)	Flux Concentration (ppm wt)
Li	0.05	0.13
Be	<0.01	<0.01
B	27	2.4
O	Matrix	Matrix
F	<1	<1
Na	20	40
Mg	280	24
Al	68	4.6
Si	520	10
P	140	2.4
S	25	1.8
Cl	73	8.3
K	19	2.1
Ca	130	170
Sc	<0.5	<0.5
Ti	Matrix	Matrix
V	0.48	0.08
Cr	2.2	0.26
Mn	0.52	0.09
Fe	54	19
Co	71	28
Ni	3	2.1
Cu	6.3	0.26
Zn	2.6	0.47
Ga	50	<0.05
Ge	<0.5	<0.5
As	<0.05	<0.05
Se	<0.5	<0.5
Br	<0.5	<0.5
Rb	<2	<2
Sr	320	430
Y	17	27
Zr	190	200
Nb	32	110
Mo	2.5	<0.5
Ru	<0.1	<0.1
Rh	<1	<5

Pd	<50	<50
Ag	<50	<50
Cd	<10	<10
In	Binder	Binder
Sn	120	8
Sb	4.1	1.5
Te	<5	<5
I	<5	<5
Cs	<1	<1
Ba	18	12
La	1.2	1
Ce	<0.5	<0.5
Pr	0.16	0.31
Nd	<0.5	12
Sm	<0.5	<0.5
Eu	0.23	0.17
Gd	0.85	<0.1
Tb	1.9	<0.1
Dy	<0.1	<0.1
Ho	<0.1	<0.1
Er	<0.1	<0.1
Tm	<0.1	<0.1
Yb	82	0.16
Lu	<0.1	<0.1
Hf	3.8	3.6
Ta	<10	<10
W	1.6	0.67
Re	<0.05	<0.05
Os	<0.05	<0.05
Ir	0.09	4100
Pt	<5	340
Au	<1	<1
Hg	<0.5	<0.5
Tl	<0.5	<0.5
Pb	Matrix	Matrix
Bi	52	54
Th	<0.01	<0.01
U	<0.01	<0.01

**Table 6-IV.** Trace elemental analysis performed for both a floating zone and flux grown  $\text{PbTiO}_3$  using GDMS.

## Conclusion

Overall, our work has demonstrated the feasibility of growing crystals of  $\text{PbTiO}_3$  using the floating zone method through tuning of growth parameters as well as implementation of laser diodes as the heating source. Due to the structural transition of cubic to tetragonal upon cooling, development of large single crystals will need to be improved, although other floating zone experiments dealing with such phase transitions have found a sharper gradient helps avoid such cracking. [60]

A comparison between crystals grown through floating zone and flux method demonstrate key difference in how the growth technique can impact the properties of the material. Through careful analysis of the heat capacity, we can rule out linear behavior in place of a more thorough fit of the phonon modes. The floating zone grown samples demonstrate lower defects present as evidenced by GDMS analysis, the lack of magnetism present, and the quantification of O vacancies using TGA/DTA. This reduction in defects is accomplished through the zone refinement of the inherent technique. This work shows the capabilities of the laser floating zone technique to allow for the growth of low defect  $\text{PbTiO}_3$  and can be applied more generally to volatile materials.

## Acknowledgements

This work was funded by the Platform for the Accelerated Realization, Analysis, and Discovery of Interface Materials (PARADIM), a National Science Foundation Materials Innovation Platform (NSF DMR-2039380). The MPMS was funded by the National Science Foundation, Division of Materials Research, Major Research Instrumentation Program, under Award 1828490. The authors would like to thank Dr. Maxime Siegler for helping with single crystal data collection. Raw data from the facility related to these syntheses is available at <https://data.paradim.org/doi/6x7g-3a87/>.

# References

1. Yang, X. *et al.* Recent Advances in Multiferroic Oxide Heterostructures and Devices. *Journal of Materials Chemistry C* **4**, 234–243 (2016).
2. Chengliang, L., Weijin, H., Yufeng, T. & Tom, W. Multiferroic Oxide Thin Films and Heterostructures. *Applied Physics Reviews* **2** (2015).
3. Eerenstein, W., Mathur, N. D. & Scott, J. F. Multiferroic and Magnetoelectric Materials. *Nature* **442**, 759–765 (2006).
4. Manfred, F., Lottermoser, T., Meier, D. & Trassin, M. The Evolution of Multiferroics. *Nature Reviews Materials* **1** (2016).
5. Saha, R. A. *et al.* The Critical Role of Stereochemically Active Lone Pair in Introducing High Temperature Ferroelectricity. *Inorganic Chemistry* **60**, 4068–4075 (2021).
6. Zhang, S. & Li, F. High Performance Ferroelectric Relaxor-PbTiO<sub>3</sub> Single Crystals: Status and Perspective. *Journal of Applied Physics* **111** (2012).
7. Bhatti, H. S., Hussain, S. T., Khan, F. A. & Hussain, S. Synthesis and Induced Multiferroicity of Perovskite PbTiO<sub>3</sub>; a Review. *Applied Surface Science* **367**, 291–306 (2016).
8. Grabmaier, B. C. PbTiO<sub>3</sub> Grown from the Melt. *Ferroelectrics* **13**, 501–503 (1976).
9. Gelabert, M. C., Laudise, R. A. & Rimann, R. E. Phase Stability, Solubility and Hydrothermal Crystal Growth of PbTiO<sub>3</sub>. *Journal of Crystal Growth* **197**, 195–203 (1999).
10. Harada, K., Shimanuki, S., Kobayashi, T., Saitoh, S. & Yamashita, Y. Crystal Growth and Electrical Properties of Pb((Zn<sub>1/3</sub>Nb<sub>2/3</sub>)<sub>0.91</sub>Ti<sub>0.09</sub>)O<sub>3</sub> Single Crystals Produced by Solution Bridgman Method. *Journal of the American Ceramic Society* **81**, 2785–2788 (1998).
11. Xu, J., Fan, S., Lu, B., Tong, J. & Zhang, A. Seeded Growth of Relaxor Ferroelectric Single Crystals Pb[(Zn<sub>1/3</sub>Nb<sub>2/3</sub>)<sub>0.91</sub>Ti<sub>0.09</sub>]O<sub>3</sub> by the Vertical Bridgman Method. *Japanese Journal of Applied Physics* **41** (2002).
12. Zhang, S., Rehrig, P. W., Randall, C. & Shrout, T. R. Crystal Growth and Electrical Properties of Pb(Yb<sub>1/2</sub>Nb<sub>1/2</sub>)O<sub>3</sub>-PbTiO<sub>3</sub> Perovskite Single Crystals. *Journal of Crystal Growth* **234**, 415–420 (2002).
13. Lee, H. Y. in *Handbook of Advanced Dielectric, Piezoelectric and Ferroelectric Materials* 158–172 (Woodhead Publishing, 2008).
14. Sun, B. N., Huang, Y. & Payne, D. A. Growth of Large PbTiO<sub>3</sub> Crystals by a Self-Flux Technique. *Journal of Crystal Growth* **128**, 867–870 (1993).

15. Burnett, T. L., Comyn, T. P. & Bell, A. J. Flux Growth of BiFeO<sub>3</sub>-PbTiO<sub>3</sub> Single Crystals. *Journal of Crystal Growth* **285**, 156–161 (2005).
16. Kakuta, K., Tsurumi, T. & Fukunaga, O. Dielectric Property of Flux-Grown PbTiO<sub>3</sub> Single Crystal. *Japanese Journal of Applied Physics* **34** (1995).
17. Mabud, S. A. & Glazer, A. M. Lattice Parameters and Birefringence in PbTiO<sub>3</sub> Single Crystals. *Journal of Applied Crystallography* **12**, 49–53 (1979).
18. Buehler, E. Contribution to the Floating Zone Refining of Silicon. *Review of Scientific Instruments* **28**, 453–460 (1957).
19. Maffei, N. & Rossetti Jr., G. A. Float-zone Growth and Properties of Ferroelectric Lead Titanate. *Journal of Materials Research* **19**, 827–833 (2004).
20. Ito, T. *et al.* Laser-diode-heated Floating Zone (LDFZ) Method Appropriate to Crystal Growth of Incongruently Melting Materials. *Journal of Crystal Growth* **363**, 264–269 (2013).
21. Sinha, M. *et al.* Introduction of Spin Centers in Single Crystals of Ba<sub>2</sub>CaWO<sub>6-δ</sub>. *Physical Review Materials* **3** (2019).
22. Berry, T., Pressley, L. A., Phelan, W. A., Tran, T. T. & McQueen, T. M. Laser enhanced single crystal growth of non-symmorphic materials: applications to an eight-fold fermion candidate. *Chemistry of Materials* **13**, 5827–5834 (2020).
23. Berry, T., Bernier, S., Auffermann, G., McQueen, T. M. & Phelan, W. A. Laser Floating Zone Growth of SrVO<sub>3</sub> Single Crystals. *Journal of Crystal Growth* **583**, 126518 (2022).
24. Sinha, M. *et al.* Twisting of 2D kagome sheets in layered intermetallics. *ACS Central Science* **7**, 1381–1390 (2021).
25. Scudder, M. R. *et al.* Highly Efficient Transverse Thermoelectric Devices with Re<sub>4</sub>Si<sub>7</sub> Crystals. *Energy and Environmental Science* **14**, 4009–4017 (2021).
26. Straker, M. *et al.* Growth of High Purity Zone-Refined Boron Carbide Single Crystals by Laser Diode Floating Zone Method. *Journal of Crystal Growth* **543**, 125700 (2020).
27. Farrugia, L. J. WinGX Suite for Small-Molecule Single-Crystal Crystallography. *Journal of Applied Crystallography* **32**, 837–838 (1999).
28. Clark, R. C. & Reid, J. S. The Analytical Calculation of Absorption in Multifaceted Crystals. *Acta Crystallographica A* **A51**, 887–897 (1995).
29. Phelan, W. A., Zahn, J., Kennedy, Z. & McQueen, T. M. Pushing boundaries: high pressure, supercritical optical floating zone materials discovery. *Journal of Solid State Chemistry* **270**, 705–709 (2019).
30. Dabkowska, H. A. & Dabkowski, A. B. in *Springer Handbook of Crystal Growth* 367–390 (Springer Heidelberg Dordrecht London New York, 2010).
31. Koohpayeh, S. M., Fort, D. & Abell, J. S. The Optical Floating Zone Technique: A Review of Experimental Procedures with Special Reference to Oxides. *Progress in Crystal Growth and Characterization of Materials* **54**, 121–137 (2008).
32. Koohpayeh, S. M., Wen, J. .-, Trump, B. A., Broholm, C. L. & McQueen, T. M. Synthesis, Floating Zone Crystal Growth and Characterization of the Quantum Spin Ice Pr<sub>2</sub>Zr<sub>2</sub>O<sub>7</sub> Pyrochlore. *Journal of Crystal Growth* **402** (2014).

33. Arpino, K. E., Trump, B. A., Scheie, A. O., McQueen, T. M. & Koohpayeh, S. M. Impact of Stoichiometry of  $\text{Yb}_2\text{Ti}_2\text{O}_7$  on its Physical Properties. *Physical Review B* **95** (2017).
34. K, W. The Influence of Point Defects on Selected Properties of  $\text{PbTiO}_3$  Crystals. *Ferroelectrics* **82**, 25–35 (1988).
35. Man, Z. Y. & Feng, X. Q. A computer simulation study of defects in  $\text{PbTiO}_3$  crystals. *Solid State Communications* **123**, 333–337 (2002).
36. Phelan, W. *et al.* On the chemistry and physical properties of flux and floating zone grown  $\text{SmB}_6$  single crystals. *Scientific Reports* **6** (2016).
37. Eo, Y. S. *et al.* Bulk Transport Paths Through Defects in Floating Zone and Al Flux Grown  $\text{SmB}_6$ . *Physical Review Materials* **5**, 055001 (2021).
38. Kushwaha, S. K. *et al.* Crystalline perfection, Raman, UV-VIS-NIR and prism coupler investigations on Cz-grown pure and Zn-doped  $\text{LiNbO}_3$ . *CrystEngComm* **14**, 3297–3305 (2012).
39. Yoshiasa, A. *et al.* High-Temperature Single-Crystal X-ray Diffraction Study of Tetragonal and Cubic Perovskite-Type  $\text{PbTiO}_3$  Phases. *Acta Crystallographica Section B* **72**, 381–388 (2016).
40. Shoemaker, D. P. *et al.* Atomic Displacements in the Charge Ice Pyrochlore  $\text{Bi}_2\text{Ti}_2\text{O}_6\text{O}'$  Studied by Neutron Total Scattering. *Physical Review B* **81** (2010).
41. Trump, B. A. *et al.* Universal Geometric Frustration in Pyrochlores. *Nature Communications* **9** (2018).
42. Kröger, F. A. & Vink, H. J. in *Solid State Physics* 307–345 (Academic Press, 1956).
43. Trump, B. A. & McQueen, T. M. Structure, Properties, and Disorder in the New Distorted-Hollandite  $\text{PbIr}_4\text{Se}_8$ . *Journal of Solid State Chemistry* **242**, 112–119 (2016).
44. Melot, B. C. *et al.* Large Low-Temperature Specific Heat in Pyrochlore  $\text{Bi}_2\text{Ti}_2\text{O}_7$ . *Physical Review B* **79** (2009).
45. Lawless, W. N., Nakamura, T., Takashige, M. & Swartz, S. L. Specific Heat of Amorphous and Crystalline  $\text{PbTiO}_3$  at Low Temperatures. *Journal of the Physical Society of Japan* **52**, 207–214 (1983).
46. Seshadri, R. Visualizing lone pairs in compounds containing heavier congeners of the carbon and nitrogen group elements. *Journal of Chemical Sciences* **113**, 487–496 (2001).
47. Dender, D. C., Hammar, P. R., Reich, D. H., Broholm, C. L. & Aeppli, G. Direct Observation of Field-Induced Incommensurate Fluctuations in a One-Dimensional  $S=1/2$  Antiferromagnet. *Physical Review Letters* **79**, 1750 (1997).
48. Haraguchi, Y., Matsuo, A., Kindo, K. & Hiroi, Z. Quantum Antiferromagnet Bluebellite Comprising a Maple-Leaf Lattice Made of Spin-1/2  $\text{Cu}^{2+}$  Ions. *Physical Review B* **104**, 174439 (2021).
49. Tari, A. *The Specific Heat of Matter at Low Temperatures* (Imperial College Press, 2003).

50. Schliesser, J. M. & Woodfield, B. F. Lattice Vacancies Responsible for the Linear Dependence of the Low-Temperature Heat Capacity of Insulating Materials. *Physical Review B* **91**, 024109 (2015).
51. Kumagai, K. *et al.* Linear temperature term of heat capacity in insulating and superconducting La-Ba-Cu-O Systems. *Physical Review Letters* **60**, 724–727 (1988).
52. Stephens, R. B. Low-Temperature specific heat and thermal conductivity of noncrys-talline dielectric solids. *Physical Review B* **8**, 2896–2905 (1973).
53. Chamorro, J. R., McQueen, T. M. & Tran, T. T. Chemistry of Quantum Spin Liquids. *Chemical Reviews* **121**, 2898–2934 (2021).
54. Coey, J. M. D. Magnetism in  $d^0$  Oxides. *Nature Materials* **18**, 652–656 (2019).
55. Shimada, T., Uratani, Y. & Kitamura, T. Vacancy-Driven Ferromagnetism in Ferroelectric PbTiO<sub>3</sub>. *Applied Physics Letters* **100**, 162901 (2012).
56. Xu, T., Shimada, T., Araki, Y., Wang, J. & Kitamura, T. Multiferroic Domain Walls in Ferroelectric PbTiO<sub>3</sub> with Oxygen Deficiency. *Nano Letters* **16**, 454–458 (2015).
57. Zhang, Z. *et al.* Room-Temperature Ferromagnetism and Ferroelectricity in Nanocrys-talline PbTiO<sub>3</sub>. *Solid State Sciences* **13**, 1391–1395 (2011).
58. Cao, G., Bolivar, J., McCall, S., Crow, J. E. & Guertin, R. P. Weak ferromagnetism, metal-to-nonmetal transition, and negative differential resistivity in single-crystal Sr<sub>2</sub>IrO<sub>4</sub>. *Physical Review B* **57**, R11039 (1998).
59. Kim, B. J. *et al.* Phase-sensitive observation of a spin-orbital mott state in Sr<sub>2</sub>IrO<sub>4</sub>. *Science* **323**, 1329–1332 (2009).
60. Peets, D. C., Kim, J.-h., Reehuis, M., Dosanjh, P. & Keimer, B. Floating zone growth of large single crystals of SrFeO<sub>3- $\delta$</sub> . *Journal of Crystal Growth* **361**, 201–205 (2012).

[lpressl3@jhu.edu](mailto:lpressl3@jhu.edu)

## EDUCATION AND DEGREES

2019–Current Ph.D., Department of Chemistry  
Johns Hopkins University

2017–2019 Masters, Department of Chemistry  
Johns Hopkins University

2013–2017 Bachelors with Honors, Department of Chemistry Presbyterian College

## PUBLICATIONS

[Transition Metal \(Dis\)order in Single Crystal High Entropy Perovskites](#) **Lucas A. Pressley**, Hector K. Vivanco, Maxime A. Siegler, and Tyrel M McQueen. **In Preparation**

[Informing Quantum Materials Synthesis and Design using X-ray  \$\mu\$ -Computed Tomography](#) **Lucas A. Pressley**, Dave Edey, Romy Hanna, Sieun Chae, John T. Heron Mojammal A. Khan, Tyrel M. McQueen *npj Quantum Materials* **Under Review**.

[Anomalous Residual Surface Conductivity in a Superconductor with Strong Spin-Orbit Coupling](#) Juan R. Chamorro, Prashant Chauhan, Canon Sun, Nicodemos Varnava, Michal J. Winiarski, Nicholas Ng, Hector K. Vivanco, **Lucas A. Pressley**, Chris M. Pasco, David Vanderbilt, Yi Li, N. Peter Armitage, Tyrel M. McQueen **Submitted to Physical Review Letters**.

[Germanium Dioxide: A New Rutile-Type Substrate for Epitaxial Film Growth](#) Sieun Chae, **Lucas A. Pressley**, Hanjong Paik, Jiseok Kim, Don Werder, Berit Goodge, Lena R. Kourkoutis, Robert Hovden, Tyrel M. McQueen, Emmanouil Kioupakis, and John T. Heron. *Journal Of Vacuum Science and Technology A* **Accepted**.

[Optimization of PbTiO<sub>3</sub> Single Crystals with Flux and Laser Floating Zone Method](#) **Lucas A. Pressley**, Mekhola Sinha, Hector K. Vivanco, Juan Chamorro, Sujit Das, Ramamoorthy Ramesh, and Tyrel M. McQueen *Crystal Growth and Design Accepted*.

[Toward In Situ Synchrotron Mapping of Crystal Selection Processes during Crystal Growth](#) Christopher J “CJ” Wright, Eric Dooryhée, **Lucas A. Pressley**, W Adam Phelan, Peter G Khalifah, Simon J. L. Billinge *Chemistry of Materials* **33**. 9 3359-3367 (2021).

[Twisting of 2D Kagomé Sheets in Layered Intermetallics](#) Mekhola Sinha, Hector K. Vivanco, Cheng Wan, Maxime A. Siegler, Veronica J. Stewart, Elizabeth A. Pogue, **Lucas A. Pressley**, Tanya Berry, Ziqian Wang, Isaac Johnson, Mingwei Chen, Thao T. Tran, W. Adam Phelan, and Tyrel M. McQueen *ACS Central Science* **7**. 8 1381-1390 (2021).

[Discovery and Single Crystal Growth of High Entropy Pyrochlores](#) **Lucas A. Pressley**, Angela Torrejon, W. Adam Phelan, Tyrel M. McQueen *Inorganic Chemistry* **59**. 23 17251-17258 (2020).

[Laser-Enhanced Single Crystal Growth of Non-Symmorphic Materials: Applications to an Eight-Fold Fermion Candidate](#) Tanya Berry, **Lucas A. Pressley**, W. Adam Phelan, Thao T. Tran, Tyrel M. McQueen *Chemistry of Materials* **32**. 13 5827-5834 (2020).

[Future Directions in Quantum Materials Synthesis](#) Tyrel M. McQueen, Tanya Berry, Juan R. Chamorro, Alireza Ghasemi, W. Adam Phelan, Elizabeth A. Pogue, **Lucas A. Pressley**, Mekhola Sinha, Veronica J. Stewart, Thao T. Tran, Hector K. Vivanco, Michal J. Winiarski *Fundamentals Of Quantum Materials: A Practical Guide To Synthesis And Exploration*